Die approbierte Originalversion dieser Dissertation ist an der Hauptbibliothek der Technischen Universität Wien aufgestellt (http://www.ub.tuwien.ac.at).

The approved original version of this thesis is available at the main library of the Vienna University of Technology (http://www.ub.tuwien.ac.at/englweb/).

DISSERTATION

Confinement Induced Neutron Phase

ausgeführt zum Zwecke der Erlangung des akademischen Grades eines Doktors der technischen Wissenschaften unter der Leitung von

o. Univ. Prof. Dipl. Ing. Dr. Helmut Rauch
E 141 - Atominstitut der Österreichischen Universitäten

eingereicht an der Technischen Universität Wien
Fakultät für Physik

von

Dipl. Ing. **Hartmut Lemmel**
Matrikelnummer 9226516
Neustiftgasse 22/1/11, 1070 Wien, Austria
lemmel@ati.ac.at

Wien, 11. Dezember 2006

Kurzfassung

Für Neutronen, die durch enge Kanäle fliegen, wurde von Lévy-Leblond [LL87] und Greenberger [Gre88] vorhergesagt, dass die Quantisierung des transversalen Impulses den longitudinalen Impuls derart verändert, dass es zu einem Phasenschub kommt, der mittels Neutroneninterferometrie gemessen werden kann. Dabei handelt es sich um einen rein quantenmechanischen Effekt, der auf den Welleneigenschaften von Quantenteilchen beruht.

In dieser Dissertation präsentiere ich die Vorbereitung und die Ergebnisse einer Reihe von Messungen, die an einem Stapel enger Kanäle in einem Neutroneninterferometer vorgenommen wurden. Es wurden thermische Neutronen mit den Wellenlängen 1.9Å und 2.7Å verwendet. Die Experimente wurden hauptsächlich am Institut Laue-Langevin (ILL) in Grenoble, Frankreich, durchgeführt, aber auch am National Institute of Standards and Technology (NIST) in Gaithersburg, Maryland, USA. Erste Ergebnisse sind in [RLBL02] veröffentlicht.

Darüberhinaus zeige ich detaillierte Berechnungen, die das Experiment simulieren. Der Einfluss der Kanäle auf die Neutronen wird durch Lösen der stationären Schrödingergleichung untersucht. Die Wellenfunktion wird im Kanal und hinter dem Kanal berechnet, für eine einfallende ebene Welle und für einen lokalisierten Strahl. Die Wellenfunktion liefert die vollständige Information über die durch den Einschluss erzeugte Phase, über die transmittierte Amplitude und über die Beugung an den Kanalkanten. Der Einfluss der Interferometerkristalle auf die Wellenfunktion wird mit Hilfe der dynamischen Beugungstheorie berechnet. Zum Schluss werden beide Rechnungen kombiniert, um den Neutronenstrahl als stationäres Wellenpaket zu beschreiben, das das Gesamtsystem aus Interferometer und Kanalsystem durchläuft.

Die Messungen zeigen, dass es zusätzliche Phaseneffekte geben muss, die die einschlussbedingte Phase überlagern. Die Rechnungen deuten darauf hin, dass diese zusätzlichen Beiträge zum Phasenschub aus der Beugung an den Kanälen hervorgehen könnten, in Kombination mit der dynamischen Beugung an den Kristallplatten.

Abstract

For neutrons passing through narrow channels it has been predicted by Lévy-Leblond [LL87] and Greenberger [Gre88] that the quantization of the transverse momentum of the neutron beam changes the longitudinal momentum, resulting in a phase shift that should be measurable by means of neutron interferometry. It is a purely quantum mechanical phenomenon which arises from the wave-like nature of quantum particles.

In this thesis I present the preparation and the results of a series of measurements which have been carried out with a stack of narrow channels in a neutron interferometer. Thermal neutrons with wave lengths of 1.9Å and 2.7Å have been used. The experiments have been performed mostly at the Institut Laue-Langevin (ILL) in Grenoble, France, but also at the National Institute of Standards and Technology (NIST) in Gaithersburg, Maryland, USA. First results have been published in [RLBL02].

In addition, I present detailed calculations on the experiment. The channel influence on the neutrons is studied by solving the stationary Schrödinger equation. The wave function is calculated in the channel and behind the channel, for incident plane waves and for localized beams. The wave function gives full information on the confinement induced phase, the transmitted amplitude and the diffraction on the channel edges. The effect of the interferometer crystals on the wave function is calculated using the dynamical theory of diffraction. Finally both calculations are put together in order to describe the neutron beam as a stationary wave packet passing the whole system of the interferometer and the channel stack.

The measurements show that there must be additional phase effects superimposed on the confinement phase. The calculations indicate that these additional phase contributions could arise from the diffraction by the channels in combination with the dynamical diffraction in the interferometer crystals.

Contents

1 Introduction **5**

2 Channel Calculation **9**

2.1 Wave Function for a Single Channel 10

2.1.1 Level Excitation 12

2.1.2 Phase Shift 14

2.2 Wave Function behind the Channels 18

2.3 Diffraction by the Channels 20

2.4 Localized Beam 22

2.5 Phase Shift of a Localized Beam 23

2.6 Wave Function for Multiple Cells 25

2.7 Absorber Coated Channels 29

2.7.1 Eigenvalues 30

2.7.2 Orthogonality of the Eigenfunctions 35

2.7.3 Normalization 35

2.7.4 Excitation 36

2.7.5 Orthogonalization 36

2.7.6 Excitation by an Incoming Plane Wave 38

2.7.7 Phase Shift 39

2.8 Refraction by the Channel Walls 41

2.9 Talbot Pattern 43

3 Channel Preparation **45**

3.1 Geometry 45

3.2 Selection of Materials 46

3.3 Cutting Silicon Wafers 47

3.4 Wafer Thickness 48

3.5 Photogrammetric Survey . . . 49
3.6 Sandblasting . . . 51
3.7 Bragg Reflections . . . 52

4 Measurements **55**
4.1 Setups . . . 55
4.2 Measurement Process . . . 55
4.3 Interferograms . . . 59
4.4 Data Fitting . . . 59
4.5 Channel Alignment . . . 61
4.6 Phase Shift Measurements . . . 62
4.6.1 1 and 2 cm channel length, ILL30, November 2002 . . . 63
4.6.2 1 cm channel length, ILL30, May 2003 . . . 64
4.6.3 2 cm channel length, ILL30, July 2003 . . . 66
4.6.4 NIST, February 2004 . . . 66
4.6.5 ILL45, May 2004 . . . 68
4.6.6 ILL30, March 2005 . . . 70
4.7 Conclusion . . . 72

5 Plane Wave Theory of the Interferometer **73**
5.1 Single Crystal Blade . . . 74
5.2 The Whole Interferometer . . . 76
5.3 Interferometer plus Sample . . . 78
5.4 Coherent and Incoherent Superposition . . . 78
5.5 The Phase Shifter . . . 79
5.6 Discussion of the Laue Reflection . . . 80
5.7 Fluctuations of the Blade Thickness . . . 83

6 Spherical Theory of the Interferometer **85**
6.1 Incoming Beam . . . 85
6.2 Empty Interferometer . . . 86
6.3 Interferometer with a Diffracting Sample . . . 89

Conclusion and Outlook **93**

Bibliography **94**

Chapter 1

Introduction

The Effect

Let's start with the basic idea of the confinement induced phase, as described by Lévy-Leblond [LL87] and Greenberger [Gre88]. Consider a neutron beam going through a narrow channel. Let the beam divergence be very small and let the beam direction be well aligned to the channel direction. Then the transverse momentum of the neutrons is initially zero. After entering the channel the neutrons are transversal confined between the channel walls, see figure 1.1a. The wall material represent an optical potential for neutrons which is given by $V_0 = 4\pi\hbar^2 N b_c/(2m)$ with the neutron mass m, the nucleus density N and the coherent neutron scattering length b_c of the material [BS99], [RW00]. The potential well allows only discrete energy states, causing a quantization of the transverse momentum of the neutron. In particular, the lowest possible energy value is larger than zero. At least this amount of energy is transfered from the longitudinal to the transverse momentum. This means that the longitudinal velocity

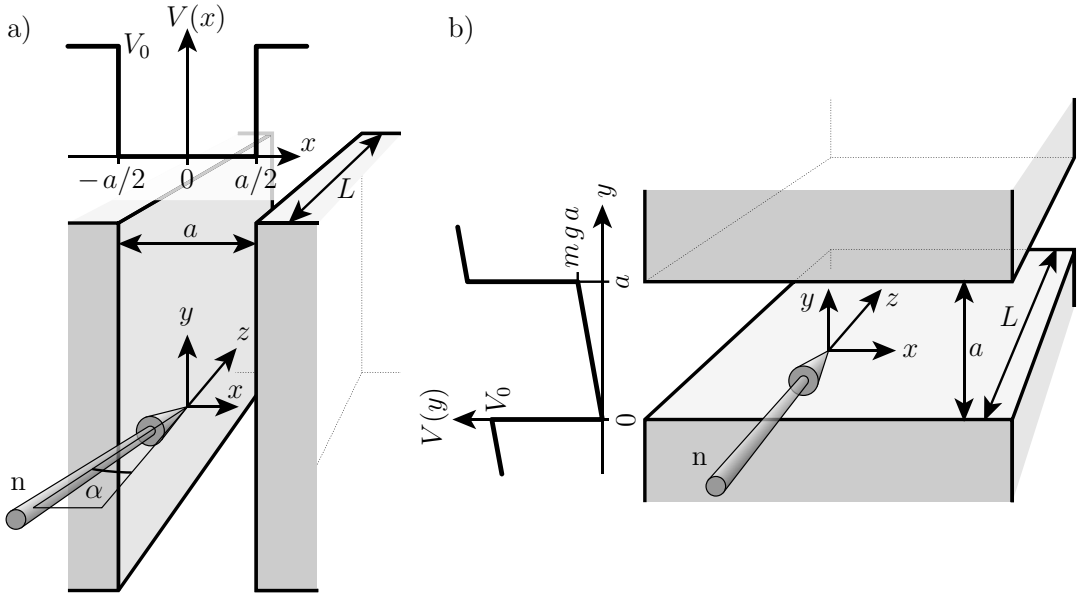

Figure 1.1: Sketch of a vertically (a) and a horizontally (b) oriented channel. In the latter case the neutron's energy in the gravitational field is added to the Fermi pseudo potential V_0 of the wall material.

is reduced inside the channel. When leaving the channel the wave function is partly diffracted, but the forward component of the neutron recovers its original momentum. As a consequence, a neutron which has gone through a channel is delayed compared to a neutron in free space, or in other words, the wave function is phase shifted. In a simple model, the phase shift is given by $L\lambda\pi/(4a^2)$ with the channel width a and the channel length L. See chapter 2 for details. The phase shift can be measured experimentally in a neutron interferometer of Mach-Zehnder type [RW00].

Related Physics

The effect is related to the slow down of electromagnetic waves in waveguides which again follows from the fact that only distinct transverse modes are allowed [Jac]. It was experimentaly verified for laser light by Allman et al. [ACGK99]. The first experiment with matter waves is presented here. While the effect can by fully understood as a phenomenon of wave mechanics, it has also been interpreted as a manifestation of a quantum potential originating in the lateral confinement [Dan02], [Kas92]. In either way it is a consequence of the non locality of a quantum particle.

If a static confinement is used, then the phase shift is not a geometrical phase, as pointed out by Peshkin [Pes00]. This is expressed by the fact that the phase shift depends on the neutron energy or wave length. The reason is that the neutron feels a force when entering and leaving the channel, because part of the wave packet touches the channel edges. At the entrance the neutron transfers part of its longitudinal momentum onto the bulk of the confinement material and receives it back at the exit. Only if a time dependent confinement was used, one could achieve a purely geometrical phase, as described by Greenberger [Gre88] and Allman [ACK00]. For such an experiment one had to ensure that the channel width is wider than the wave packet at the moment when the wave packet enters the channel region. After that, the channel walls would have to move closer together in order to create the confinement. Finally the channel would have to be widened just in time before the wave packet reaches the channel end. In this case the transverse energy modes would be changed adiabatically and the neutron wouldn't feel any longitudinal force. There would be no dispersion and no diffraction and the wave packet would leave the channel in its original shape. It would be a true analogon to the scalar Aharonov-Bohm effect [BWG$^+$93], [ALMW99]. However, the experimental realisation of a time dependent confinement would be very challenging and is not subject of the present work.

In principle the confinement induced phase arises also for particles other than neutrons but in those cases other surface or cavity effects come along. Therefore neutrons are most suitable for studying the confinement induced phase. Charged particles are influenced by the self-induced currents and mirror charges in the walls. Atoms and molecules feel — even if they are neutral — the van der Waals or Casimir forces [BFG$^+$02]. Virtual photons, which are exchanged between the atom and the surrounding vacuum all the time, are constrained in their wave length if the atom is close to a surface, because the atom and the surface form a resonator which allows only discrete values of the wave length. For distances smaller than a few nanometers the regime of the van der Waals force applies, which can also be explained by the polarizability of the atom. For larger distances the regime of the Casimir force applies [BKM04]. In any case the force is attractive. In the case of an atom beam sent through a channel it causes an acceleration of the atoms, resulting in a phase shift opposite to the confinement induced phase shift. This was experimentally measured by Perreault [PC05] in an atom interferometer. A related effect is the

life time prolongation of excited atoms in a cavity, which cannot decay as long as the photon to be emitted does not fit between the mirrors of the cavity [HR93].

There is virtually no van der Waals or Casimir force for neutrons because neutrons don't have an electron shell which could couple to electromagnetic waves. The only coupling could be achieved by a spin flip in a magnetic field. However the energy exchange $E = \mu B$ is very small, even in strong magnetic fields. It amounts to 60neV in a 1 Tesla field, which corresponds to an electromagnetic wave length of 20m.

If atoms or molecules are diffracted on slits and gratings, one has observed deviations from the classical wave optics, if the diameter of the particle is not small compared to the slit width [HK00]. However this does not play a role for neutrons whose diameter is in the order of one femtometer.

Pokotilovsky [Pok97] pointed out the additional influence of gravity in horizontally oriented channels. In this case the potential energy of the neutrons in the gravitational field has to be added to the square well, see figure 1.1b. The rising potential well creates slighly different energy levels which could in principle change the phase shift. However this change would be too small ($\ll 1°$) to be measurable by today's neutron interferometry. In addition the interpretation of an interferometric measurement would be difficult. The neutrons in the reference beam are in a state of free fall in earth's gravitational field whereas the neutrons in the channel are guided and prevented from falling. In such an experiment a phase shift could arise simpliy from the change of the potential energy or from the defocusing of the interferometer. For these reasons, our experiments have been performed only with vertically oriented channels as shown in figure 1.1a.

Nevertheless the quantization of the neutron wave function in the gravitational field becomes appaerent in the intensity transmitted by narrow channels. Nesvizhevsky et al. [NBG$^+$03], [VAB$^+$06] performed an experiment with a horizontal channel made of a reflecting floor and an absorbing ceiling. If the channel height is gradually increased starting from zero then the transmitted intensity rises in small steps as more and more transverse modes (gravitational levels) are allowed.

Semiclassical calculations on neutron capillaries and fibers have been done by various authors [AEC84], [Roh02] in order to describe the optical properties of capillary neutron guides. The point of interest in these applications is the neutron intensity. Here we need accurate information on the neutron phase and the diffraction at the channel's entrance and exit. Therefore a fully quantum mechanical approach is used.

Outline

The thesis is structured in the following way.

Chapter two contains calculations on how the neutron wave function is changed when passing through a channel. The wave function gives full information on the confinement induced phase, the transmission amplitude and the diffraction on the channel edges.

Chapter three presents the experimental preparation of the channels. The channels are made by a stack of thin silicon plates, separated by spacers. The thickness of both the plates and the spacers is in the order of 20μm. Two channel stacks have been made with a channel length of 1cm and 2cm respectively.

In chapter four the results of the phase shift measurements are presented and discussed. We will see that the results cannot be solely explained by the confinement. We will find evidence that the collimation and the diffraction caused by the channels also leads to phase effects. This is possible because a neutron interferometer is constituted by perfect crystal blades which have different properties compared to the half transparent mirrors used in an optical interferometer. The details of perfect crystal optics are described in the next chapters.

The chapters five and six present the plane wave theory of neutron interferometry and the spherical theory respectively, based on the dynamical theory of diffraction. The reflectivity of perfect crystal blades is discussed. The reflectivity depends strongly on the wave length and the beam angle. A new formalism is developed in order to calculate the influence of both the channels and the interferometer on the neutron wave function. Extensive numerical calculations would be necessary in order to apply the formalism. So far only first results of the calculations could have been obtained, which are not yet reliable in a quantitative way, but the qualitative agreement looks primisingly.

Acknoledgement

I want to thank my thesis advisor Helmut Rauch for his support and his care on the subject; Dietmar Petrascheck for the support on theoretical questions and the disposal of computer power; Johann Summhammer, Ewald Balcar, Erwin Jericha and Yuji Hasegawa for additional specialist knowledge; Matthias Baron and Rudolf Loidl for experimental help at the ILL; Muhammad Arif and Dimiry Pushin for experimental help at NIST; and all my collegues Stefan Filipp, Martin Jäkel, Jürgen Klepp, Simon Mayer, Arnold Rofner, Stephan Sponar, Martin Trinker and Michael Zawisky for having a great time during my work.

The thesis was financed by the Austrian Science Fund FWF, project SFB-F1513.

Chapter 2

Channel Calculation

The magnitude of the neutron phase shift can be roughly estimated, following Lévy-Leblond [LL87]. Consider a plane wave as incoming wave function $\psi_{in} = \exp(\mathrm{i}kz)$ with the energy $E = \hbar^2 k^2/(2m)$. m denotes the neutron mass and k is equal to 2π over the neutron wave length λ. The energy levels of an infinite potential well of width a are given as $E_n = n^2\pi^2/(2ma)$. The corresponding transverse and longitudinal wave vectors are $k_{xn} = n\pi/a$ and $k_{zn} = \sqrt{k^2 - k_{xn}^2}$. For a channel of length L the phase shift is given by $\Delta\phi_n = (k_{z,in} - k_{zn})\, L \approx L\lambda\pi n^2/(4a^2)$. Inserting numbers we get for $a = 20\mu$m, $L = 2$cm and $\lambda = 2$Å:

	$n=1$	$n=2$	$n=3$	$n=4$
E_n	0.51peV	2.05pev	4.60peV	8.18peV
$\Delta\phi_n$	0.45°	1.8°	4.05°	7.2°

It is obvious that the overall phase shift will depend on how much each level is excited. As we will see in the next sections, the excitation depends on the beam angle and the beam divergence. Nevertheless we can already see that the phase shift will be in the order of one degree. The noise limit of neutron interferometry measurements has about the same magnitude which means that the experiment is quite challenging.

As explained in the introduction, the channels should be oriented vertically. Then we don't have to care about gravitational effects and we can make all calculations in two dimensions only, because both the channels and the interferometer have no influence on the vertical wave component.

The beam cross section in neutron interferometry is in the order of 1cm. This means that a single channel of about 20μm width could use only a tiny fraction of the intensity. Therefore the experiment is done with a system of about 250 channels as illustrated in figure 2.1.

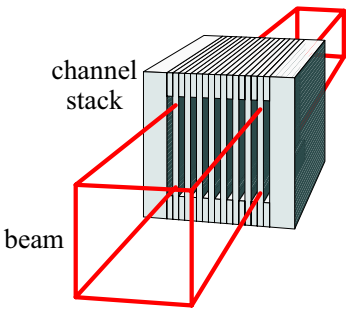

Figure 2.1: Channel stack for using the whole beam cross section.

2.1 Wave Function for a Single Channel

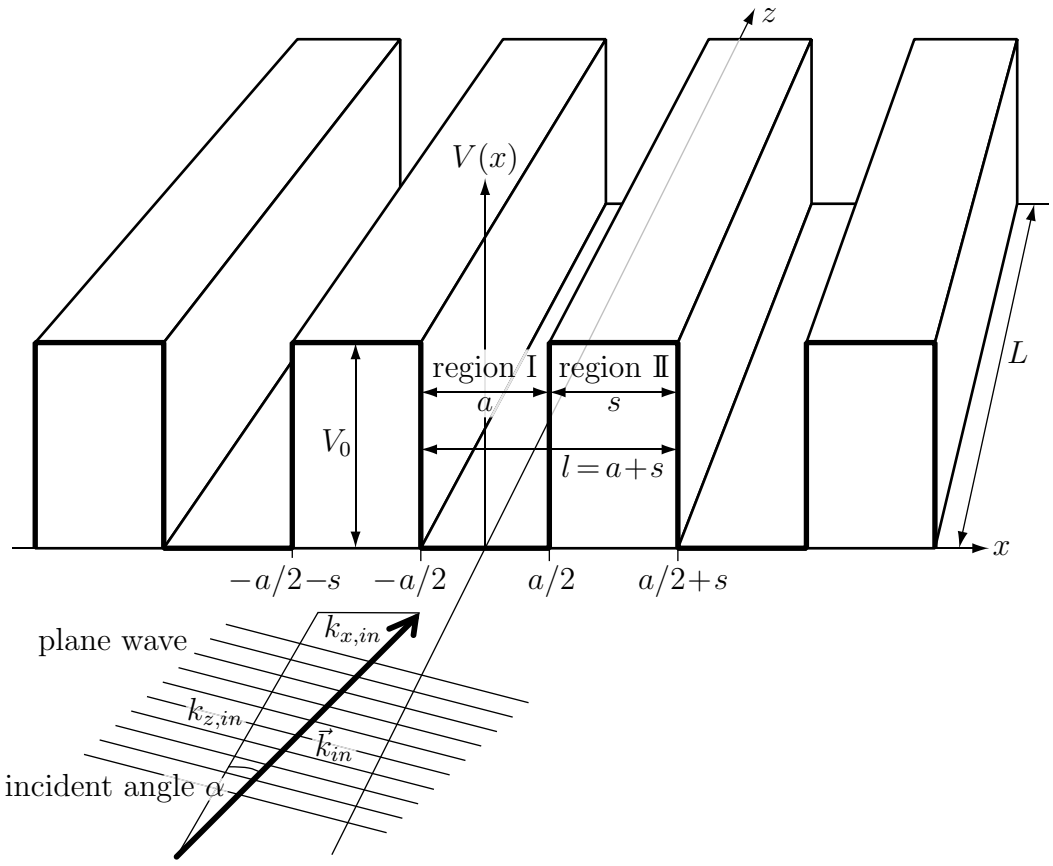

Figure 2.2: The periodic potential of the channel stack

The wave function of the neutrons inside the channel stack ($0 < z < L$) is calculated by solving the Schrödinger equation with the periodic potential $V(x)$ given by figure 2.2.

$$\left(-\frac{\hbar^2\nabla^2}{2m} + V(x)\right)\psi(x,z,t) = \mathrm{i}\hbar\frac{\partial}{\partial t}\psi(x,z,t) \tag{2.1}$$

The potential is time independent and within the channel stack also independent from z. So we can make the separation ansatz $\psi(x,z,t) = \psi_x(x)\psi_z(z)\psi_t(t)$. We get for the z component:

$$\left(-\frac{\hbar^2}{2m}\frac{d^2}{dz^2} - E_z\right)\psi_z(z) = 0 \qquad \Rightarrow \qquad \psi_z = \mathrm{e}^{\mathrm{i}k_z z}\ ,\ k_z^2 = \frac{2mE_z}{\hbar^2} \tag{2.2}$$

For the x component we have to solve the equation

$$\left(-\frac{\hbar^2}{2m}\frac{d^2}{dx^2} + V(x) - E_x\right)\psi_x(x) = 0 \tag{2.3}$$

We get for the time component:

$$\psi_t = \mathrm{e}^{-\mathrm{i}(E_x+E_z)t/\hbar} \tag{2.4}$$

E_x is given by the solutions of the eigenvalue equation (2.3). The total energy is given by the incoming neutron and must be conserved. Therefore each E_x has a corresponding $E_z = E_{in} - E_x$. For all further calculations we will write E instead of E_x.

Here we will assume a single channel with periodic boundary conditions. The multi channel solution will be investigated in section 2.6. We make the ansatz:

$$-\tfrac{a}{2} < x < \tfrac{a}{2}: \qquad \psi_{\rm I}(x) = A\sin(kx) + B\cos(kx) \qquad k^2 = \tfrac{2\,m\,E}{\hbar^2} \tag{2.5}$$

$$\tfrac{a}{2} < x < \tfrac{a}{2}+s: \qquad \psi_{\rm II}(x) = C\sin\big(K(x-\tfrac{l}{2})\big) + D\cos\big(K(x-\tfrac{l}{2})\big) \qquad K^2 = \tfrac{2\,m\,(E-V_0)}{\hbar^2} \tag{2.6}$$

The matching conditions and the periodic boundary conditions are:

$$\psi_{\rm I}(\tfrac{a}{2}) = \psi_{\rm II}(\tfrac{a}{2}) \qquad \psi_{\rm I}(-\tfrac{a}{2}) = \psi_{\rm II}(s+\tfrac{a}{2}) \tag{2.7}$$

$$\psi'_{\rm I}(\tfrac{a}{2}) = \psi'_{\rm II}(\tfrac{a}{2}) \qquad \psi'_{\rm I}(-\tfrac{a}{2}) = \psi'_{\rm II}(s+\tfrac{a}{2}) \tag{2.8}$$

The norm condition is:

$$1 = \frac{1}{l}\int_{-a/2}^{a/2}\psi_{\rm I}(x)\;\psi^*_{\rm I}(x)\;dx + \frac{1}{l}\int_{a/2}^{l-a/2}\psi_{\rm II}(x)\;\psi^*_{\rm II}(x)\;dx \tag{2.9}$$

Because of the potential symmetry and the choice of the origin we get two independent sets of solutions:

• symmetric states

$$\psi^{\rm sym}_{\rm I}(x) = \frac{\cos kx}{N^{\rm sym}\cos\frac{ka}{2}} \qquad \text{eigenvalue equation:} \quad k\tan\tfrac{ka}{2} = -K\tan\tfrac{Ks}{2} \tag{2.10}$$

$$\psi^{\rm sym}_{\rm II}(x) = \frac{\cos\big(K(x-\frac{l}{2})\big)}{N^{\rm sym}\cos\frac{Ks}{2}} \qquad \text{norm:} \quad N^{\rm sym} = \sqrt{\frac{\frac{ka}{2}+\sin\frac{ka}{2}\cos\frac{ka}{2}}{kl\cos^2\frac{ka}{2}} + \frac{\frac{Ks}{2}+\sin\frac{Ks}{2}\cos\frac{Ks}{2}}{Kl\cos^2\frac{Ks}{2}}} \tag{2.11}$$

• antisymmetric states

$$\psi^{\rm asy}_{\rm I}(x) = \frac{\sin kx}{N^{\rm asy}\sin\frac{ka}{2}} \qquad \text{eigenvalue equation:} \quad k\cot\tfrac{ka}{2} = -K\cot\tfrac{Ks}{2} \tag{2.12}$$

$$\psi^{\rm asy}_{\rm II}(x) = \frac{-\sin\big(K(x-\frac{l}{2})\big)}{N^{\rm asy}\sin\frac{Ks}{2}} \qquad \text{norm:} \quad N^{\rm asy} = \sqrt{\frac{\frac{ka}{2}-\sin\frac{ka}{2}\cos\frac{ka}{2}}{kl\sin^2\frac{ka}{2}} + \frac{\frac{Ks}{2}-\sin\frac{Ks}{2}\cos\frac{Ks}{2}}{Kl\sin^2\frac{Ks}{2}}} \tag{2.13}$$

For $E < V$ (bound states) K becomes imaginary and it is convenient to replace K by $\mathrm{i}\kappa$:

• symmetric states (bound)

$$\psi^{\rm symb}_{\rm I}(x) = \frac{\cos kx}{N^{\rm symb}\cos\frac{ka}{2}} \qquad \text{eigenvalue equation:} \quad k\tan\tfrac{ka}{2} = \kappa\tanh\tfrac{\kappa s}{2} \tag{2.14}$$

$$\psi^{\rm symb}_{\rm II}(x) = \frac{\cosh\big(\kappa(x-\frac{l}{2})\big)}{N^{\rm symb}\cosh\frac{\kappa s}{2}} \qquad \text{norm:} \quad N^{\rm symb} = \sqrt{\frac{\frac{ka}{2}+\sin\frac{ka}{2}\cos\frac{ka}{2}}{kl\cos^2\frac{ka}{2}} + \frac{\frac{\kappa s}{2}+\sinh\frac{\kappa s}{2}\cosh\frac{\kappa s}{2}}{\kappa l\cosh^2\frac{\kappa s}{2}}} \tag{2.15}$$

• antisymmetric states (bound)

$$\psi_{\mathrm{I}}^{\mathrm{asyb}}(x) = \frac{\sin kx}{N^{\mathrm{asyb}} \sin \frac{ka}{2}} \qquad \text{eigenvalue equation:} \quad k \cot \tfrac{ka}{2} = -\kappa \coth \tfrac{\kappa s}{2} \tag{2.16}$$

$$\psi_{\mathrm{II}}^{\mathrm{asyb}}(x) = \frac{-\sinh\big(\kappa(x - \frac{l}{2})\big)}{N^{\mathrm{asyb}} \sinh \frac{\kappa s}{2}} \qquad \text{norm:} \quad N^{\mathrm{asyb}} = \sqrt{\frac{\frac{ka}{2} - \sin\frac{ka}{2}\cos\frac{ka}{2}}{kl \sin^2 \frac{ka}{2}} - \frac{\frac{\kappa s}{2} - \sinh\frac{\kappa s}{2}\cosh\frac{\kappa s}{2}}{\kappa l \sinh^2 \frac{\kappa s}{2}}} \tag{2.17}$$

The eigenvalue equations can be solved numerically and give a discrete series of eigenvalues E_n. For the bound states ($E < V_0$) we have an alternating series of symmetric and antisymmetric eigenstates. For the free states this is not the case but nevertheless we can sort all energy levels by its value and assign an index number n. The general solution is a superposition of all levels.

$$\psi_{x,n}(x) = (2.10)...(2.17) \qquad \text{with } E_{x,n} \equiv E_n \text{ found numerically} \tag{2.18}$$

$$\psi_{z,n}(z) = \mathrm{e}^{\mathrm{i}k_{z,n}z} \qquad \text{with } E_{z,n} = E_{in} - E_n, \quad k_{z,n}^2 = \tfrac{2mE_{z,n}}{\hbar^2} = k_{in}^2 - k_{x,n}^2 \tag{2.19}$$

$$\psi_n(x,z) = \psi_{x,n}(x)\, \psi_{z,n}(z) =: |\psi_n\rangle \tag{2.20}$$

$$\psi_{ch}(x,z) = \sum_n u_n \psi_n(x,z) = \sum_n u_n\, \psi_{x,n}(x)\, \mathrm{e}^{\mathrm{i}k_{z,n}z} \tag{2.21}$$

Figure 2.3 shows the wave functions of the first levels. For the typical channel dimensions and wall potential we get a few hundred bound levels followed by an infinite number of free levels. As we will see in the next section, only a distinct range of levels will be excited. Therefore we can terminate the sum e.g. at level 1000.

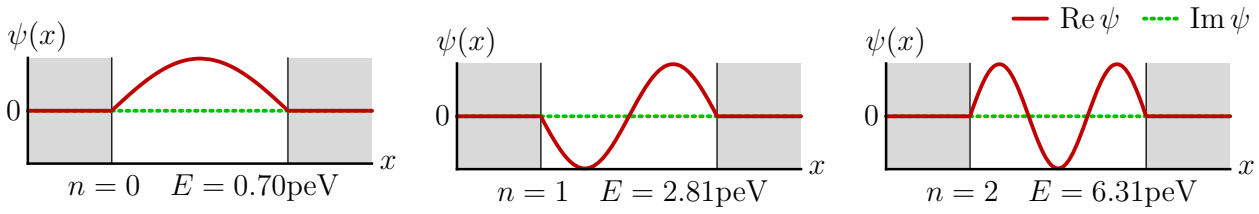

Figure 2.3: The wave functions of the first three energy levels. The energy values are calculated for $a = 17\mu$m, $s = 22\mu$m and $V_0 = 53.9751$neV (see table 5.1, pg. 76).

2.1.1 Level Excitation

At the beginning of the channel ($z = 0$) the wave function (2.21) should be equal to an arbitrary incoming wave function $|\psi_{in}\rangle$. Reflections at the channel entrance can be neglected because $E_{in} \gg V_0$. The energy E_{in} of thermal neutrons is in the range of 10 to 25 meV while the silicon potential V_0 amounts to 54 neV. Expanding $|\psi_{in}\rangle$ by the channel eigenfunctions $|\psi_n\rangle$ leads to the excitation amplitudes u_n.

$$u_n = \langle \psi_n | \psi_{in} \rangle_{z=0} = \frac{1}{l} \int_{-l/2}^{l/2} \psi_{x,n}^*(x)\, \psi_{in}(x, z{=}0)\, dx \tag{2.22}$$

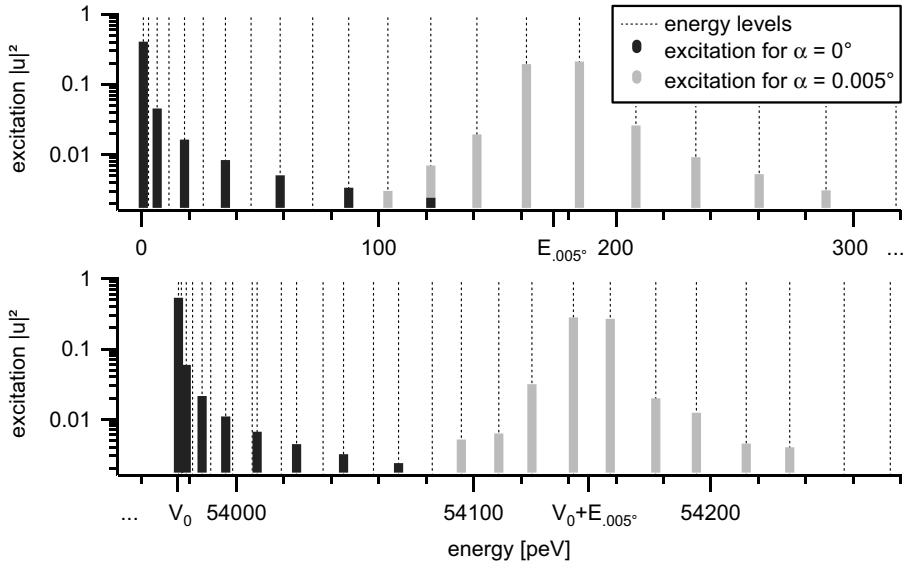

Figure 2.4: Excitation of the energy levels, calculated for two incident angles α. The plot is divided into two blow-ups of the energy scale. The upper one shows the bound levels in the range $E \geq 0$. The lower one shows the free levels at $E \geq V_0$. The strongest excitation is found for the levels which are closest to the incoming transverse energy which is 0 for $\alpha = 0$ and 173 peV for $\alpha = 0.005°$, denoted with $E_{.005}$. For $\alpha = 0$ only symmetric levels are excited, that is every second level in the plot, because the wave function must be symmetric in x.

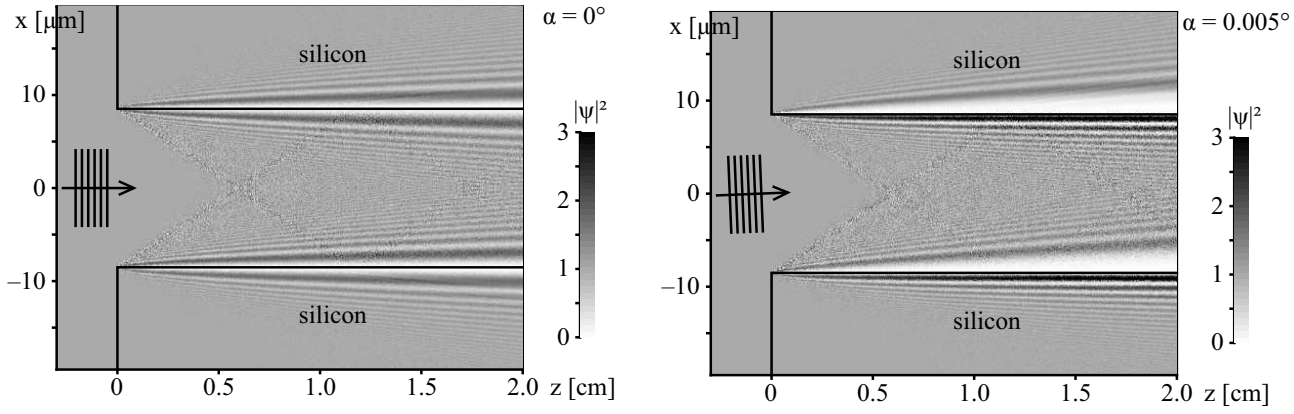

Figure 2.5: The intensity distributions inside the channel for an incoming plane wave with incident angle $\alpha = 0$ and $\alpha = 0.005°$. Near the channel walls the intensity shows oscillations which are well known from the Fresnel diffraction pattern of a slit. For $\alpha \neq 0$ we can see shadow regions with no intensity (white) and reflection regions with the interference fringes of the incoming and reflected components. The diagonal lines starting from the silicon edges at the begin of the channel represent the border lines where the initial plane wave is disturbed. The angle of these lines depends on the height of the potential which is equal to the maximum amount of energy which can be transferred from the longitudinal to the transverse direction. (The classical analogon would be a ball which is rolling up the front of a hill and rolling down its side.) The noisy features arise from oscillations which cannot be resolved by the plot resolution. In order to avoid Moiré effects the wave function is evalutated at a random position within each pixel.

Using plane waves as incoming wave function $|\psi_{in}\rangle = \exp(\mathrm{i}\vec{k}_{in}\vec{r})$ with incident angle α as shown in figure 2.2, we get the u_n as a function of the incident angle.

$$u_n(\alpha) = \frac{1}{l}\int_{-l/2}^{l/2} \psi^*_{x,n}(x)\, \mathrm{e}^{\mathrm{i}k_{in}x\sin\alpha} \tag{2.23}$$

The results are listed below, calculated for the symmetric and the antisymmetric solutions, with the short term $h := k_{x,in} = k_{in}\sin\alpha$. All k, K and κ depend on E_n.

$$u_n^{\mathrm{sym}} = \frac{1}{l\sqrt{N^{\mathrm{sym}}}}\left[\frac{1}{\cos\frac{ka}{2}}\left(\frac{\sin\frac{ka-ha}{2}}{k-h}+\frac{\sin\frac{ka+ha}{2}}{k+h}\right)+\frac{\exp(\mathrm{i}\frac{hl}{2})}{\cos\frac{Ks}{2}}\left(\frac{\sin\frac{Ks-hs}{2}}{K-h}+\frac{\sin\frac{Ks+hs}{2}}{K+h}\right)\right] \tag{2.24}$$

$$u_n^{\mathrm{asy}} = \frac{\mathrm{i}}{l\sqrt{N^{\mathrm{asy}}}}\left[\frac{1}{\sin\frac{ka}{2}}\left(\frac{\sin\frac{ka-ha}{2}}{k-h}-\frac{\sin\frac{ka+ha}{2}}{k+h}\right)-\frac{\exp(\mathrm{i}\frac{hl}{2})}{\sin\frac{Ks}{2}}\left(\frac{\sin\frac{Ks-hs}{2}}{K-h}-\frac{\sin\frac{Ks+hs}{2}}{K+h}\right)\right] \tag{2.25}$$

For the bound states we can again replace K by $\mathrm{i}\kappa$:

$$u_n^{\mathrm{symb}} = \frac{1}{l\sqrt{N^{\mathrm{symb}}}}\left[\frac{1}{\cos\frac{ka}{2}}\left(\frac{\sin\frac{ka-ha}{2}}{k-h}+\frac{\sin\frac{ka+ha}{2}}{k+h}\right)+\frac{\exp(\mathrm{i}\frac{hl}{2})}{\cosh\frac{\kappa s}{2}}\,\frac{\kappa\sinh\frac{\kappa s}{2}\cos\frac{hs}{2}+h\cosh\frac{\kappa s}{2}\sin\frac{hs}{2}}{\frac{1}{2}(\kappa^2+h^2)}\right] \tag{2.26}$$

$$u_n^{\mathrm{asyb}} = \frac{\mathrm{i}}{l\sqrt{N^{\mathrm{asyb}}}}\left[\frac{1}{\sin\frac{ka}{2}}\left(\frac{\sin\frac{ka-ha}{2}}{k-h}-\frac{\sin\frac{ka+ha}{2}}{k+h}\right)-\frac{\exp(\mathrm{i}\frac{hl}{2})}{\sinh\frac{\kappa s}{2}}\,\frac{\kappa\cosh\frac{\kappa s}{2}\sin\frac{hs}{2}-h\sinh\frac{\kappa s}{2}\cos\frac{hs}{2}}{\frac{1}{2}(\kappa^2+h^2)}\right] \tag{2.27}$$

It turns out that basically only the energy levels which are closest to the incoming transverse energy are excited. There are always two groups of excited levels, one within the bound levels and one within the free levels, because the beam enters both the channels and the walls. See figure 2.4. With the excitation amplitudes we can calculate the whole wave function inside the channel. See figure 2.5. The pictures have been calculated with a C++ program.

2.1.2 Phase Shift

The phase shift is calculated by comparing the phase of the wave function behind the channels with the phase of the incident wave function at the same position. As a first approach only the transmitted component parallel to the incident beam is taken into account. The diffracted part will be discussed in section 2.3. The non deviated component is calculated by the backprojection of the channel wave function onto the incident plane wave at the channel end $z = L$:

$$\psi_{out} = \langle\psi_{in}|\psi_{ch}\rangle_{z=L}\ \psi_{in} =: S\cdot\psi_{in} \tag{2.28}$$

Using again plane waves for $|\psi_{in}\rangle$ we get with (2.21):

$$S := \langle\psi_{in}|\psi_{ch}\rangle_{z=L} = \sum_n |u_n|^2\exp(\mathrm{i}L\,\Delta k_n),\quad \Delta k_n = k_{z,n}-k_{z,in} \tag{2.29}$$

S is a complex factor which describes the effect of the channel on the wave function. The argument value of S represents the phase shift and the absolute value represents the transmitted amplitude. The amplitude affects the interference contrast or visiblilty as given in (5.36).

The sum in (2.29) can be interpreted as an averaging over the phase shifts of all levels. Each level is weighted by the excitation probability $|u_n|^2$ and contributes with the phase shift $\Delta\phi_n = L\,\Delta k_n$ which is caused by the difference of the k_z components of the incoming wave and the channel wave function. $\Delta\phi_n$ is proportional to L and approximately inverse proportional

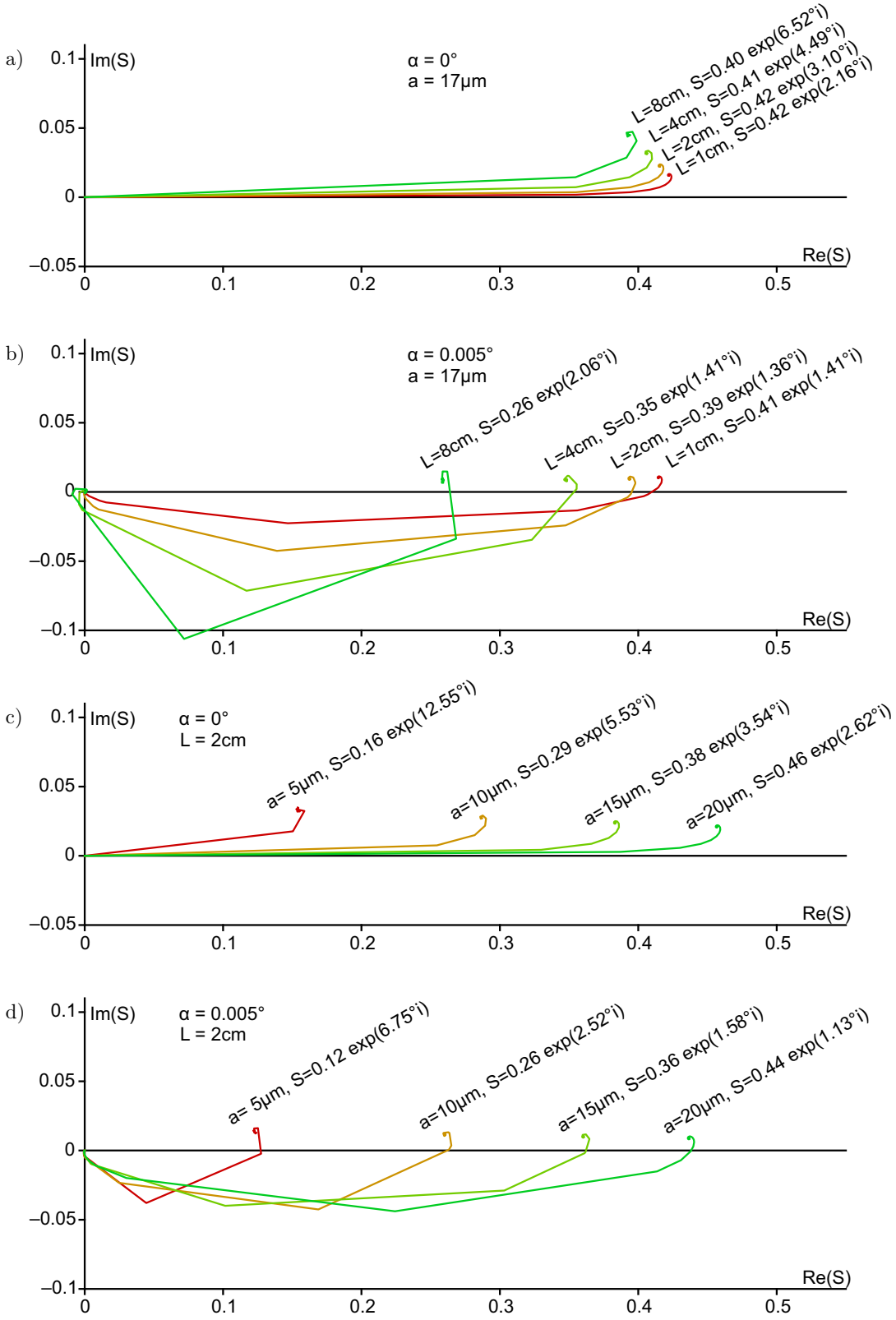

Figure 2.6: Graphical illustration of the sum in formula (2.29). The summands are represented by straigt lines in the complex plane and are concatenated, starting at the origin and ending at the value of S. The figures a) and b) show S for different values of L at constant a. c) and d) show S for different values of a at constant L. The incident angle α is zero in figure a) and c) and 0.005° in figure b) and d).

to a^2. The latter relation holds exactly for an infinitely high wall potential and is a good approximation for the lower levels in an finite potential well.

$$\Delta\phi_n = \Delta\phi_{n0}\frac{L}{L_0}\frac{a_0^2}{a^2} \tag{2.30}$$

However, this proportionality does only hold for a single level and *not* for the sum as a whole.

$$\arg(S) \neq \arg(S_0)\frac{L}{L_0}\frac{a_0^2}{a^2} \tag{2.31}$$

The reason is shown in figure 2.6 where the sum is composed graphically by its summands. Figure 2.6 a) shows four different sums, calculated for incident angle $\alpha = 0$ but for different values of L. When L is doubled then the argument value (the angle versus the real axis) of each summand also doubles, but the argument value of the total sum does not.

The quantities S, u_n and $k_{z,in}$ depend on the incident angle α. In figure 2.7 the absolute and argument values of S are plotted as a function of α for a channel stack with perfect geometry. The curves show strong oscillations as well as an asymmetry in respect to α. These oscillations and even the non oscillating central part of the phase change rapidly if the channel length is varied. These effects are caused by the beam part going through the silicon walls. The so called lambda thickness, which is the thickness of a phase shifter causing a phase shift of 2π, is 120 μm for thermal neutrons in silicon. This means that the phase of (2.29) makes a 2π oscillation if L is changed by 120 μm. The asymmetry in figure 2.7 follows from the correlation between α and λ due to Bragg's law.

To get rid of the wall part the edges of the walls have been roughend in the order of magnitude of the lambda thickness. Averaging (2.29) over a Gaussian distribution of the channel length $g(L) = \frac{1}{\sqrt{2\pi\sigma^2}}\exp(-(L-L_0)^2/(2\sigma_L^2))$ results in

$$S := \int dL\, g(L)\, \langle\psi_{in}|\psi_{ch}\rangle_{z=L} = \sum_n |u_n|^2 \exp(\mathrm{i}L\,\Delta k_n)\exp(-\tfrac{1}{2}(\Delta k_n \sigma_L)^2). \tag{2.32}$$

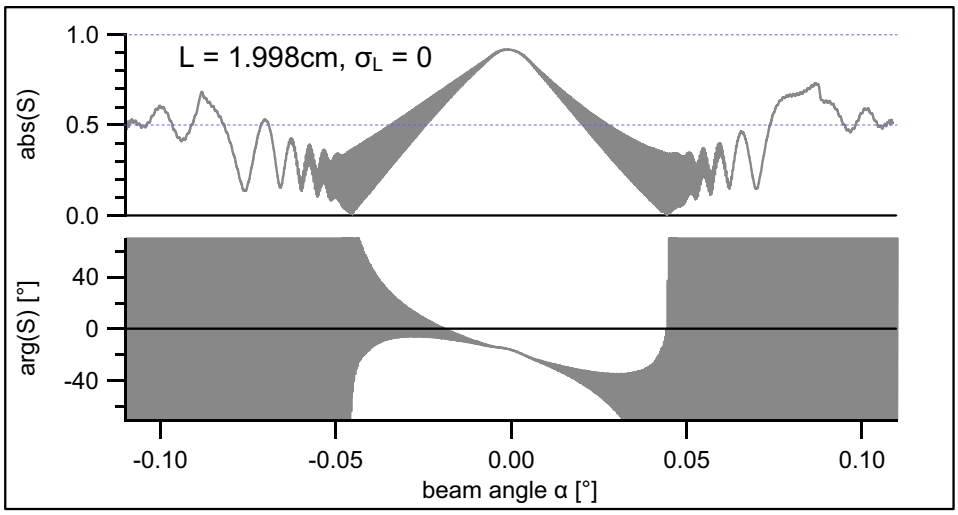

Figure 2.7: Transmission amplitude abs(S) and phase shift arg(S) of a plane wave as a function of the incident angle α. The rapid oscillations (black areas) of the phase are explained in figure 2.8. The phase value for $\alpha = 0$ is quite random because it is dominated by the neutrons travelling through the silicon. It makes a 360° oscillation if the length L of the silicon is changed by 120μm.

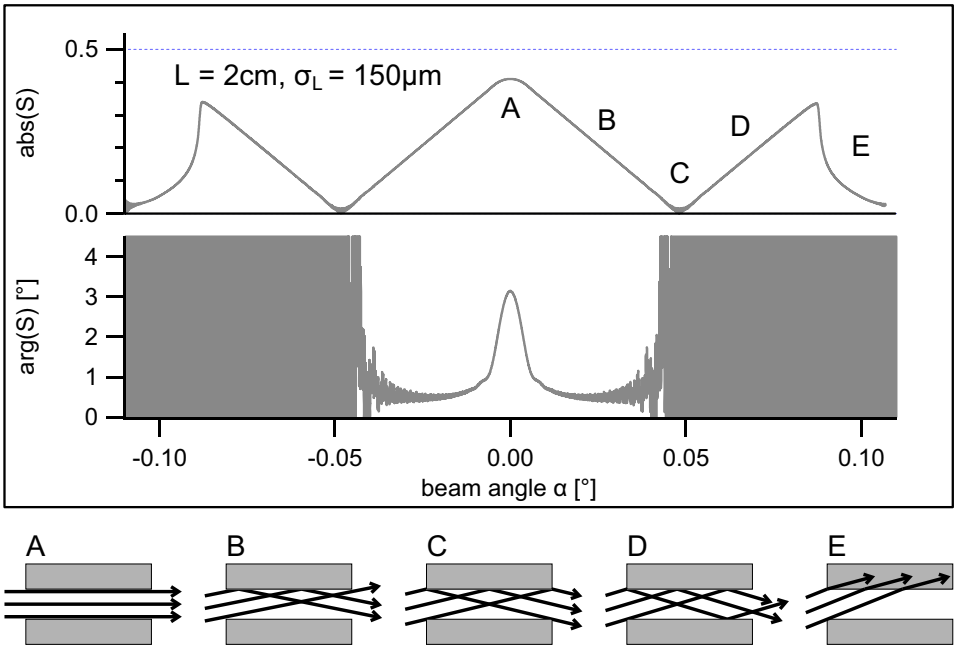

Figure 2.8: Transmission amplitude abs(S) and phase shift arg(S) with suppressed wall contribution. The amplitude follows the classically expected behaviour of a channel with opaque walls. For $\alpha = 0$ the maximum intensity can pass the channel (A). It is half the intensity compared to figure 2.7 because it doesn't contain the wall contribution. With increasing α the intensity decreases because the beam is partly reflected (B). When α reaches the channel diagonal at 0.048° the whole beam is reflected and the forward intensity is zero (C). For greater angles the intensity increases again because of double reflection (D). Now the optical path length stronly depends on α and the phase oscillates very fast. At $\alpha = 0.088°$ the critical angle of total reflection is reached and the beam starts penetrating the silicon (E).

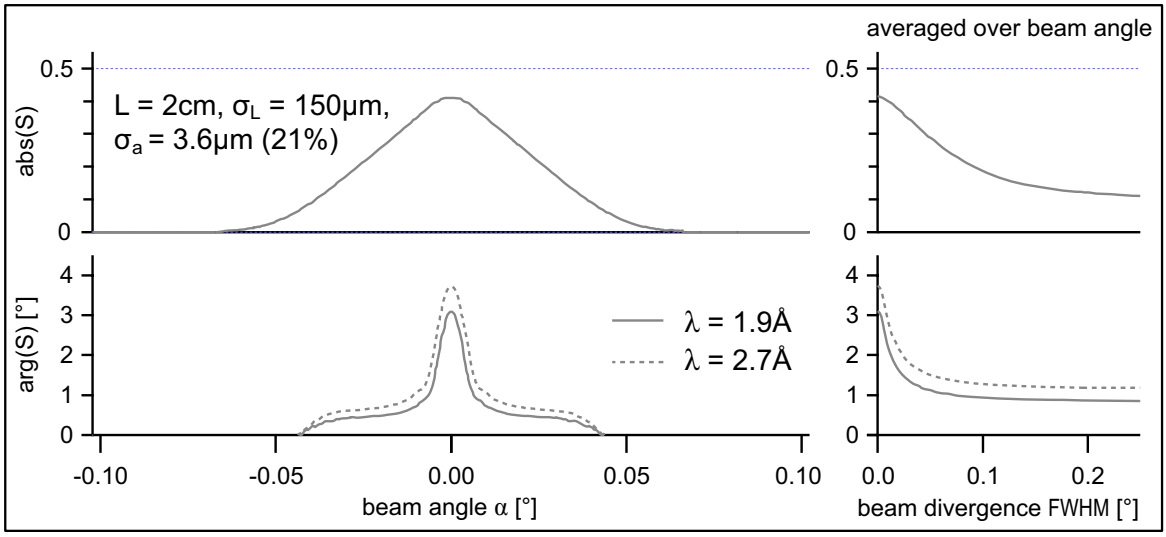

Figure 2.9: Transmission abs(S) and phase shift arg(S) for varying channel width and length. The largest phase contribution comes from well aligned neutrons ($\alpha \approx 0$) which hardly touch the walls. The measurement would reveal an average value due to the beam divergence.

The levels in the silicon walls have a large Δk_n and are strongly suppressed by the factor $\exp(-\frac{1}{2}(\Delta k_n \sigma_L)^2)$ while the small phase shifts of the channels are hardly affected. The result is shown in figure 2.8 and can be understood easily as explained in the figure caption.

The mean channel width a is 17μm but varies by about 21% ($=\sigma_a/a$). The averaging of S over this distribution can only be done numerically. The result is shown in figure 2.9. The strongly oscillating part of the double reflected beam is smeared out completely.

The typical beam divergence in an experiment is about $\pm 0.1^\circ$ to $\pm 0.5^\circ$. Therefore the measurement should reveal the average of S over that angle range. Table 2.1 gives the averaged values for a beam divergence of 0.2° for different wave lengths λ and channel lengths L. The other parameters have been set to $\sigma_L = 150\mu$m, $a = 17\mu$m, $\sigma_a = 3.6\mu$m, taken from the real channel stacks, see figure 3.10.

	$L=1$cm	$L=2$cm
$\lambda = 1.9$Å	0.53°	0.87°
$\lambda = 2.7$Å	0.70°	1.19°

Table 2.1: Calculated phase shift values for the real experiments.

At the very beginning of this chapter we calculated the phase shift in a very simple model without beam divergence, with infinite potentials and without the knowledge of the excitation amplitudes in each level. For comparison these values are re-calculated for the above values of λ, a and L and shown in table 2.2.

	$n=1$		$n=2$		$n=3$	
	$L=1$cm	$L=2$cm	$L=1$cm	$L=2$cm	$L=1$cm	$L=2$cm
$\lambda = 1.9$Å	0.30°	0.59°	1.18°	2.37°	2.66°	5.32°
$\lambda = 2.7$Å	0.42°	0.84°	1.68°	3.36°	3.78°	7.57°

Table 2.2: Calculated phase shift contributions of single levels n for an incident plane wave with $\alpha = 0$.

2.2 Wave Function behind the Channels

Now we have calculated the wave function within the channels. What happens when the neutrons leave the channels? A purely numerical solution of the wave function behind the channels can be calculated by Huygen's principle. If the wave function $\tilde{\psi}(\tilde{x}, \tilde{y})$ in known at the plane $z = \tilde{z}$ then the wave function for $z > \tilde{z}$ can be calculated by integration over spherical waves coming from each point of the $\tilde{z}$ plane.

$$\psi(x,y,z) = c \int d\tilde{x} \int d\tilde{y}\, \tilde{\psi}(\tilde{x},\tilde{y}) \frac{\mathrm{e}^{\mathrm{i}kr}}{r}, \quad \text{with} \quad r = \sqrt{(x-\tilde{x})^2 + (y-\tilde{y})^2 + (z-\tilde{z})^2} \tag{2.33}$$

The normalization constant c is equal to $\frac{k}{2\pi\mathrm{i}} = \frac{1}{\lambda\mathrm{i}}$, see [Pér96]. In our case ψ does not depend on y and the $\tilde{y}$ integration can be done immediately.

$$\psi(x,z) = \frac{k}{2\pi\mathrm{i}} \int d\tilde{x} \underbrace{\int d\tilde{y}\, \frac{\mathrm{e}^{\mathrm{i}kr}}{r}}_{I_y} \tilde{\psi}(\tilde{x}) \tag{2.34}$$

$$I_y = \int_{-\infty}^{\infty} d\tilde{y}\, \frac{\mathrm{e}^{\mathrm{i}kr}}{r} \qquad r^2 = \tilde{y}^2 + a^2, \qquad a^2 := (x-\tilde{x})^2 + (z-\tilde{z})^2 \tag{2.35}$$

$$= 2\int_{0}^{\infty} d\tilde{y}\, \frac{\mathrm{e}^{\mathrm{i}kr}}{r} \qquad r dr = \tilde{y} d\tilde{y}, \quad \int_0^\infty d\tilde{y} \to \int_a^\infty dr \tag{2.36}$$

$$= 2\int_{a}^{\infty} dr\, \frac{\mathrm{e}^{\mathrm{i}kr}}{\sqrt{r^2-a^2}} \qquad \to \text{Mathematica} \tag{2.37}$$

$$= \pi\,\mathrm{i}\,\mathrm{H}_0^{(1)}(ak) \qquad \mathrm{H}_0^{(1)} = \text{first Hankel function} = \mathrm{J}_0(ak) + \mathrm{i}\mathrm{Y}_0(ak) \tag{2.38}$$

$$\psi(x,z) = \frac{k}{2}\int_{\tilde{x}_1}^{\tilde{x}_2} d\tilde{x}\, \tilde{\psi}(\tilde{x})\, \mathrm{H}_0^{(1)}(k\sqrt{(x-\tilde{x})^2 + (z-\tilde{z})^2}) \tag{2.39}$$

We can use this formula to calculate the outgoing wave function ψ_{out} from the channel wave function ψ_{ch} (2.21) at the end of the channel $z = L$.

$$\psi_{out}(x,z) = \frac{k}{2}\int_{\tilde{x}_1}^{\tilde{x}_2} d\tilde{x}\, \psi_{ch}(\tilde{x}, L)\, \mathrm{H}_0^{(1)}(k\sqrt{(x-\tilde{x})^2 + (z-L)^2}) \tag{2.40}$$

Figure 2.10 gives a few examples for the wave function behind the channel.

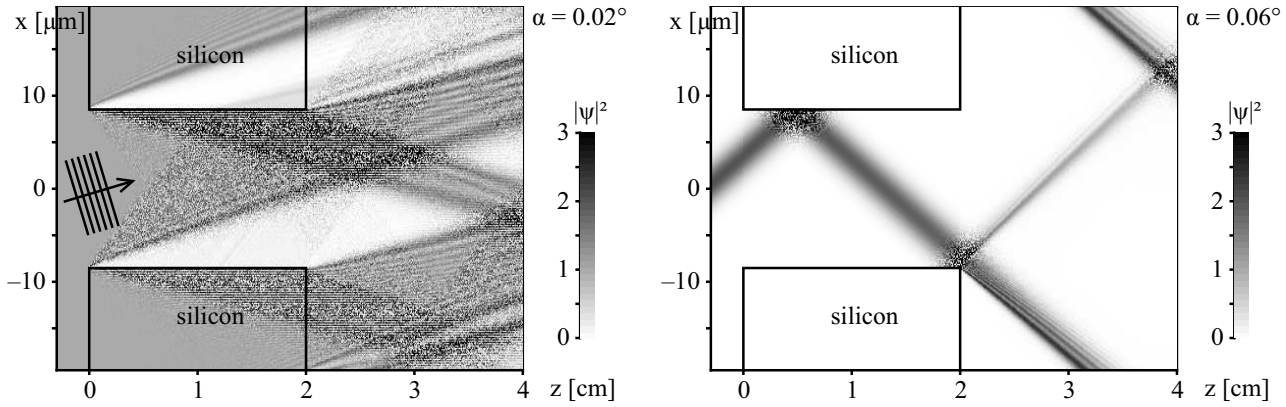

Figure 2.10: The wave intensity in the space behind the channel, calculated by Huygens principle. As a consequence of the periodic boundary conditions the beam which is leaving the picture at the bottom is entering again on top. This can be avoided by using the multiple cell solution described in section 2.6. The calculation of the localized beam is described in section 2.4.

2.3 Diffraction by the Channels

A more elegant way to calculate the wave function behind the channels is expanding the channel wave function in the plane wave solutions of the free space. Let's assume again an incoming plane wave. Then we can calculate the transition amplitude $S(\alpha, \widetilde{\alpha})$ from the incident angle α to any diffraction angle $\widetilde{\alpha}$.

If we introduce the periodic boundary conditions of the channel also to the free space behind the channels we have a set of discrete plane wave states $\exp(\mathrm{i}\vec{\widetilde{k}}_m\vec{r})$ with the direction $\widetilde{\alpha}_m = \arcsin(\widetilde{k}_{x,m}/k)$.

$$\widetilde{k}_{x,m} = m2\pi/(lN) = k\sin\widetilde{\alpha}_m, \qquad N = \text{number of cells (2.60)} \tag{2.41}$$

$$\widetilde{k}_{z,m} = \sqrt{k^2 - \widetilde{k}_{x,m}^{\,2}} = k\cos\widetilde{\alpha}_m \tag{2.42}$$

$$|\psi_{out}\rangle = \sum_{m=-M}^{M} S_m(\alpha, \widetilde{\alpha}_m)\,|\psi_{out,m}\rangle, \qquad |\psi_{out,m}\rangle = \mathrm{e}^{\mathrm{i}\widetilde{k}_{x,m}x}\,\mathrm{e}^{\mathrm{i}\widetilde{k}_{z,m}z} \tag{2.43}$$

$$S_m(\alpha, \widetilde{\alpha}_m) = \langle\psi_{out,m}|\psi_{ch}\rangle_{z=L} = \frac{1}{lN}\int dx\ \mathrm{e}^{-\mathrm{i}kx\sin\widetilde{\alpha}_m}\,\mathrm{e}^{-\mathrm{i}kL\cos\widetilde{\alpha}_m}\sum_n u_n(\alpha)\psi_{x,n}(x)\,\mathrm{e}^{\mathrm{i}k_{z,n}L} \tag{2.44}$$

$$= \sum_n u_n(\alpha)\,u_n^*(\widetilde{\alpha}_m)\ \mathrm{e}^{\mathrm{i}(k_{z,n}-k\cos\widetilde{\alpha}_m)L} \tag{2.45}$$

If we allow continuous directions of outgoing plane waves we get

$$|\psi_{out}\rangle = \int d\widetilde{\alpha}\ S(\alpha, \widetilde{\alpha})\ \mathrm{e}^{\mathrm{i}k\,x\sin\widetilde{\alpha}}\,\mathrm{e}^{\mathrm{i}k\,z\cos\widetilde{\alpha}} \tag{2.46}$$

$$|\psi_{ch}\rangle_{z=L} = |\psi_{out}\rangle_{z=L} \tag{2.47}$$

$$\sum_n u_n(\alpha)\psi_n(x)\,\mathrm{e}^{\mathrm{i}k_{z,n}L} = \int d\widetilde{\alpha}\ S(\alpha, \widetilde{\alpha})\ \mathrm{e}^{\mathrm{i}kx\sin\widetilde{\alpha}}\,\mathrm{e}^{\mathrm{i}kL\cos\widetilde{\alpha}} \qquad \Big|\cdot\,\mathrm{e}^{-\mathrm{i}kx\sin\beta}$$

$$\sum_n u_n(\alpha)\psi_n(x)\,\mathrm{e}^{-\mathrm{i}kx\sin\beta}\,\mathrm{e}^{\mathrm{i}k_{z,n}L} = \int d\widetilde{\alpha}\ S(\alpha, \widetilde{\alpha})\ \mathrm{e}^{\mathrm{i}kL\cos\widetilde{\alpha}}\ \mathrm{e}^{\mathrm{i}kx(\sin\widetilde{\alpha}-\sin\beta)} \qquad \Big|\tfrac{1}{l}\textstyle\int dx\cdot$$

$$\sum_n u_n(\alpha)\underbrace{\frac{1}{l}\int_{-l/2}^{l/2} dx\ \psi_n(x)\,\mathrm{e}^{-\mathrm{i}kx\sin\beta}}_{u_n^*(\beta)}\,\mathrm{e}^{\mathrm{i}k_{z,n}L} = \int d\widetilde{\alpha}\ S(\alpha, \widetilde{\alpha})\ \mathrm{e}^{\mathrm{i}kL\cos\widetilde{\alpha}}\ \underbrace{\frac{1}{l}\int_{-l/2}^{l/2} dx\ \mathrm{e}^{\mathrm{i}kx(\sin\widetilde{\alpha}-\sin\beta)}}_{\xrightarrow{l\gg\lambda}\ \lambda\,\delta(\sin\widetilde{\alpha}-\sin\beta)} \tag{2.48}$$

$$\sum_n u_n(\alpha)\,u_n^*(\beta)\,\mathrm{e}^{\mathrm{i}k_{z,n}L} = S(\alpha, \beta)\ \mathrm{e}^{\mathrm{i}kL\cos\beta}\ \frac{\lambda}{l} \tag{2.49}$$

$$S(\alpha, \widetilde{\alpha}) = \frac{l}{\lambda}\sum_n u_n(\alpha)\,u_n^*(\widetilde{\alpha})\,\mathrm{e}^{\mathrm{i}L(k_{z,n}-k\cos\widetilde{\alpha})} \tag{2.50}$$

The continuous (2.50) and the discrete solution (2.45) differ only by the norm factor l/λ.

The absolute value of $S(\alpha, \widetilde{\alpha})$ is shown in the top of figure 2.13 and in figure 2.11 a) and can be understood as a diffraction pattern. If we calculate formula (2.45) for $V_0 \to \infty$, $L \to 0$, $\alpha = 0$ and $\widetilde{\alpha} \ll 1$ we get the well known diffraction formula of a slit of the width a:

$$|S(0, \widetilde{\alpha})| \to \frac{a}{l}\left|\mathrm{sinc}\frac{\pi\,a\,\widetilde{\alpha}}{\lambda}\right|, \qquad \mathrm{sinc}\,x \equiv \frac{\sin x}{x} \tag{2.51}$$

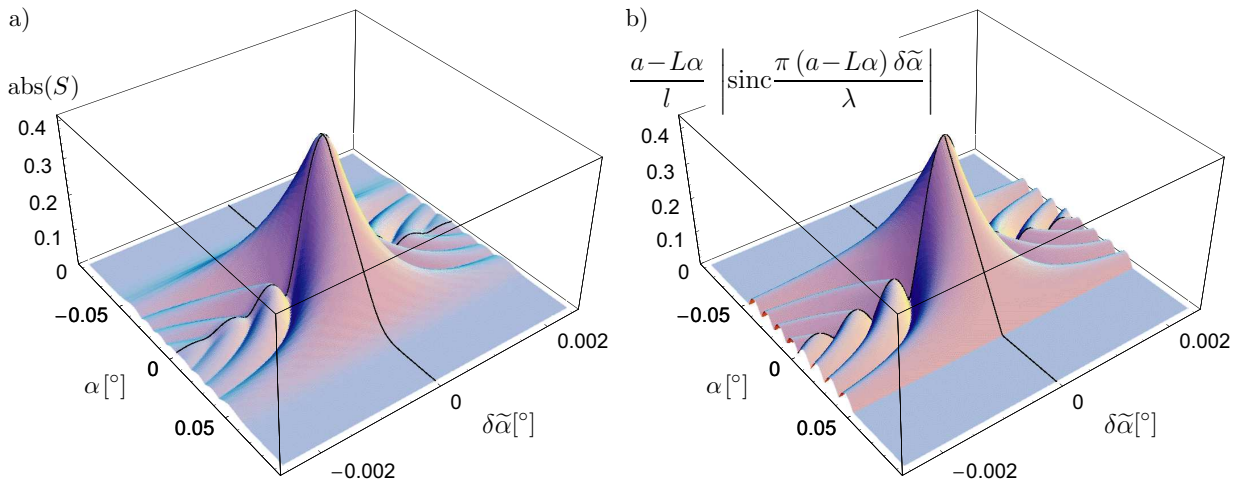

Figure 2.11: a) Numerical calculation of the absolute value of the diffraction factor $S(\alpha, \widetilde{\alpha})$, formula (2.45). α denotes the incident angle, $\widetilde{\alpha}$ the exit angle and $\delta\widetilde{\alpha} = \widetilde{\alpha} - \alpha$ the diffraction angle.
b) Diffraction pattern of a slit, see formula (2.52).

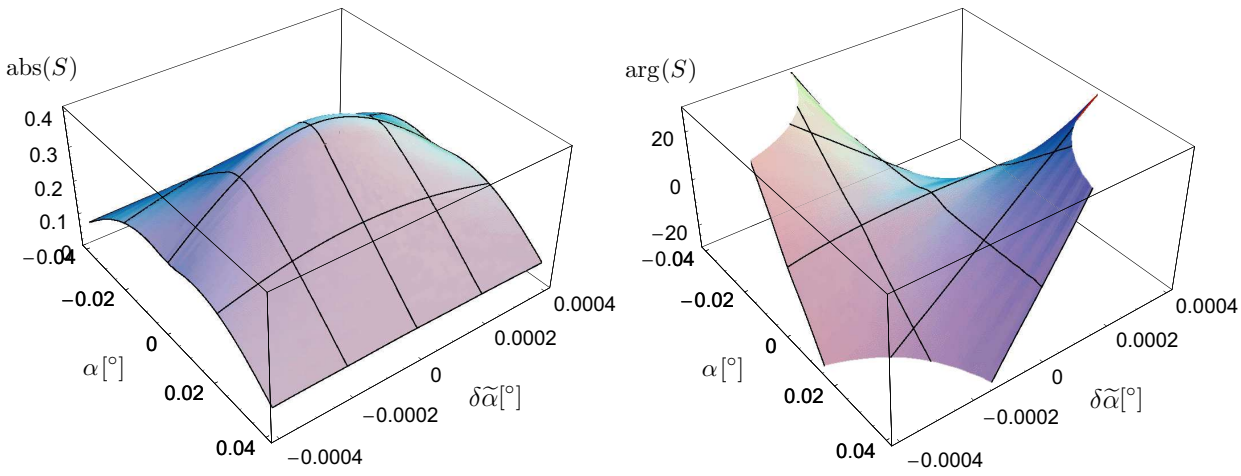

Figure 2.12: Magnification of the central area of $S(\widetilde{\alpha}, \alpha)$. Figure 2.9 would be a cut at $\delta\widetilde{\alpha} = 0$.

We can extend this formula for the case $L \neq 0$ and $\alpha \neq 0$ by substituting a by the effective slit width $a - L\alpha$.

$$|S(\alpha, \widetilde{\alpha})| \approx \frac{a - L\alpha}{l} \left| \mathrm{sinc} \frac{\pi\,(a - L\alpha)\,\delta\widetilde{\alpha}}{\lambda} \right|, \qquad \delta\widetilde{\alpha} := \widetilde{\alpha} - \alpha \tag{2.52}$$

This formula is plotted in figure 2.11 b) and reproduces quite well the numerical result shown in figure 2.11 a). With increasing $|\alpha|$ the effective slit width decreases which means less intensity and larger diffraction angles. Figure 2.13 displays a few cuts for different values of α. A magnification of the central region is shown in figure 2.12.

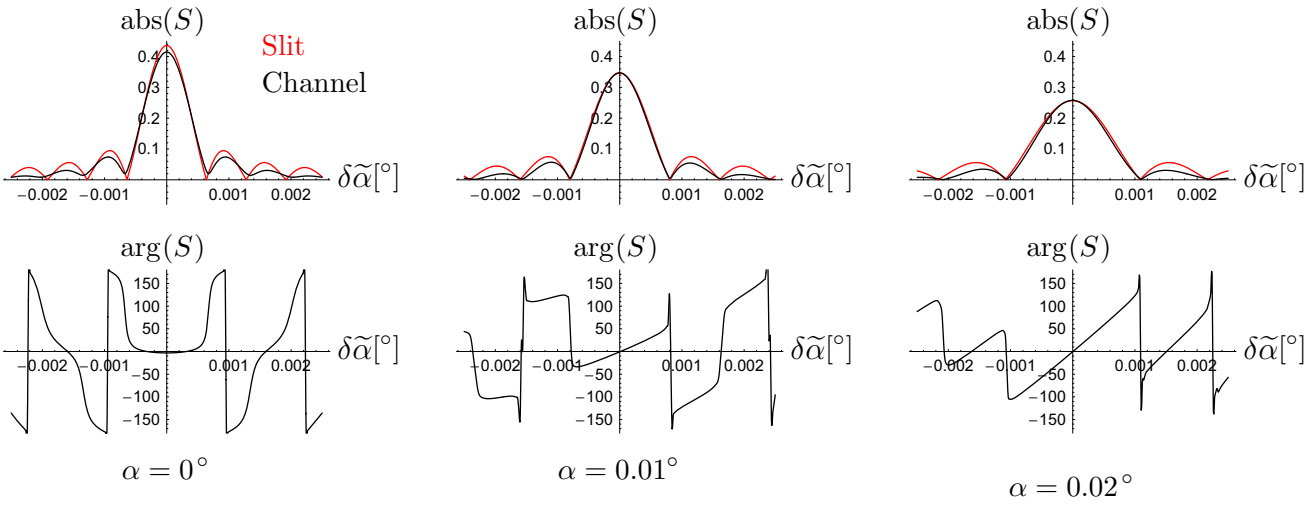

Figure 2.13: Plots of $S(\widetilde{\alpha}, \alpha)$ for different values of α. The diffraction pattern of a slit (2.52) is shown by the red line.

2.4 Localized Beam

A localized beam can be generated by a coherent superposition of monochromatic plane waves with slightly different angles and an appropriate weight function. By chosing the width of the angle distribution and the distance of the source one can control the beam width δx and the beam position x_0 at the channel entrance. See section 6.1 for details. We can write the incident beam as

$$\psi_{in} = \int d\alpha \underbrace{\frac{1}{\sqrt{2\pi}\,\sigma_\alpha} \exp\left(-\frac{(\alpha - \alpha_0)^2}{2\sigma_\alpha^2}\right) \exp\left(-\mathrm{i}\vec{k}\vec{r}_0\right)}_{g(\alpha)} \underbrace{\exp\left(\mathrm{i}\vec{k}\vec{r}\right)}_{\psi_\alpha} \tag{2.53}$$

In a similar way we can apply all plane wave results obtained so far to a beam, e.g. $|\psi_{ch}\rangle = \int d\alpha\, g(\alpha)\, |\psi_{ch}(\alpha)\rangle$. Figure 2.14 gives two examples for a beam width of 32μm and 4μm. These beams represent only a coherent package of the real neutron beam. The complete description of the beam would be an incoherent superposition of many of such packages.

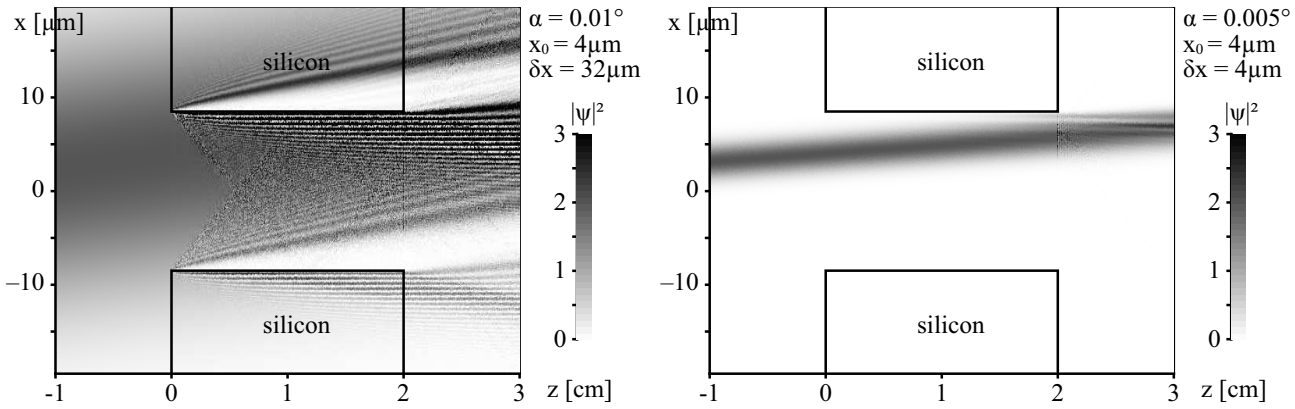

Figure 2.14: A broad beam with $\delta x = 32\mu$m (FWHM) and a narrow beam with $\delta x = 4\mu$m entering the channel at $x_0 = 4\mu$m.

2.5 Phase Shift of a Localized Beam

Let's calculate the phase shift of a localized beam given by (2.53). We will denote the phase factor of a single plane wave component by $S(\alpha)$ and the total phase factor by plain S.

$$|\psi_{in}\rangle = \int d\alpha\, g(\alpha)|\psi_\alpha\rangle \tag{2.54}$$

$$|\psi_{out}\rangle = \int d\alpha\, g(\alpha)S(\alpha)|\psi_\alpha\rangle \tag{2.55}$$

$$S = \langle\psi_{in}|\psi_{out}\rangle = \int d\alpha'\, g^*(\alpha') \int d\alpha\, g(\alpha)S(\alpha)\underbrace{\langle\psi'_\alpha|\psi_\alpha\rangle}_{\delta(\alpha-\alpha')} = \int d\alpha\, |g(\alpha)|^2\, S(\alpha) \tag{2.56}$$

This factor S depends on the beam width δx, the beam entry point x_0 and the beam direction α_0 which all enter in $g(\alpha)$. Figures 2.15 and 2.16 show plots of S versus x_0 and α_0 for two different beam widths. If the beam is narrow and does not touch the wall ($\alpha_0 \approx 0$, $x_0 = 0$) we get the classical behaviour which means that there is full intensity (abs(S)) and no phase shift ($\arg(S) = 0$), see figure 2.16. As we cannot control the beam position we have to average over x_0. This has been done numerically and is shown by the small inserts in the figures. If we average coherently we get the plane wave result, which is not a big surprise, because a coherent superposition of beams results again in a plane wave. If we average incoherently, which is probably more in accordance with the real beam nature, we get the same phase shift and only a difference in the intensity. This is good news because it means that we don't have to care so much about the coherence properties of the beam. The reason behind this is derived in section 5.4 in the interferometer theory chapter.

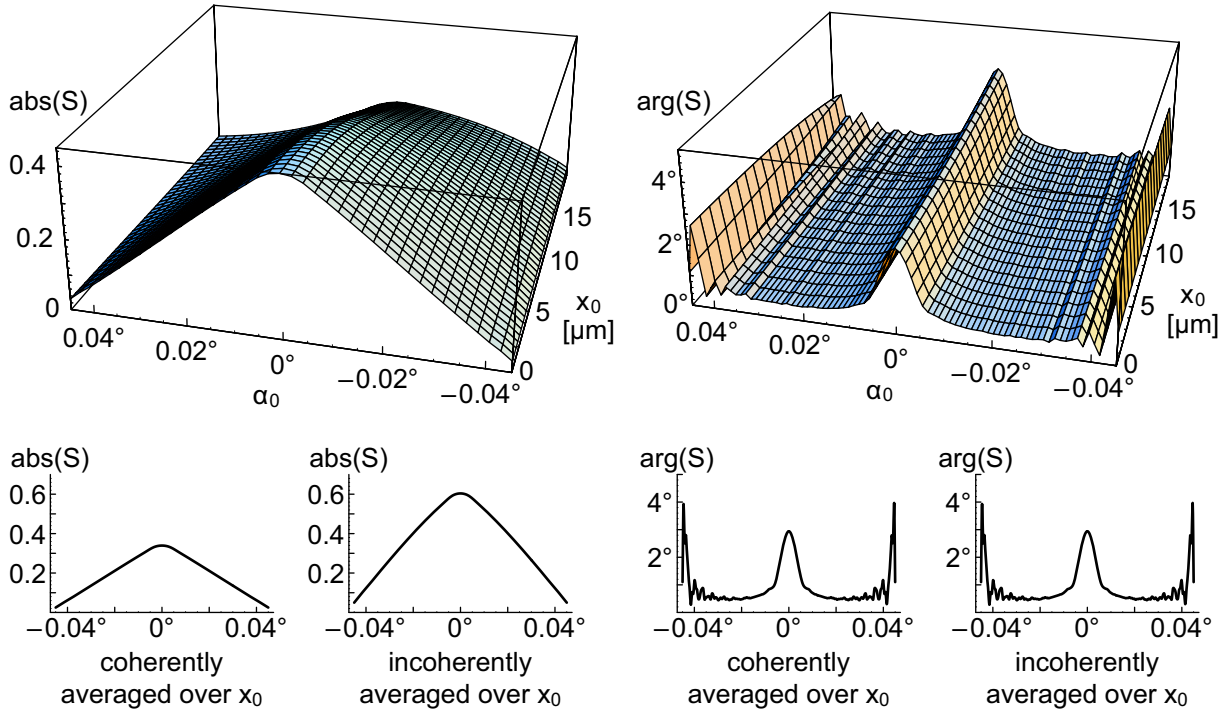

Figure 2.15: Phase factors for a beam of 32 μm width which is comparable to the channel width. Consequently there is no strong dependence on the entry position x_0.

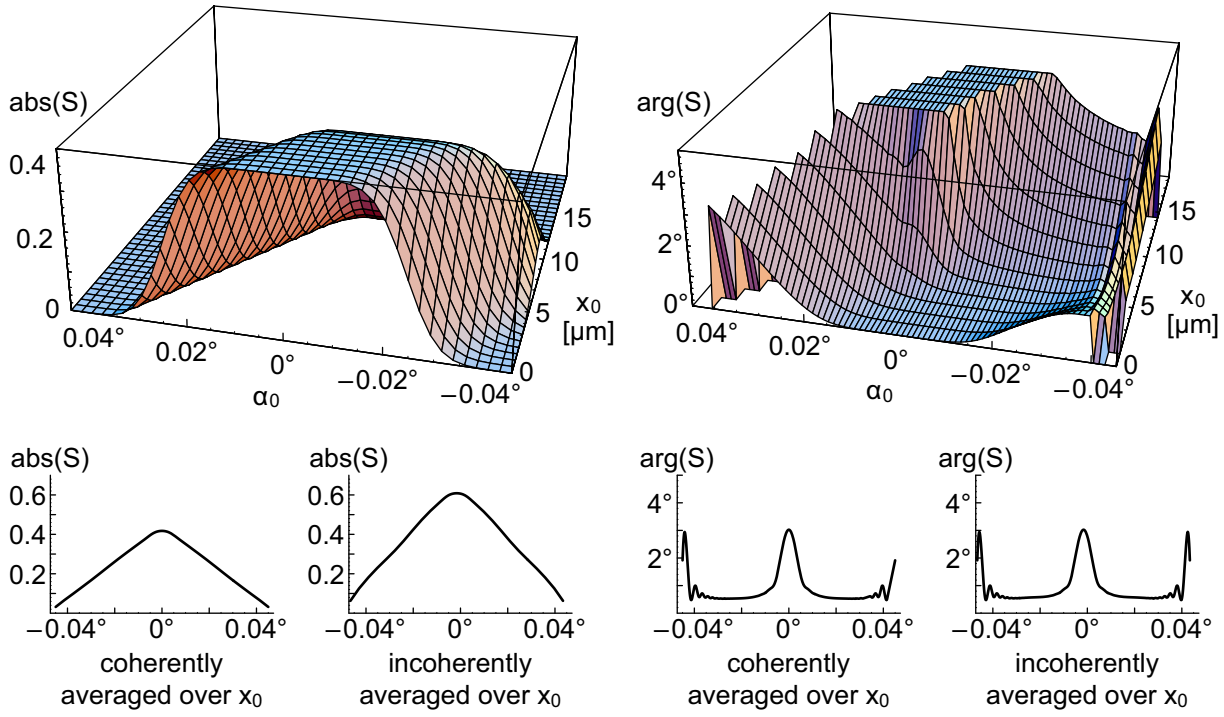

Figure 2.16: Phase factors for a beam width of 4 μm width which is clearly smaller than the channel width. The dependence on the entry position x_0 is appaerent. Nevertheless we get the plane wave result after averaging over x_0.

2.6 Wave Function for Multiple Cells

Above we have calculated the wave function for a single cell of the periodic potential. Now we start again with (2.3) and figure 2.2 but assume N cells. The Bloch theorem states that for a periodic potential $V(x) = V(x+l)$ the wave function is equal in each cell up to a phase factor $\exp(\mathrm{i}ql)$ between the cells.

$$\psi(x) = \mathrm{e}^{\mathrm{i}qx}u(x) \tag{2.57}$$
$$u(x+l) = u(x) \tag{2.58}$$
$$\psi(x+l) = \mathrm{e}^{\mathrm{i}ql}\psi(x) = \mathrm{e}^{\mathrm{i}ql}\,\mathrm{e}^{\mathrm{i}qx}u(x+l) \tag{2.59}$$
$$q = \frac{\nu\,2\,\pi}{Nl}, \qquad \nu = 0, 1, \ldots N-1, \qquad N = \text{number of cells} \tag{2.60}$$

q describes a standing wave within the entire group of cells. If we add $Q = 2\pi/(Nl)$ to q we get the same phase factor $\exp(\mathrm{i}ql)$ and thus the same solution for ψ. This means that there are exactly N different values of q. Each level of the single cell solution corresponds to a group of N sublevels in the multi cell solution. q is smaller than Q which means that the wave length λ_q of the standing wave is larger than the width l of a single cell.

The wave function $\psi(x)$ should be smooth on each cell boundary. Because of (2.57) this must also be true for $u(x)$.

$$u(x+l) = u(x), \qquad u'(x+l) = u'(x) \tag{2.61}$$

With this result we can calculate the derivative ψ' and get

$$\psi(x+l) = \psi(x)\,\mathrm{e}^{\mathrm{i}ql}, \qquad \psi'(x+l) = \psi'(x)\,\mathrm{e}^{\mathrm{i}ql}. \tag{2.62}$$

Ansatz with $k = \sqrt{2mE/\hbar^2}$ and $K = \sqrt{2m(E-V_0)/\hbar^2}$:

$$\psi_{\text{cell}\,0}(x) = \begin{cases} \psi_{\mathrm{I}}(x) = A\,\mathrm{e}^{\mathrm{i}kx} + B\,\mathrm{e}^{-\mathrm{i}kx} & \text{for } -\frac{a}{2} < x < \frac{a}{2} \\ \psi_{\mathrm{II}}(x) = C\,\mathrm{e}^{\mathrm{i}K(x-l/2)} + D\,\mathrm{e}^{-\mathrm{i}K(x-l/2)} & \text{for } \frac{a}{2} < x < l - \frac{a}{2} \end{cases} \tag{2.63}$$
$$\psi_{\text{cell}j}(x) = \psi_{\text{cell}\,0}(x - j\,l)\;\mathrm{e}^{-\mathrm{i}\,qj\,l} \tag{2.64}$$

Solving the matching conditions

$$\psi_{\mathrm{I}}(a/2) = \psi_{\mathrm{II}}(a/2) \qquad \psi_{\mathrm{I}}(-a/2) = \psi_{\mathrm{II}}(l - a/2)\,\mathrm{e}^{-\mathrm{i}ql} \tag{2.65}$$
$$\psi'_{\mathrm{I}}(a/2) = \psi'_{\mathrm{II}}(a/2) \qquad \psi'_{\mathrm{I}}(-a/2) = \psi'_{\mathrm{II}}(l - a/2)\,\mathrm{e}^{-\mathrm{i}ql} \tag{2.66}$$

leads to the eigenvalue equation

$$\cos(ka)\cos(Ks) - \tfrac{k^2+K^2}{2kK}\sin(ka)\sin(Ks) = \cos(ql) \tag{2.67}$$

with q given by (2.60). The cosine term $\cos(ql) = \cos(2\pi\nu/N)$ has arguments in the range of 0 to 2π. Because the cosine function is symmetric around π we get for $\nu > N/2$ the same eigenvalues as for $N-\nu$. Therefore it is sufficient to look for eigenvalues in the range $\nu \le N/2$ and take into account the following degeneration:

$$\nu = 0 \qquad \text{no degeneration} \tag{2.68}$$
$$0 < \nu < N/2 \qquad \text{two fold degeneration} \tag{2.69}$$
$$\nu = N/2 \qquad \text{no degeneration, exists only for even } N \tag{2.70}$$

The relations between the coefficients can be reduced to

$$A = F\,(k-K)(\cos(ql+ka)-\cos(Ks)) \tag{2.71}$$
$$B = F\,(k+K)(\cos(ql)-\cos(ka+Ks)) \tag{2.72}$$
$$C = G\,(k-K)(\cos(ka)-\cos(ql+Ks)) \tag{2.73}$$
$$D = G\,(k+K)(\cos(ql)-\cos(ka+Ks)) \tag{2.74}$$
$$\frac{G}{F} = \frac{D}{B} = \mathrm{e}^{\mathrm{i}ql/2}\frac{(k+K)\sin(ka)}{2K\sin\frac{ka-ql-Ks}{2}} = \mathrm{e}^{\mathrm{i}ql/2}\frac{-2k\sin\frac{ka+ql-Ks}{2}}{(k+K)\sin(Ks)}. \tag{2.75}$$

The normalization

$$1 = \frac{1}{l}\int_{-a/2}^{-a/2+l}|\psi(x)|^2dx = \underbrace{\frac{1}{l}\int_{-a/2}^{a/2}|\psi_{\mathrm{I}}(x)|^2dx}_{I_1} + \underbrace{\frac{1}{l}\int_{-s/2}^{s/2}|\psi_{\mathrm{II}}(x+l/2)|^2dx}_{I_2} \tag{2.76}$$
$$I_1 = \frac{\sin(ka)\,(BA^*+AB^*)+ka\,(AA^*+BB^*)}{kl} \tag{2.77}$$
$$I_2 = \frac{\sin(Ks)\,(DC^*+CD^*)+Ks\,(CC^*+DD^*)}{Kl} \tag{2.78}$$

leads to

$$\frac{1}{FF^*} = \frac{a}{l}\left(u^2+v^2+2uv\frac{\sin(ka)}{ka}\right)+\frac{s}{l}y^2\left(u^2+w^2+2uw\frac{\sin(Ks)}{Ks}\right) \tag{2.79}$$
$$u := (k+K)\,(\cos(ql)-\cos(ka+Ks)) \tag{2.80}$$
$$v := (k-K)\,(\cos(ka+ql)-\cos(Ks)) \tag{2.81}$$
$$w := (k-K)\,(\cos(ka)-\cos(ql+Ks)) \tag{2.82}$$
$$y := \frac{2\sin\frac{ka+ql-Ks}{2}}{(1+K/k)\sin(Ks)} \tag{2.83}$$

$$\frac{GG^*}{FF^*} = \frac{(k+K)^2\sin(ka)^2}{4K^2\sin(\frac{ka-ql-Ks}{2})^2} = \frac{4k^2\sin(\frac{ka+ql-Ks}{2})^2}{(k+K)^2\sin(Ks)^2} = \frac{k\sin(ka)\sin(\frac{ka+ql-Ks}{2})}{K\sin(Ks)\sin(\frac{ka-ql-Ks}{2})}. \tag{2.84}$$

The excitation of level n for a potential with N cells, indexed by $j = 0, 1, ...N-1$:

$$u_n = \langle\psi_n|\psi_{in}\rangle_{z=0} = \frac{1}{Nl}\int_{\text{cells}}\psi_n^*(x,z=0)\;\psi_{in}(x,z=0)\;dx \tag{2.85}$$
$$= \frac{1}{Nl}\sum_{j=0}^{N-1}\int_{-a/2}^{l-a/2}\psi_{n,\text{cell}\,0}^*(x)\;\mathrm{e}^{-\mathrm{i}\,qj\,l}\;\mathrm{e}^{\mathrm{i}h(x+j\,l)}\,dx \tag{2.86}$$
$$= \frac{1}{Nl}\left(\sum_{j=0}^{N-1}\mathrm{e}^{\mathrm{i}j\,l(h-q)}\right)\underbrace{\int_{-a/2}^{l-a/2}\psi_{n,\text{cell}\,0}^*(x)\,\mathrm{e}^{\mathrm{i}hx}dx}_{I_0} \tag{2.87}$$

$$I_0 = a\left(A^*\frac{\sin\frac{a(h-k)}{2}}{\frac{a(h-k)}{2}} + B^*\frac{\sin\frac{a(h+k)}{2}}{\frac{a(h+k)}{2}}\right) + \mathrm{e}^{\mathrm{i}\frac{hl}{2}}s\left(C^*\frac{\sin\frac{s(h-K)}{2}}{\frac{s(h-K)}{2}} + D^*\frac{\sin\frac{s(h+K)}{2}}{\frac{s(h+K)}{2}}\right) \tag{2.88}$$

The formulas above could be used directly for the bound states by replacing K by $\mathrm{i}\kappa$. However, numerical problems arise if the functions sinh, cosh and exp are used with large arguments. That's why it is better to start again with the ansatz:

$$\psi_{\mathrm{I}}(x) = A\ \mathrm{e}^{\mathrm{i}kx} + B\ \mathrm{e}^{-\mathrm{i}kx} \tag{2.89}$$

$$\psi_{\mathrm{II}}(x) = \overline{C}\ \mathrm{e}^{-\kappa(x-a/2)} + \overline{D}\ \mathrm{e}^{\kappa(x-a/2-s)} \tag{2.90}$$

Eigenvalue equation:

$$(k-\kappa)^2\sin(ka)\tanh(\kappa s) - 2k\kappa\left[\cos(ka) - \cos(ql)/\cosh(\kappa s)\right] = 0 \tag{2.91}$$

Relations between the coefficients:

$$A = \overline{F}\,2k\kappa\,(1-\cos(ka+ql)/\cosh(\kappa s)) \tag{2.92}$$

$$B = \overline{F}\,(k^2+\kappa^2)\sin(ka)\tanh(\kappa s)) \tag{2.93}$$

$$\overline{C} = \overline{G}\,2k\kappa\left[\cos(ql) - \cos(ka)/\cosh(\kappa s) - \mathrm{i}\sin(ql)\tanh(\kappa s)\right] \tag{2.94}$$

$$\overline{D} = \overline{G}\,(k^2+\kappa^2)\sin(ka)\tanh(\kappa s)) \tag{2.95}$$

$$\frac{\overline{G}}{\overline{F}} = \frac{\overline{D}}{B} = \mathrm{e}^{\mathrm{i}ql/2}\,2k\,\frac{\mathrm{i}\sin\frac{ka+ql}{2} + \cos\frac{ka+ql}{2}\tanh\frac{\kappa s}{2}}{(k+\mathrm{i}\kappa)(1-\mathrm{e}^{-\kappa s})} = \frac{\mathrm{e}^{\mathrm{i}ql/2}\,(k+\mathrm{i}\kappa)\,\sin(ka)}{\kappa(1+\mathrm{e}^{-\kappa s})\left(\mathrm{i}\sin\frac{ka-ql}{2} + \cos\frac{ka-ql}{2}\tanh\frac{\kappa s}{2}\right)}$$

Calculating the normalization (2.76) leads to

$$I_1 = \frac{\sin(ka)\,(BA^*+AB^*) + ka\,(AA^*+BB^*)}{kl} \tag{2.97}$$

$$\overline{I_2} = \frac{\sinh(\kappa s)\,(\overline{C}\overline{C}^*+\overline{D}\overline{D}^*) + \kappa s\,(\overline{D}\overline{C}^*+\overline{C}\overline{D}^*)}{\kappa l\,\mathrm{e}^{\kappa s}} \tag{2.98}$$

and

$$\frac{1}{\overline{F}\overline{F}^*} = \frac{a}{l}\left\{u^2+v^2+\frac{\sin(ka)}{ka}\left[2uv + \frac{k^2v}{\kappa^2u}\left(u^2+w^2+2uw\frac{\kappa s}{\sinh(\kappa s)}+y^2\right)\right]\right\} \tag{2.99}$$

$$u := (k^2+\kappa^2)\sin(ka)\tanh(\kappa s) \tag{2.100}$$

$$v := 2k\kappa\left(1 - \frac{\cos(ka+ql)}{\cosh(\kappa s)}\right) \tag{2.101}$$

$$w := 2k\kappa\left(\cos(ql) - \frac{\cos(ka)}{\cosh(\kappa s)}\right) \tag{2.102}$$

$$y := 2k\kappa\sin(ql)\tanh(\kappa s). \tag{2.103}$$

$$\frac{\overline{G}\overline{G}^*}{\overline{F}\overline{F}^*} = \frac{\mathrm{e}^{\kappa s}(k^2+\kappa^2)\sin(ka)^2}{2\kappa^2\,(\cosh(\kappa s) - \cos(ka-ql))} = \frac{2k^2\,\mathrm{e}^{\kappa s}\,(\cosh(\kappa s) - \cos(ka+ql))}{(k^2+\kappa^2)\sinh(\kappa s)^2} \tag{2.104}$$

The excitation is given by (2.87) and

$$I_0 = a\left(A^*\frac{\sin\frac{a(h-k)}{2}}{\frac{a(h-k)}{2}} + B^*\frac{\sin\frac{a(h+k)}{2}}{\frac{a(h+k)}{2}}\right) + \mathrm{e}^{\mathrm{i}\frac{hl}{2}}s\left(1+\mathrm{e}^{-\kappa s}\right)\cdot$$
$$\cdot\left(\overline{C}^*\frac{\sin\frac{hs}{2} + \mathrm{i}\cos\frac{hs}{2}\tanh\frac{\kappa s}{2}}{h+\mathrm{i}\kappa} + \overline{D}^*\frac{\sin\frac{hs}{2} - \mathrm{i}\cos\frac{hs}{2}\tanh\frac{\kappa s}{2}}{h-\mathrm{i}\kappa}\right). \tag{2.105}$$

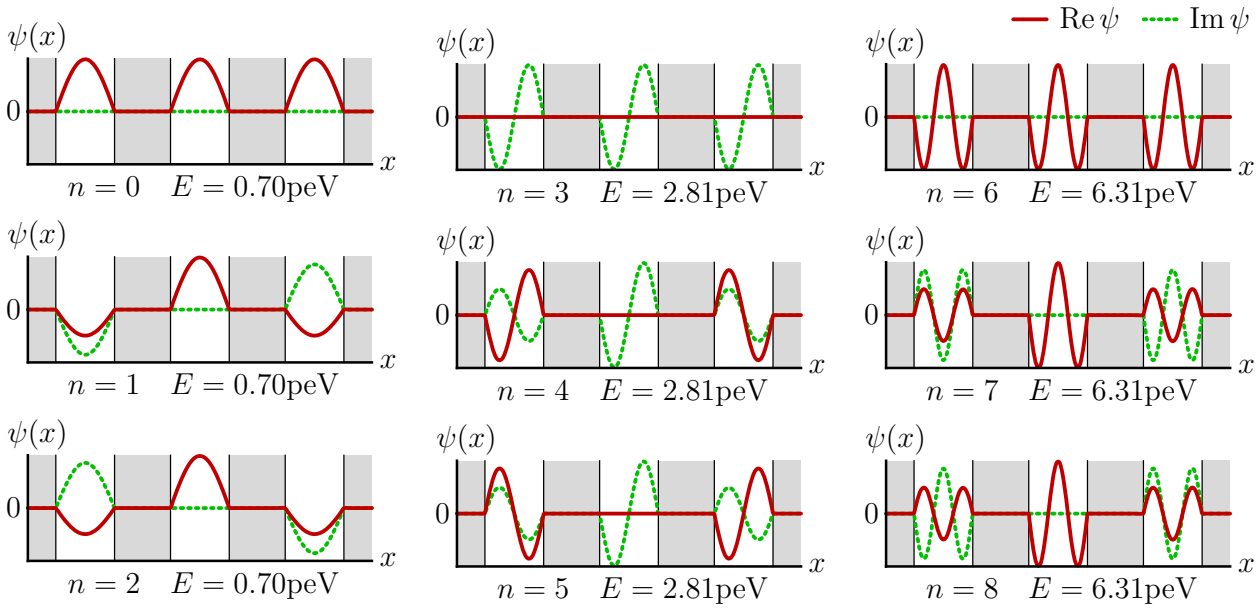

Figure 2.17: The wave functions of the first nine energy levels calculated for three cells. The energy values for e.g. $n = 0$ and $n = 1$ are in principle different but cannot be distinguished by the numerical precision.

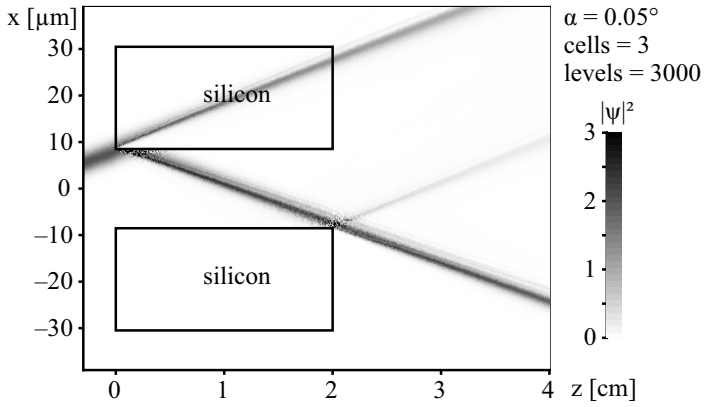

Figure 2.18: A beam falling onto the edge of the silicon wall is partly reflected, partly refracted. The interval of periodicity contains three channels, prohibiting the artefacts of figure 2.10.

Figure 2.17 shows the wave functions of the first levels for three cells. An illustration of a multi-cell solution is given in figure 2.18.

The multi-cell approach is not necessary for the calculation of the confinement induced phase, because this phase is dominated by the very lowest levels of the potential well. These levels are virtually not affected by the neighbour channels because their energy is much less than the potential step. Therefore the single-cell approach is sufficient.

2.7 Absorber Coated Channels

The phase shift calculations in section 2.1.2 have shown that the largest phase contribution comes from neutrons which are well aligned to the channel direction ($\alpha = 0$) and hardly touch the walls, as shown in the phase shift distribution at the bottom of figure 2.9. Because of the beam divergence a realistic experiment would always reveal the average value of this distribution. In this section we want to check if the contributions of $\alpha \neq 0$ could be attenuated by applying absorbing layers onto the channel walls. The idea is that the more the neutrons are misaligned the more they would touch the walls and be absorbed.

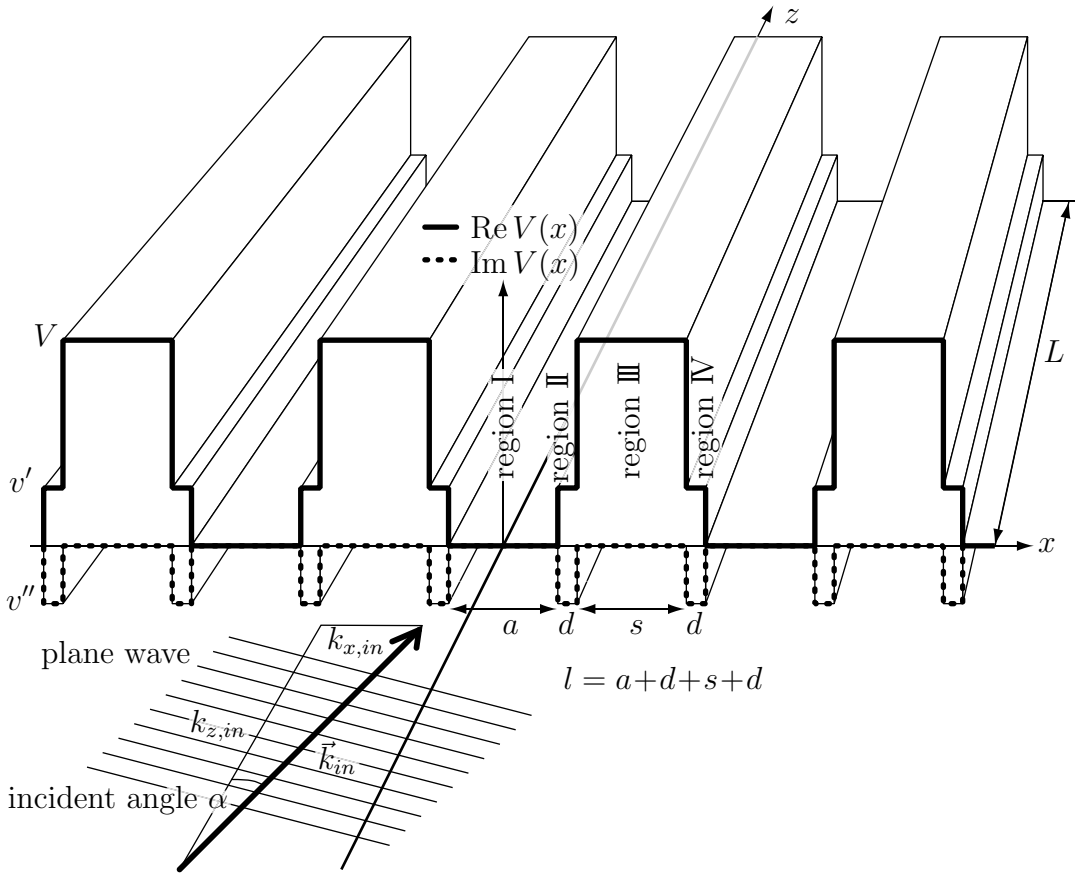

Figure 2.19: The periodic potential of the channel stack with absorber coated walls. The absorber is represented by a complex potential.

$$V(x) = \begin{cases} 0 & -\frac{a}{2} < x \leq \frac{a}{2} & \text{region I, channel} \\ v = v' + \mathrm{i}v'' & \frac{a}{2} < x \leq \frac{a}{2}+d & \text{region II, absorbing layer} \\ V & \frac{a}{2}+d < x \leq \frac{a}{2}+d+s & \text{region III, wall material} \\ v = v' + \mathrm{i}v'' & -\frac{a}{2}-d < x \leq -\frac{a}{2} & \text{region IV, absorbing layer} \end{cases} \tag{2.106}$$

In the calculation the absorbing layer is represented by a region with a complex potential, as shown in figure 2.19. The potential of a material is given by $V = 4\pi\hbar^2 N b_c/(2m)$. The coherent scattering length b_c is tabulated for different nuclides [HJ01] and has a complex value for absorbers with a negative imaginary part. N is the particle density, m the neutron mass.

Why does a complex potential lead to absorption? Let's have a look at the equations for the time and x dependent parts of the wave function, (2.4) and (2.3). If $V(x)$ is complex then the eigenvalues E_x of equation (2.3) will become complex too, $E_x = E'_x + \mathrm{i}E''_x$, and we get for the time dependent part

$$\psi_t = \exp\bigl(-\mathrm{i}(E_x+E_z)t/\hbar\bigr) = \exp\bigl(-\mathrm{i}(E'_x+E_z)t/\hbar\bigr)\,\exp\bigl(E''_x\,t/\hbar\bigr) \tag{2.107}$$

Only the real value E'_x represents the energy. The imaginary part E''_x changes the amplitude in time. For $E''_x < 0$ the amplitude will decrease which means absorption. The time t in $\exp(E''_x\,t/\hbar)$ is the time the neutron spends in the channel. Because the neutrons are moving basically in z direction ($E_z \gg E'_x$) we can write $t = z/v_z = zm/(\hbar k_z)$

$$\exp\bigl(E''_x\,t/\hbar\bigr) = \exp\bigl(E''_x\,m\,z/(\hbar^2 k_z)\bigr) \tag{2.108}$$

For all further calculations we will write E instead of E_x.

The calculation is done in the following order. We solve the x part of the Schrödinger equation and get a series of complex eigenvalues E_n and eigenfunctions $\psi_{x,n}(x)$. Then the z component is given by $\psi_{z,n} = \exp(\mathrm{i}k_{z,n}z)$ with $k_{z,n} = \sqrt{2m(E_{in}-E'_n)/\hbar^2}$. The complete channel wave function is given by the superposition of all levels n with the amplitudes u_n. Including the absoption factor we get:

$$\psi_{ch}(x,z) = \sum_n u_n \psi_{x,n}(x)\exp(\mathrm{i}k_{z,n}z)\exp(E''_n m z/(\hbar^2 k_{z,n})) \tag{2.109}$$

2.7.1 Eigenvalues

The **ansatz** for equation (2.3) using the potential (2.106) reads:

$$-\tfrac{a}{2} \le x < \tfrac{a}{2}: \quad \psi_{\mathrm{I}}(x) = A\,\mathrm{e}^{\mathrm{i}kx} + B\,\mathrm{e}^{-\mathrm{i}kx} \qquad k = \sqrt{2mE/\hbar^2} \tag{2.110}$$

$$\tfrac{a}{2} \le x < \tfrac{a}{2}+d: \quad \psi_{\mathrm{II}}(x) = Q\,\mathrm{e}^{\mathrm{i}\kappa(x-\frac{a}{2})} + R\,\mathrm{e}^{-\mathrm{i}\kappa(x-\frac{a}{2})} \qquad \kappa = \sqrt{2m(E-v'-\mathrm{i}v'')/\hbar^2}$$

$$\tfrac{a}{2}+d \le x < \tfrac{a}{2}+d+s: \quad \psi_{\mathrm{III}}(x) = C\,\mathrm{e}^{\mathrm{i}K(x-\frac{l}{2})} + D\,\mathrm{e}^{-\mathrm{i}K(x-\frac{l}{2})} \qquad K = \sqrt{2m(E-V)/\hbar^2} \tag{2.112}$$

$$-\tfrac{a}{2}-d \le x < -\tfrac{a}{2}: \quad \psi_{\mathrm{IV}}(x) = S\,\mathrm{e}^{\mathrm{i}\kappa(x+\frac{a}{2})} + T\,\mathrm{e}^{-\mathrm{i}\kappa(x+\frac{a}{2})} \qquad E, v, k, \kappa, K \in \mathbb{C} \tag{2.113}$$

The wave function and its derivative must be continuous:

$$\psi_{\mathrm{I}}(\tfrac{a}{2}) = \psi_{\mathrm{II}}(\tfrac{a}{2}): \quad A\,\mathrm{e}^{\mathrm{i}k\frac{a}{2}} + B\,\mathrm{e}^{-\mathrm{i}k\frac{a}{2}} = Q + R \tag{2.114}$$

$$\psi'_{\mathrm{I}}(\tfrac{a}{2}) = \psi'_{\mathrm{II}}(\tfrac{a}{2}): \quad k(A\,\mathrm{e}^{\mathrm{i}k\frac{a}{2}} - B\,\mathrm{e}^{-\mathrm{i}k\frac{a}{2}}) = (Q-R)\kappa \tag{2.115}$$

$$\psi_{\mathrm{II}}(\tfrac{a}{2}+d) = \psi_{\mathrm{III}}(\tfrac{a}{2}+d): \quad Q\,\mathrm{e}^{\mathrm{i}\kappa d} + R\,\mathrm{e}^{-\mathrm{i}\kappa d} = C\,\mathrm{e}^{-\mathrm{i}K\frac{s}{2}} + D\,\mathrm{e}^{\mathrm{i}K\frac{s}{2}} \tag{2.116}$$

$$\psi'_{\mathrm{II}}(\tfrac{a}{2}+d) = \psi'_{\mathrm{III}}(\tfrac{a}{2}+d): \quad \kappa(Q\,\mathrm{e}^{\mathrm{i}\kappa d} - R\,\mathrm{e}^{-\mathrm{i}\kappa d}) = (C\,\mathrm{e}^{-\mathrm{i}K\frac{s}{2}} - D\,\mathrm{e}^{\mathrm{i}K\frac{s}{2}})K \tag{2.117}$$

$$\psi_{\mathrm{III}}(\tfrac{a}{2}+d+s) = \psi_{\mathrm{IV}}(-\tfrac{a}{2}-d): \quad C\,\mathrm{e}^{\mathrm{i}K\frac{s}{2}} + D\,\mathrm{e}^{-\mathrm{i}K\frac{s}{2}} = S\,\mathrm{e}^{-\mathrm{i}\kappa d} + T\,\mathrm{e}^{\mathrm{i}\kappa d} \tag{2.118}$$

$$\psi'_{\mathrm{III}}(\tfrac{a}{2}+d+s) = \psi'_{\mathrm{IV}}(-\tfrac{a}{2}-d): \quad K(C\,\mathrm{e}^{\mathrm{i}K\frac{s}{2}} - D\,\mathrm{e}^{-\mathrm{i}K\frac{s}{2}}) = (S\,\mathrm{e}^{-\mathrm{i}\kappa d} - T\,\mathrm{e}^{\mathrm{i}\kappa d})\kappa \tag{2.119}$$

$$\psi_{\mathrm{IV}}(-\tfrac{a}{2}) = \psi_{\mathrm{I}}(-\tfrac{a}{2}): \quad S + T = A\,\mathrm{e}^{-\mathrm{i}k\frac{a}{2}} + B\,\mathrm{e}^{\mathrm{i}k\frac{a}{2}} \tag{2.120}$$

$$\psi'_{\mathrm{IV}}(-\tfrac{a}{2}) = \psi'_{\mathrm{I}}(-\tfrac{a}{2}): \quad \kappa(S-T) = (A\,\mathrm{e}^{-\mathrm{i}k\frac{a}{2}} - B\,\mathrm{e}^{\mathrm{i}k\frac{a}{2}})k \tag{2.121}$$

One of the eight constants $A \ldots D$ and $Q \ldots T$ is arbitrary and can be calculated later by normalization. Eliminating the other seven constants leaves one equation which is the eigenvalue

equation for E where k, K, and κ depend on.

$$\left((\kappa-k)(\kappa+K)\sin\frac{(ka-2\kappa d-Ks)}{2}-(\kappa+k)(\kappa-K)\sin\frac{(ka+2\kappa d-Ks)}{2}\right)= \\ =\mp\left((\kappa-k)(\kappa-K)\sin\frac{(ka-2\kappa d+Ks)}{2}-(\kappa+k)(\kappa+K)\sin\frac{(ka+2\kappa d+Ks)}{2}\right) \quad (2.122)$$

There are again two classes of solutions ($\mp$) which refer to the symmetric and the antisymmetric states of the wave function $\psi_x(x)$.

• symmetric case: $(2.122)^-$

$$\cos(\kappa d)\left[k\sin\tfrac{ka}{2}\cos\tfrac{Ks}{2}+K\sin\tfrac{Ks}{2}\cos\tfrac{ka}{2}\right]+\tfrac{1}{\kappa}\sin(\kappa d)\left[\kappa^2\cos\tfrac{ka}{2}\cos\tfrac{Ks}{2}-k\sin\tfrac{ka}{2}\;K\sin\tfrac{Ks}{2}\right]=0 \quad (2.123)$$

$$\psi_{\rm I}(x)=A\cos(kx) \quad (2.124)$$
$$\psi_{\rm II}(x)=A\left[\cos\tfrac{ka}{2}\cos\left(\kappa(x-\tfrac{a}{2})\right)-\tfrac{k}{\kappa}\sin\tfrac{ka}{2}\sin\left(\kappa(x-\tfrac{a}{2})\right)\right]= \quad (2.125)$$
$$=C\left[\cos\tfrac{Ks}{2}\cos\left(\kappa(x-\tfrac{l}{2}+\tfrac{s}{2})\right)+\tfrac{K}{\kappa}\sin\tfrac{Ks}{2}\sin\left(\kappa(x-\tfrac{l}{2}+\tfrac{s}{2})\right)\right] \quad (2.126)$$
$$\psi_{\rm III}(x)=C\cos\left(K(x-\tfrac{l}{2})\right) \quad (2.127)$$
$$\psi_{\rm IV}(x)=\psi_{\rm II}(-x) \quad (2.128)$$
$$\psi(x)=\psi(-x) \quad (2.129)$$

$$\frac{C}{A}=\frac{-k\sin\frac{ka}{2}\sin(\kappa d)+\kappa\cos\frac{ka}{2}\cos(\kappa d)}{\kappa\cos\frac{Ks}{2}}=\frac{\kappa\cos\frac{ka}{2}}{-K\sin\frac{Ks}{2}\sin(\kappa d)+\kappa\cos\frac{Ks}{2}\cos(\kappa d)}= \quad (2.130)$$
$$=\frac{-k\sin\frac{ka}{2}\cos(\kappa d)-\kappa\cos\frac{ka}{2}\sin(\kappa d)}{K\sin\frac{Ks}{2}}=\frac{k\sin\frac{ka}{2}}{-K\sin\frac{Ks}{2}\cos(\kappa d)-\kappa\cos\frac{Ks}{2}\sin(\kappa d)}$$

• antisymmetric case: $(2.122)^+$

$$\cos(\kappa d)\left[\tfrac{1}{k}\sin\tfrac{ka}{2}\cos\tfrac{Ks}{2}+\tfrac{1}{K}\sin\tfrac{Ks}{2}\cos\tfrac{ka}{2}\right]+\tfrac{1}{\kappa}\sin(\kappa d)\left[\cos\tfrac{ka}{2}\cos\tfrac{Ks}{2}-\kappa^2\tfrac{1}{k}\sin\tfrac{ka}{2}\;\tfrac{1}{K}\sin\tfrac{Ks}{2}\right]=0 \quad (2.131)$$

$$\psi_{\rm I}(x)=A\sin(kx) \quad (2.132)$$
$$\psi_{\rm II}(x)=A\left[\sin\tfrac{ka}{2}\cos\left(\kappa(x-\tfrac{a}{2})\right)+\tfrac{k}{\kappa}\cos\tfrac{ka}{2}\sin\left(\kappa(x-\tfrac{a}{2})\right)\right]= \quad (2.133)$$
$$=C\left[-\sin\tfrac{Ks}{2}\cos\left(\kappa(x-\tfrac{l}{2}+\tfrac{s}{2})\right)+\tfrac{K}{\kappa}\cos\tfrac{Ks}{2}\sin\left(\kappa(x-\tfrac{l}{2}+\tfrac{s}{2})\right)\right] \quad (2.134)$$
$$\psi_{\rm III}(x)=C\sin\left(K(x-\tfrac{l}{2})\right) \quad (2.135)$$
$$\psi_{\rm IV}(x)=-\psi_{\rm II}(-x) \quad (2.136)$$
$$\psi(x)=-\psi(-x) \quad (2.137)$$

$$\frac{C}{A}=\frac{-k\cos\frac{ka}{2}\sin(\kappa d)-\kappa\sin\frac{ka}{2}\cos(\kappa d)}{\kappa\sin\frac{Ks}{2}}=\frac{\kappa\sin\frac{ka}{2}}{-K\cos\frac{Ks}{2}\sin(\kappa d)-\kappa\sin\frac{Ks}{2}\cos(\kappa d)}= \quad (2.138)$$
$$=\frac{+k\cos\frac{ka}{2}\cos(\kappa d)-\kappa\sin\frac{ka}{2}\sin(\kappa d)}{K\cos\frac{Ks}{2}}=\frac{k\cos\frac{ka}{2}}{+K\cos\frac{Ks}{2}\cos(\kappa d)-\kappa\sin\frac{Ks}{2}\sin(\kappa d)}$$

The equations (2.123) and (2.131) must be solved numerically and give the set of eigenvalues $E_{x,n}$ and eigenfunctions $\psi_{x,n}(x)$. One has to be careful with the numerical stability because of

the exponential behaviour of the hyperbolic part of the complex trigonometric functions:

$$\sin(a'+\mathrm{i}a'') = \cosh a'' \sin a' + \mathrm{i}\sinh a'' \cos a' \tag{2.139}$$
$$\cos(a'+\mathrm{i}a'') = \cosh a'' \cos a' - \mathrm{i}\sinh a'' \sin a' \tag{2.140}$$

In equations (2.123) and (2.131) this problem can be solved by dividing the equation by $\left(\cosh(\kappa'' d)\cosh\frac{k'' a}{2}\cosh\frac{K'' s}{2}\right)$ which just leaves real sin, cos and tanh functions. For ψ_{II} and C/A the different given expressions may help in different numerical situations.

Finding the complex eigenvalues is not trivial. One has to find the points in the complex plane of E where both the real and the imaginary part of the eigenvalue equation vanish. The plots of the real and imaginary parts each show a set of curves where these functions equal zero. The crossing points of these curves are the eigenvalues. See figure 2.20. The search for the crossing points has been programmed in C++. The algorithm works in the following way:

- Define a boundary rectangle in the complex plane which encloses the area where you expect the eigenvalues. The upper limit of the imaginary part is 0 because $\mathrm{Im}E < 0$ for absorption. The lower limit seems to be $\mathrm{Im}\, v$. (I have no proof for that.) The lower limit for the real part is given by the minimum of the real part of the potential, i.e. 0 or $\mathrm{Re}\, v$ if $\mathrm{Re}\, v < 0$. The upper limit depends on the number of energy levels you want to calculate and can be set to a few multiples of V.

- Find the roots of the real part of the eigenvalue equation along the boundary line. Move along the boundary line in small steps (chosen empirically) and evaluate the equation. Whenever the value changes sign we have a root in between the last two points of evaluation. Cutting this interval recursively into halves and evalutating the sign leads to the root. (Bisection methode, [PVTF02].)

- From the roots on the boundary line move along the zero lines into the boundary rectangle. Making a step along the zero line means making a step in an assumed direction and then looking again for the zero line perpendicular to the step direction. The assumed direction of the first step will be perpendicular to the boundary. The consecutive directions can be estimated from the preceding two points.

- While moving on the line where the real part of the equation is zero, evaluate the imaginary part. Whenever the sign of the imaginary part changes you can find the eigenvalue again by the bisection methode. Of course each bisection point has to be corrected to lie on the zero line of the real part.

- Continue on the zero line until you reach the boundary again. Remember this point and don't enter from here again.

This algorithm finds all eigenvalues in the given boundary rectangle as long as there are no circular zero lines which would not cross the border at any point. I plotted the equation for all sets of parameters I used, and I never found circles. So I guess that circles do not appear for this kind of equation.

Another methode would be to evaluate the absolute value of the equation as shown in figure 2.21, but I would expect two disadvantages here. First you have no guide lines to the eigenvalues. This means that you have to scan the whole area by tiny steps in two dimensions in order not to miss any eigenvalue. Second the absolute value just touches the zero point and

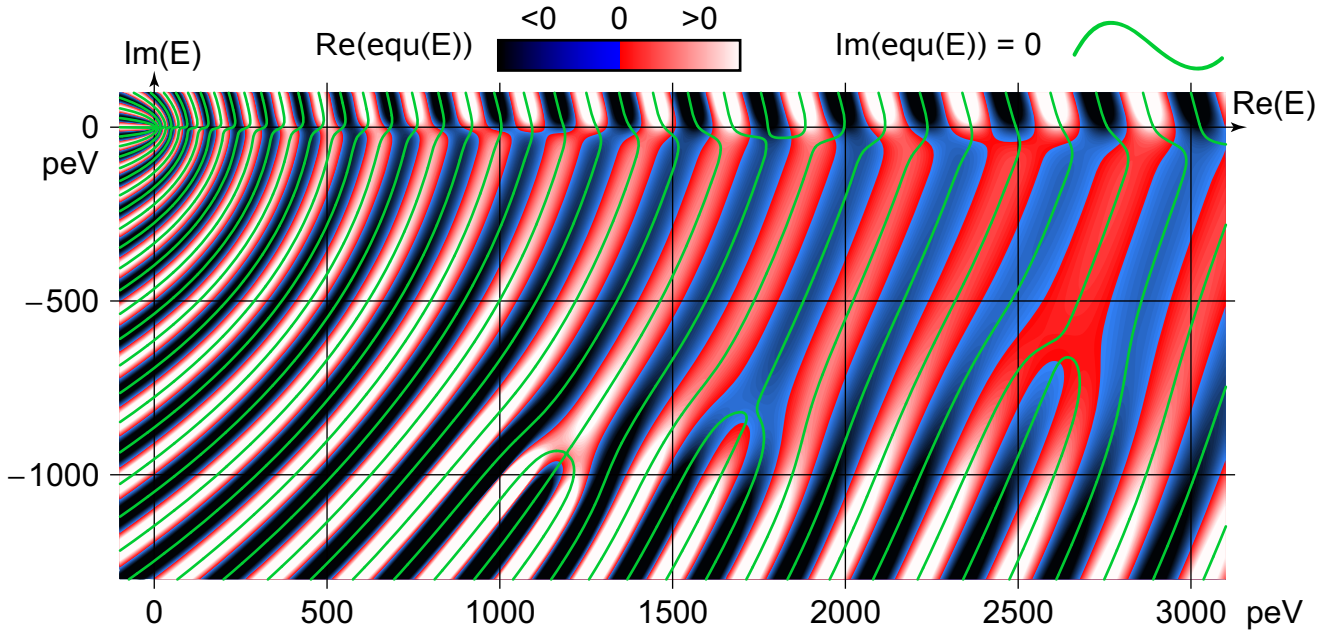

Figure 2.20: Plotting the real part of the eigenvalue equation in the complex plane we get a landscape of mountains (red) and valleys below sea level (blue). At the coast line the real part is zero. We can do the same for the imaginary part and get a second coast line which is shown here in green. The eigenvalues lie at the points where both coast lines cross each other. The numerical strategy to find the eigenvalues is explained in the text. This example plot shows the equation for the symmetric states for an absorber potential of $v = 1000 - 1000\mathrm{i}\,\mathrm{peV}$.

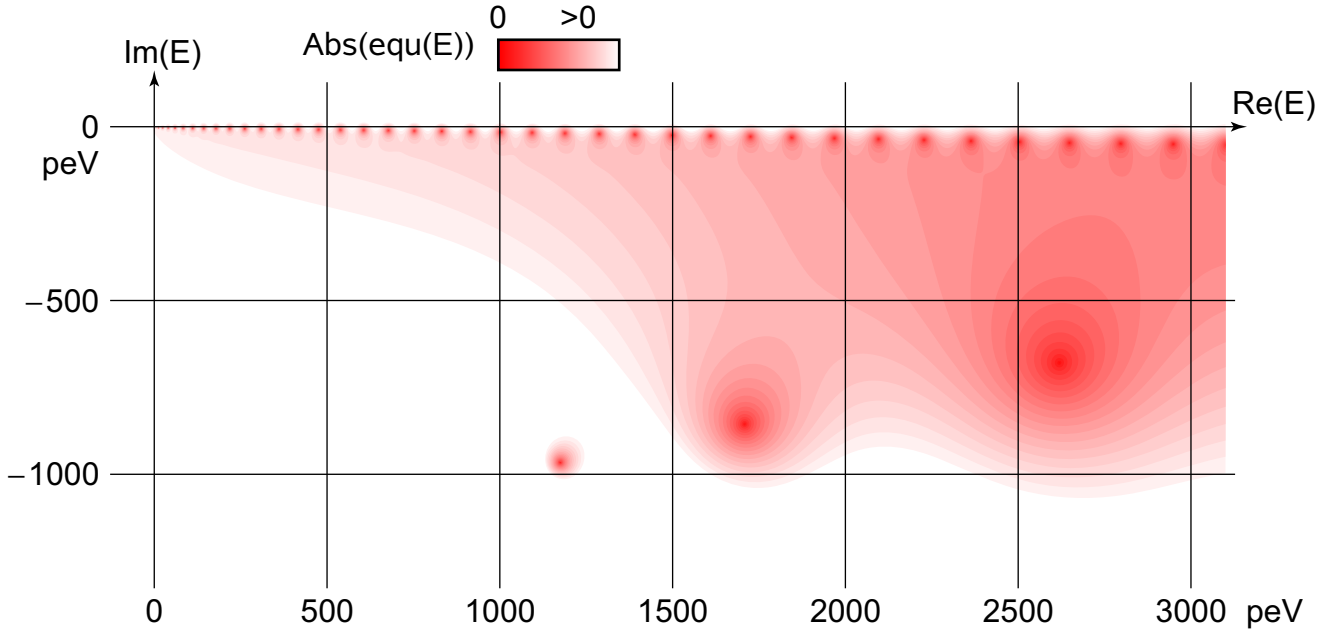

Figure 2.21: Plotting the absolute value of the eigenvalue equation shows the eigenvalues directly. However the numerical implementation would be more complicated and it would be difficult not to miss any eigenvalue.

does not cross it like an oscillating function. It is numerically more costly to find a touching point than a crossing point.

Figure 2.22 shows the eigenvalues for two example potentials plotted in the complex plane.

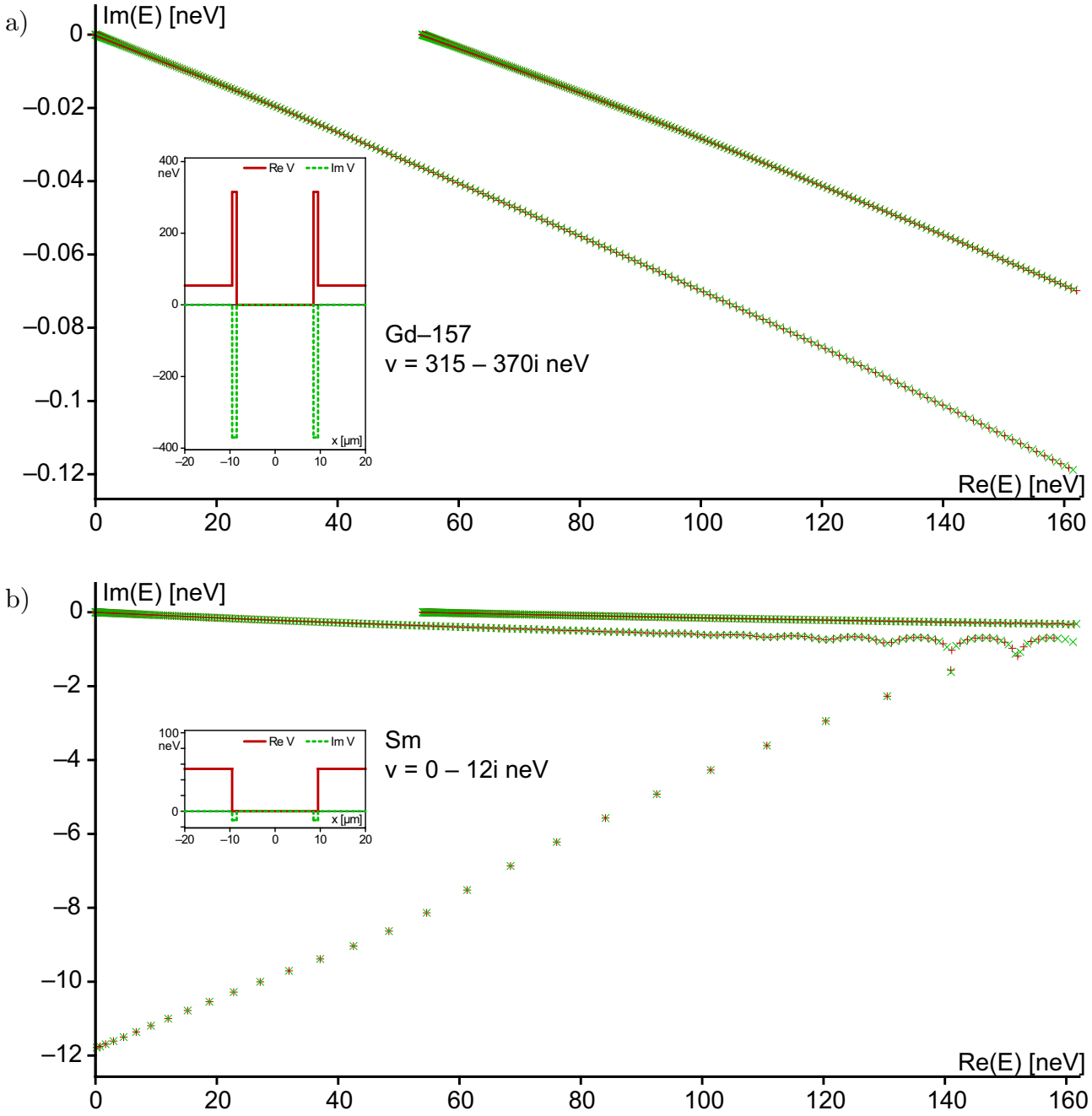

Figure 2.22: The eigenvalues for two different absorber materials, Gd-157 and Sm. The tiny red and green crosses show the symmetric and antisymmetric eigenvalues respectively. The group starting at the top left corner represents the bound states. At $\mathrm{Re}E > V_0 = 54\mathrm{neV}$ a second group comes in representing the free states. For a real potential both groups would lie on the real axis and mix up. That's why the free states in a real potential don't come in an alternating series of symmetric and antisymmetric eigenvalues but in an irregular order.

2.7.2 Orthogonality of the Eigenfunctions

As a consequence of the complex potential the Hamiltonian is no longer Hermitean which means that the eigenfunctions are not necessarily orthogonal. Therefore we have to check the orthogonality relation.

$$\langle\psi_n|\psi_m\rangle = \frac{1}{l}\int_{-l/2}^{l/2}\psi_n^*(x)\psi_m(x)dx \tag{2.141}$$

Case 1: ψ_n is symmetric and ψ_m is antisymmetric or vice versa. Then the integrand is antisymmetric and the result is zero because of the symmetric integration intervall. This means that symmetric and antisymmetric eigenfunctions are orthogonal to each other.

Case 2: Both ψ_n and ψ_m are symmetric or antisymmetric. Then the integrand is symmetric and we get:

$$\langle\psi_n|\psi_m\rangle = \frac{2}{l}\int_0^{l/2}\psi_n^*(x)\psi_m(x)dx \tag{2.142}$$

$$= \underbrace{\frac{2}{l}\int_0^{a/2}\psi_{\mathrm{I}n}^*(x)\psi_{\mathrm{I}m}(x)dx}_{I_1} + \underbrace{\frac{2}{l}\int_{a/2}^{a/2+d}\psi_{\mathrm{II}n}^*(x)\psi_{\mathrm{II}m}(x)dx}_{I_2} + \underbrace{\frac{2}{l}\int_{a/2+d}^{l/2}\psi_{\mathrm{III}n}^*(x)\psi_{\mathrm{III}m}(x)dx}_{I_3}$$

$$I_1 = \frac{A_m A_n^*}{l}\left(\frac{\sin\left(\frac{a}{2}(k_m - k_n^*)\right)}{k_m - k_n^*} \pm \frac{\sin\left(\frac{a}{2}(k_m + k_n^*)\right)}{k_m + k_n^*}\right) \qquad \pm \ldots \begin{smallmatrix}\text{symmetric}\\ \text{antisymm.}\end{smallmatrix} \tag{2.143}$$

$$I_3 = \frac{C_m C_n^*}{l}\left(\frac{\sin\left(\frac{s}{2}(K_m - K_n^*)\right)}{K_m - K_n^*} \pm \frac{\sin\left(\frac{s}{2}(K_m + K_n^*)\right)}{K_m + K_n^*}\right) \tag{2.144}$$

$$I_2 = \ldots = \text{with (2.130) and (2.138)} = -\frac{k_m^2 - k_n^{*2}}{\kappa_m^2 - \kappa_n^{*2}}\, I_1 - \frac{K_m^2 - K_n^{*2}}{\kappa_m^2 - \kappa_n^{*2}}\, I_3 \tag{2.145}$$

$$\langle\psi_n|\psi_m\rangle = \left(1 - \frac{k_m^2 - k_n^{*2}}{\kappa_m^2 - \kappa_n^{*2}}\right) I_1 + \left(1 - \frac{K_m^2 - K_n^{*2}}{\kappa_m^2 - \kappa_n^{*2}}\right) I_3 = \frac{v''\,(I_1 + I_3)}{v'' + \frac{\mathrm{i}}{2}(E_m - E_n^*)} \tag{2.146}$$

This means that the eigenfunctions $|\psi_n\rangle$ within the symmetric or antisymmetric subset are not orthogonal as long as the imaginary part v'' of the potential does not vanish.

2.7.3 Normalization

$$\langle\psi_n|\psi_n\rangle = 1 =$$

$$= \frac{1}{1 - E_n''/v''}\left\{\frac{|A_n|^2}{2l}\left(\frac{\sinh(ak_n'')}{k_n''} \pm \frac{\sin(ak_n')}{k_n'}\right) + \frac{|C_n|^2}{2l}\left(\frac{\sinh(sK_n'')}{K_n''} \pm \frac{\sin(sK_n')}{K_n'}\right)\right\} \tag{2.147}$$

$$|A_n|^2 = \frac{2l\,(1 - E_n''/v'')}{\left(\frac{\sinh(ak_n'')}{k_n''} \pm \frac{\sin(ak_n')}{k_n'}\right) + \left|\frac{C_n}{A_n}\right|^2\left(\frac{\sinh(sK_n'')}{K_n''} \pm \frac{\sin(sK_n')}{K_n'}\right)} \tag{2.148}$$

$|C_n/A_n|$ is given by 2.130 and 2.138.

2.7.4 Excitation

At the beginning of the channel ($z = 0$) the wave function in the slit should be equal to an arbitrary incoming wave function ψ_{in}.

$$|\psi_{in}\rangle_{z=0} = |\psi_{ch}\rangle_{z=0} = \sum_n u_n |\psi_n\rangle \tag{2.149}$$

Because the $|\psi_n\rangle$ are not orthogonal the u_n cannot be calculated directly. Instead, one has to switch to an orthogonal base $|\phi_n\rangle$. As described in the next section the $|\phi_n\rangle$ can be calculated as a linear combination of the $|\psi_n\rangle$.

$$|\phi_n\rangle = \sum_{m=0}^{N} d_{nm} |\psi_m\rangle \qquad \text{with } d_{nm} \text{ to be calculated (2.177)} \tag{2.150}$$

N is the number of levels taken into account. Now we can expand the incoming wave function in terms of $|\phi_n\rangle$. The amplitudes v_n can be calculated directly by projection.

$$|\psi_{in}\rangle_{z=0} = \sum_{n=0}^{N} v_n |\phi_n\rangle \qquad \text{with} \qquad v_n = \langle \phi_n | \psi_{in} \rangle_{z=0} \tag{2.151}$$

Combining (2.150) and (2.151) and we get:

$$|\psi_{in}\rangle_{z=0} = \sum_{n=0}^{N} \langle \phi_n | \psi_{in} \rangle_{z=0} |\phi_n\rangle = \sum_{n=0}^{N} \sum_{l=0}^{N} d_{nl}^* \langle \psi_l | \psi_{in} \rangle_{z=0} \sum_{m=0}^{N} d_{nm} |\psi_m\rangle \tag{2.152}$$

Comparing this result with (2.149) we get the amplitudes u_m.

$$u_m = \sum_{n=0}^{N} d_{nm} \sum_{l=0}^{N} d_{nl}^* \langle \psi_l | \psi_{in} \rangle_{z=0} \tag{2.153}$$

As shown in the next section the orthogonal base can be chosed so that $d_{nm} = 0$ for $n < m$. So we can re-write the sum boundaries:

$$u_m = \sum_{n=m}^{N} d_{nm} \sum_{l=0}^{n} d_{nl}^* \langle \psi_l | \psi_{in} \rangle_{z=0} \tag{2.154}$$

2.7.5 Orthogonalization

Let $|\psi_n\rangle$ be a set of normalized but not orthogonal functions. We denote the new orthogonal but not normalized functions with $|\chi_n\rangle$. The normalization results in $|\phi_n\rangle = |\chi_n\rangle / a_n$ with $a_n^2 = \langle \chi_n | \chi_n \rangle$. The algorithm follows the Gram Schmidt process but the explicit calculation of the $|\phi_n\rangle$ is skipped. All coefficients are expressed directly in terms of $|\psi_n\rangle$.

$$|\chi_0\rangle = |\psi_0\rangle \tag{2.155}$$
$$a_0^2 = \langle\chi_0|\chi_0\rangle = \langle\psi_0|\psi_0\rangle = 1 \tag{2.156}$$
$$|\phi_0\rangle = \frac{|\chi_0\rangle}{a_0} = \underbrace{1}_{d_{00}}|\psi_0\rangle \tag{2.157}$$
$$|\chi_1\rangle = c_{10}\,|\phi_0\rangle + |\psi_1\rangle \tag{2.158}$$
$$\langle\phi_0|\chi_1\rangle = c_{10}\langle\phi_0|\phi_0\rangle + \langle\phi_0|\psi_1\rangle = 0 \tag{2.159}$$
$$\Rightarrow \quad c_{10} = -\langle\phi_0|\psi_1\rangle = -\langle\psi_0|\psi_1\rangle \tag{2.160}$$
$$a_1^2 = \langle\chi_1|\chi_1\rangle = |c_{10}|^2\langle\phi_0|\phi_0\rangle + c_{10}^*\langle\phi_0|\psi_1\rangle + c_{10}\langle\psi_1|\phi_0\rangle + \langle\psi_1|\psi_1\rangle = 1 - |c_{10}|^2 \tag{2.161}$$
$$|\phi_1\rangle = \frac{|\chi_1\rangle}{a_1} = \underbrace{\frac{c_{10}}{a_1}}_{d_{10}}|\psi_0\rangle + \underbrace{\frac{1}{a_1}}_{d_{11}}|\psi_1\rangle \tag{2.162}$$
$$|\chi_2\rangle = c_{20}\,|\phi_0\rangle + c_{21}\,|\phi_1\rangle + |\psi_2\rangle \tag{2.163}$$
$$\langle\phi_0|\chi_2\rangle = c_{20}\langle\phi_0|\phi_0\rangle + c_{21}\langle\phi_0|\phi_1\rangle + \langle\phi_0|\psi_2\rangle = 0 \tag{2.164}$$
$$\Rightarrow \quad c_{20} = -\langle\phi_0|\psi_2\rangle = -\langle\psi_0|\psi_2\rangle \tag{2.165}$$
$$\langle\phi_1|\chi_2\rangle = c_{20}\langle\phi_1|\phi_0\rangle + c_{21}\langle\phi_1|\phi_1\rangle + \langle\phi_1|\psi_2\rangle = 0 \tag{2.166}$$
$$\Rightarrow \quad c_{21} = -\langle\phi_1|\psi_2\rangle = -d_{10}^*\langle\psi_0|\psi_2\rangle - d_{11}^*\langle\psi_1|\psi_2\rangle \tag{2.167}$$
$$a_2^2 = \langle\chi_2|\chi_2\rangle = ... = 1 - |c_{20}|^2 - |c_{21}|^2 \tag{2.168}$$
$$|\phi_2\rangle = \frac{|\chi_2\rangle}{a_2} = \underbrace{\frac{c_{20}d_{00} + c_{21}d_{10}}{a_2}}_{d_{20}}|\psi_0\rangle + \underbrace{\frac{c_{21}d_{11}}{a_2}}_{d_{21}}|\psi_1\rangle + \underbrace{\frac{1}{a_2}}_{d_{22}}|\psi_2\rangle \tag{2.169}$$
$$|\chi_3\rangle = c_{30}\,|\phi_0\rangle + c_{31}\,|\phi_1\rangle + c_{32}\,|\phi_2\rangle + |\psi_3\rangle \tag{2.170}$$
$$c_{30} = -\langle\phi_0|\psi_3\rangle = -d_{00}^*\langle\psi_0|\psi_3\rangle \tag{2.171}$$
$$c_{31} = -\langle\phi_1|\psi_3\rangle = -d_{10}^*\langle\psi_0|\psi_3\rangle - d_{11}^*\langle\psi_1|\psi_3\rangle \tag{2.172}$$
$$c_{32} = -\langle\phi_2|\psi_3\rangle = -d_{20}^*\langle\psi_0|\psi_3\rangle - d_{21}^*\langle\psi_1|\psi_3\rangle - d_{22}^*\langle\psi_2|\psi_3\rangle \tag{2.173}$$
$$a_3^2 = \langle\chi_3|\chi_3\rangle = 1 - |c_{30}|^2 - |c_{31}|^2 - |c_{32}|^2 \tag{2.174}$$
$$|\phi_3\rangle = \underbrace{\frac{c_{30}d_{00}+c_{31}d_{10}+c_{32}d_{20}}{a_3}}_{d_{30}}|\psi_0\rangle + \underbrace{\frac{c_{31}d_{11}+c_{32}d_{21}}{a_3}}_{d_{31}}|\psi_1\rangle + \underbrace{\frac{c_{32}d_{22}}{a_3}}_{d_{32}}|\psi_2\rangle + \underbrace{\frac{1}{a_3}}_{d_{33}}|\psi_3\rangle \tag{2.175}$$

The factors are calculated in the following order:

$$d_{00}{=}1 \quad c_{10}\;a_1 \quad d_{10}\;d_{11} \quad c_{20}\;c_{21}\;a_2 \quad d_{20}\;d_{21}\;d_{22} \quad c_{30}\;c_{31}\;c_{32}\;a_3 \quad d_{30}\;d_{31}\;d_{32}\;d_{33} \quad ... \tag{2.176}$$

with the formulas given here:

$$d_{nm} = \begin{cases} 0 & \text{if } m > n \\ 1/a_n & \text{if } m = n \\ \sum_{l=m}^{n-1} c_{nl}d_{lm}/a_n & \text{if } m < n \quad (0 \le m \le l < n) \end{cases} \tag{2.177}$$

$$c_{nl} = -\sum_{m=0}^{l} d_{lm}^*\langle\psi_m|\psi_n\rangle \quad (0 \le m \le l < n) \qquad\qquad a_n = \sqrt{1 - \sum_{l=0}^{n-1}|c_{nl}|^2} \tag{2.178}$$

The c_{nm} and a_n are needed for the subsequent row of d_{nm} only. The d_{nm} can be stored in a triangular matrix $d\,[n,m] = d\,[n(n+1)/2+m]$: $d_{00}\ d_{10}\ d_{11}\ d_{20}\ d_{21}\ d_{22}\ d_{30}\ d_{31}$ ...

2.7.6 Excitation by an Incoming Plane Wave

Now we have d_{nm} and need the projection $\langle\psi_l|\psi_{in}\rangle_{z=0}$ to calculate the amplitudes (2.154). We assume an incoming plane wave $\psi_{in}(x,z) = \exp(\mathrm{i}(k_{x,in}x + k_{z,in}z))$. To ease the notation we rename $k_{x,in}$ to h.

$$\langle\psi_n|\psi_{in}\rangle_{z=0} = \frac{1}{l}\int_{-l/2}^{l/2}\psi_n^*(x)\,\mathrm{e}^{\mathrm{i}hx}dx = \\ = \frac{1}{l}\Bigg(\underbrace{\int_{-\frac{a}{2}-d}^{-\frac{a}{2}}\psi_{\mathrm{IV}}^*(x)\,\mathrm{e}^{\mathrm{i}hx}dx}_{I_4} + \underbrace{\int_{-\frac{a}{2}}^{\frac{a}{2}}\psi_{\mathrm{I}}^*(x)\,\mathrm{e}^{\mathrm{i}hx}dx}_{I_1} + \underbrace{\int_{\frac{a}{2}}^{\frac{a}{2}+d}\psi_{\mathrm{II}}^*(x)\,\mathrm{e}^{\mathrm{i}hx}dx}_{I_2} + \underbrace{\int_{\frac{a}{2}+d}^{\frac{a}{2}+d+s}\psi_{\mathrm{III}}^*(x)\,\mathrm{e}^{\mathrm{i}hx}dx}_{I_3}\Bigg) \tag{2.179}$$

Where terms are different for the symmetric and the antisymmetric case we write the former on top of the latter.

$$I_1 = \quad A^*\int_{-\frac{a}{2}}^{\frac{a}{2}}\begin{matrix}\sin\\ \cos\end{matrix}(k^*x)\,\mathrm{e}^{\mathrm{i}hx}dx = \frac{2A^*}{h^2-k^{*2}}\left(\begin{matrix}\mathrm{i}k^*\\ h\end{matrix}\cos\tfrac{k^*a}{2}\sin\tfrac{ha}{2} - \begin{matrix}\mathrm{i}h\\ k^*\end{matrix}\sin\tfrac{k^*a}{2}\cos\tfrac{ha}{2}\right) \tag{2.180}$$

$$I_3 = \mathrm{e}^{\mathrm{i}h\frac{l}{2}}C^*\int_{-\frac{s}{2}}^{\frac{s}{2}}\begin{matrix}\sin\\ \cos\end{matrix}(K^*x)\,\mathrm{e}^{\mathrm{i}hx}dx = \frac{2C^*\,\mathrm{e}^{\mathrm{i}h\frac{l}{2}}}{h^2-K^{*2}}\left(\begin{matrix}\mathrm{i}K^*\\ h\end{matrix}\cos\tfrac{K^*s}{2}\sin\tfrac{hs}{2} - \begin{matrix}\mathrm{i}h\\ K^*\end{matrix}\sin\tfrac{K^*s}{2}\cos\tfrac{hs}{2}\right) \tag{2.181}$$

$$I_4 = \int_{\frac{a}{2}+d}^{\frac{a}{2}}\psi_{\mathrm{IV}}^*(-x)\,\mathrm{e}^{-\mathrm{i}hx}(-dx) = \int_{\frac{a}{2}}^{\frac{a}{2}+d}\psi_{\mathrm{IV}}^*(-x)\,\mathrm{e}^{-\mathrm{i}hx}dx = \int_{\frac{a}{2}}^{\frac{a}{2}+d}(\pm\psi_{\mathrm{II}}^*(x))\,\mathrm{e}^{-\mathrm{i}hx}dx \tag{2.182}$$

$$I_2 + I_4 = \int_{\frac{a}{2}}^{\frac{a}{2}+d}\psi_{\mathrm{II}}^*(x)(\,\mathrm{e}^{\mathrm{i}hx} \pm \mathrm{e}^{-\mathrm{i}hx})\,dx = 2\int_{\frac{a}{2}}^{\frac{a}{2}+d}\psi_{\mathrm{II}}^*(x)\begin{matrix}\mathrm{i}\sin\\ \cos\end{matrix}(hx)\,dx = \tag{2.183}$$

$$= 2\int_0^d A^*\left[\begin{matrix}\sin\\ \cos\end{matrix}\tfrac{k^*a}{2}\cos(\kappa^*x) \mp \tfrac{k^*}{\kappa^*}\begin{matrix}\cos\\ \sin\end{matrix}\tfrac{k^*a}{2}\sin(\kappa^*x)\right]\begin{matrix}\mathrm{i}\sin\\ \cos\end{matrix}\left(h(x+\tfrac{a}{2})\right)dx = \tag{2.184}$$

$$= 2\int_{-d}^0 C^*\left[\begin{matrix}-\sin\\ +\cos\end{matrix}\tfrac{K^*s}{2}\cos(\kappa^*x) + \tfrac{K^*}{\kappa^*}\begin{matrix}\cos\\ \sin\end{matrix}\tfrac{K^*s}{2}\sin(\kappa^*x)\right]\begin{matrix}\mathrm{i}\sin\\ \cos\end{matrix}\left(h(x+\tfrac{a}{2}+d)\right)dx = \tag{2.185}$$

$$= \ldots = \text{with (2.130) and (2.138)} = \tag{2.186}$$

$$= \frac{2A^*}{h^2-\kappa^{*2}}\left(\begin{matrix}\mathrm{i}h\\ k^*\end{matrix}\sin\tfrac{k^*a}{2}\cos\tfrac{ha}{2} - \begin{matrix}\mathrm{i}k^*\\ h\end{matrix}\cos\tfrac{k^*a}{2}\sin\tfrac{ha}{2}\right) + \tag{2.187}$$

$$+ \frac{2C^*}{h^2-\kappa^{*2}}\left(\begin{matrix}\mathrm{i}h\\ K^*\end{matrix}\sin\tfrac{K^*s}{2}\cos\tfrac{h(a+2d)}{2} + \begin{matrix}\mathrm{i}K^*\\ h\end{matrix}\cos\tfrac{K^*s}{2}\sin\tfrac{h(a+2d)}{2}\right)$$

$$\langle\psi_n|\psi_{in}\rangle_{sym} = \frac{2}{l}\Big[A^*\left(\tfrac{1}{k^{*2}-h^2} - \tfrac{1}{\kappa^{*2}-h^2}\right)\left(-h\cos\tfrac{k^*a}{2}\sin\tfrac{ha}{2} + k^*\sin\tfrac{k^*a}{2}\cos\tfrac{ha}{2}\right) \\ + C^*\,\mathrm{e}^{\mathrm{i}h\frac{l}{2}}\tfrac{1}{K^{*2}-h^2}\left(-h\cos\tfrac{K^*s}{2}\sin\tfrac{hs}{2} + K^*\sin\tfrac{K^*s}{2}\cos\tfrac{hs}{2}\right) \\ - C^*\tfrac{1}{\kappa^{*2}-h^2}\left(h\cos\tfrac{K^*s}{2}\sin\tfrac{h(l-s)}{2} + K^*\sin\tfrac{K^*s}{2}\cos\tfrac{h(l-s)}{2}\right)\Big] \tag{2.188}$$

$$\begin{aligned}\langle\psi_n|\psi_{in}\rangle_{asy} = \frac{2\mathrm{i}}{l}\Big[&A^*\left(\tfrac{1}{k^{*2}-h^2}-\tfrac{1}{\kappa^{*2}-h^2}\right)\left(h\sin\tfrac{k^*a}{2}\cos\tfrac{ha}{2}-k^*\cos\tfrac{k^*a}{2}\sin\tfrac{ha}{2}\right)\\&+C^*\,\mathrm{e}^{\mathrm{i}h\frac{l}{2}}\tfrac{1}{K^{*2}-h^2}\left(h\sin\tfrac{K^*s}{2}\cos\tfrac{hs}{2}-K^*\cos\tfrac{K^*s}{2}\sin\tfrac{hs}{2}\right)\\&-C^*\,\tfrac{1}{\kappa^{*2}-h^2}\left(h\sin\tfrac{K^*s}{2}\cos\tfrac{h(l-s)}{2}+K^*\cos\tfrac{K^*s}{2}\sin\tfrac{h(l-s)}{2}\right)\Big]\end{aligned} \tag{2.189}$$

Now we can calculate the complete wave function. An example is given in figure 2.23.

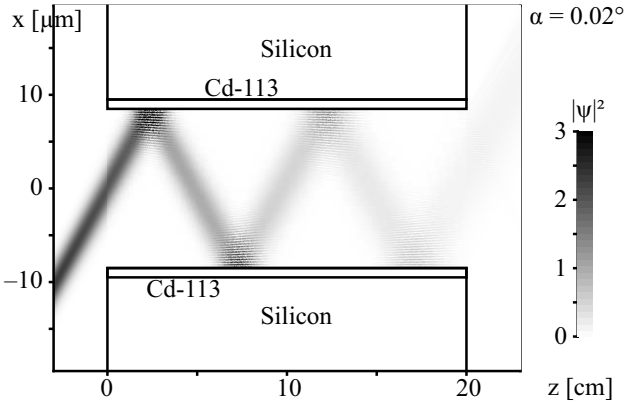

Figure 2.23: A beam in an absorber coated channel. At each reflection the beam is slighly attenuated but mostly reflected. The beam does not penetrate into the material because we are still in the regime of total reflection. In this picture the channel has an arbitrary length in order to demonstrate the absorption.

2.7.7 Phase Shift

The phase shift is calculated in a similar way as in section 2.1.2.

$$\psi_{out} = \langle\psi_{in}|\psi_{ch}\rangle_{z=L}\;\psi_{in} =: S\cdot\psi_{in} \tag{2.190}$$

$$|\psi_{in}\rangle = \exp(\mathrm{i}(k_{x,in}x+k_{z,in}z)) \tag{2.191}$$

$$|\psi_{ch}\rangle = \sum_n|\psi_n\rangle = \sum_n u_n\psi_{x,n}(x)\,\mathrm{e}^{\mathrm{i}k_{z,n}z}\,\mathrm{e}^{E''_n mz/(\hbar^2k_{z,n})} \qquad (2.109) \tag{2.192}$$

$$u_n = \sum_{m=n}^{N} d_{mn}\sum_{l=0}^{m} d^*_{ml}\;\langle\psi_l|\psi_{in}\rangle_{z=0} \qquad (2.154) \tag{2.193}$$

$$\begin{aligned}S = \langle\psi_{in}|\psi_{ch}\rangle_{z=L} &= \frac{1}{l}\int_{-l/2}^{l/2}dx\;\mathrm{e}^{-\mathrm{i}(k_{z,in}L+k_{x,in}x)}\;\sum_n u_n\psi_n(x)\,\mathrm{e}^{\mathrm{i}k_{z,n}L}\,\mathrm{e}^{E''_n mL/(\hbar^2k_{z,n})} =\\&=\sum_n\;u_n\;\mathrm{e}^{\mathrm{i}(k_{z,n}-k_{z,in})L}\;\mathrm{e}^{E''_{x,n}mL/(\hbar^2k_{z,n})}\;\langle\psi_{in}|\psi_n\rangle_{z=0}\end{aligned} \tag{2.194}$$

The expression $\langle\psi_l|\psi_{in}\rangle_{z=0}$ which is used in (2.193) and (2.194) is given in (2.188f). The result of S is plotted in figure 2.24. The double reflected part ($|\alpha| > 0.05$) is more or less absorbed, but the straight part in the center is hardly affected. So we can conclude that an absorber coating would not substantially change the phase shift of the channel.

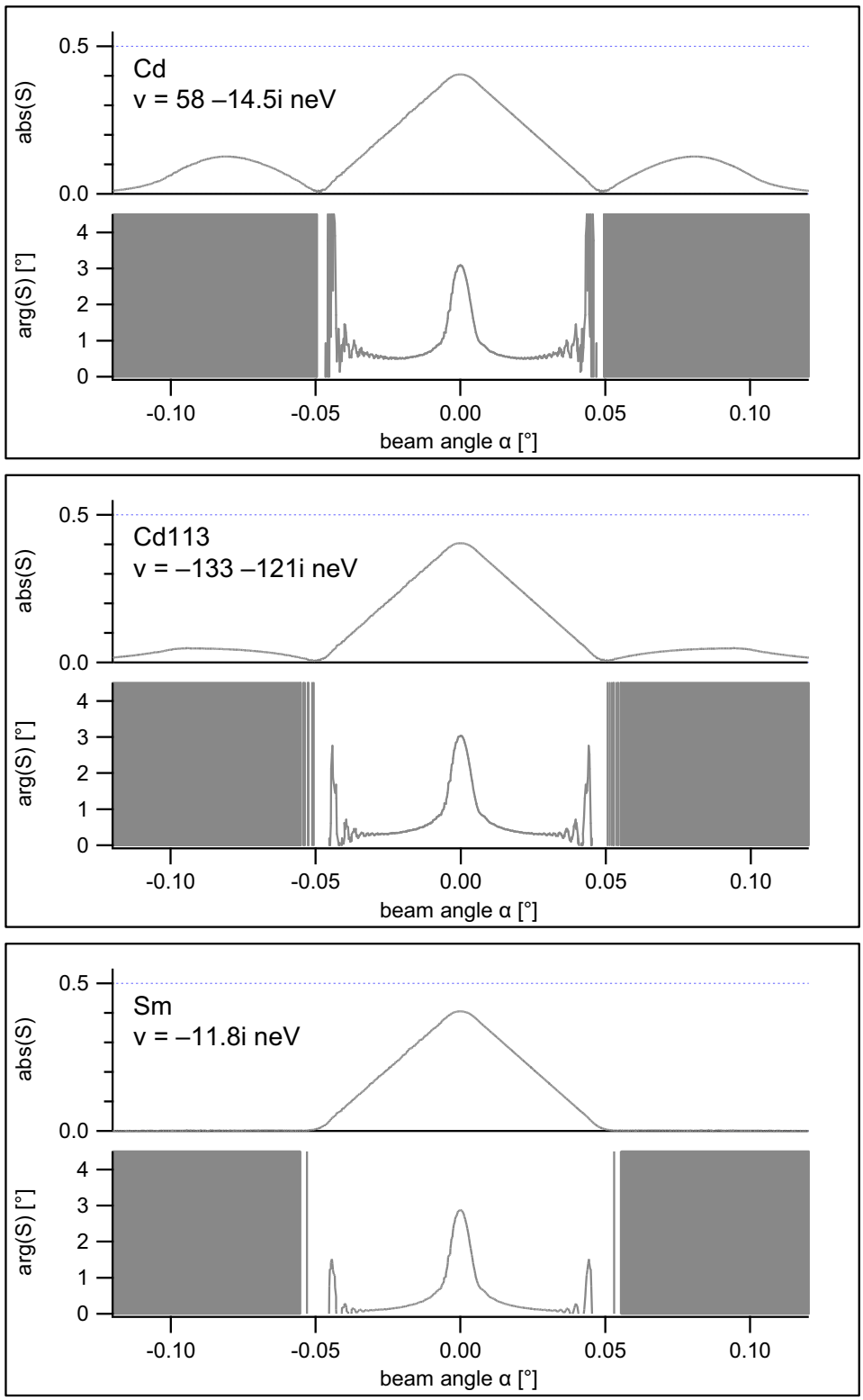

Figure 2.24: Transmission amplitude abs(S) and phase shift arg(S) for different absorber coatings. The comparable calculation without absorber is given in figure 2.8. The double reflected part (figure 2.8 D) is more or less absorbed, but the central part is hardly affected.

2.8 Refraction by the Channel Walls

By calculating the wave function of the neutrons we can describe all wave effects like diffraction (section 2.3) as well as effects of geometric optics like reflection and refraction (e.g. figure 2.18). Unfortunatly it would be very difficult to calculate the wave function for non ideal geometries, like slighly non parallel channel walls. Now we want to try the semiclassical approach of ray optics, which is good enough for reflection and refraction, and can easily by applied on geometrical imperfections.

Figure 2.25 shows the basic processes a classical beam may undergo when passing the channel stack. Depending on the entrance position and angle the beam can be refracted (red and dark blue) or reflected (light blue) or transmitted (green). Each process leads to a very distinct angle deviation $\delta\alpha$ which is given in the figure for perfect geometry.

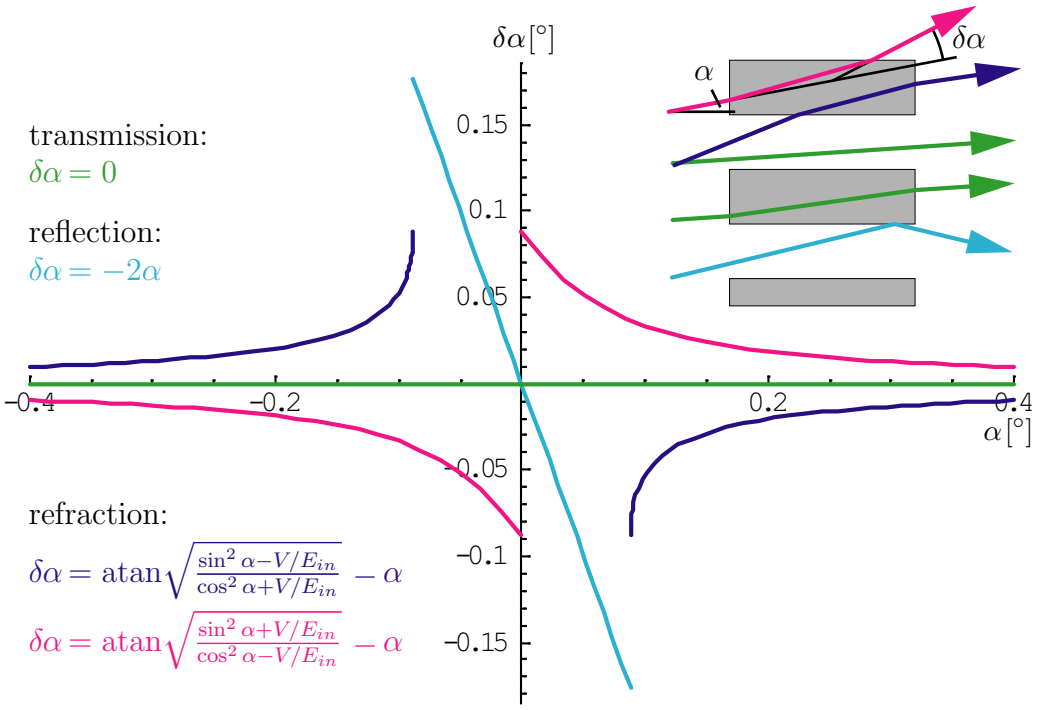

Figure 2.25: Exit angles which are possible by reflection and refraction. Perfect geometry is assumed.

Non perfect geometries can be investigated by a Monte Carlo simulation. First a virtual stack of 250 channels is created by randomly varying the geometric parameters of the wall plates. See table 2.3. Then a few thousand beams are sent through the channel stack at random entry positions and incident angles. The exit angle of each beam is calculated and counted in a histogram. Figure 2.26 shows the result for nearly perfect geometries. The distinct angle deviations of the ideal case (figure 2.25) are still valid. Figure 2.27a) shows the result for realistic geometries with the standard deviations given in table 2.3. Now the distinct angles have become broad distributions. Figure 2.27b) shows experimental data acquired with the real channel stack. The agreement is very good. The measurement has been performed in 2003 at the S18 instrument at the ILL, using the USANS setup (Ultra Small Angle Neutron Scattering).

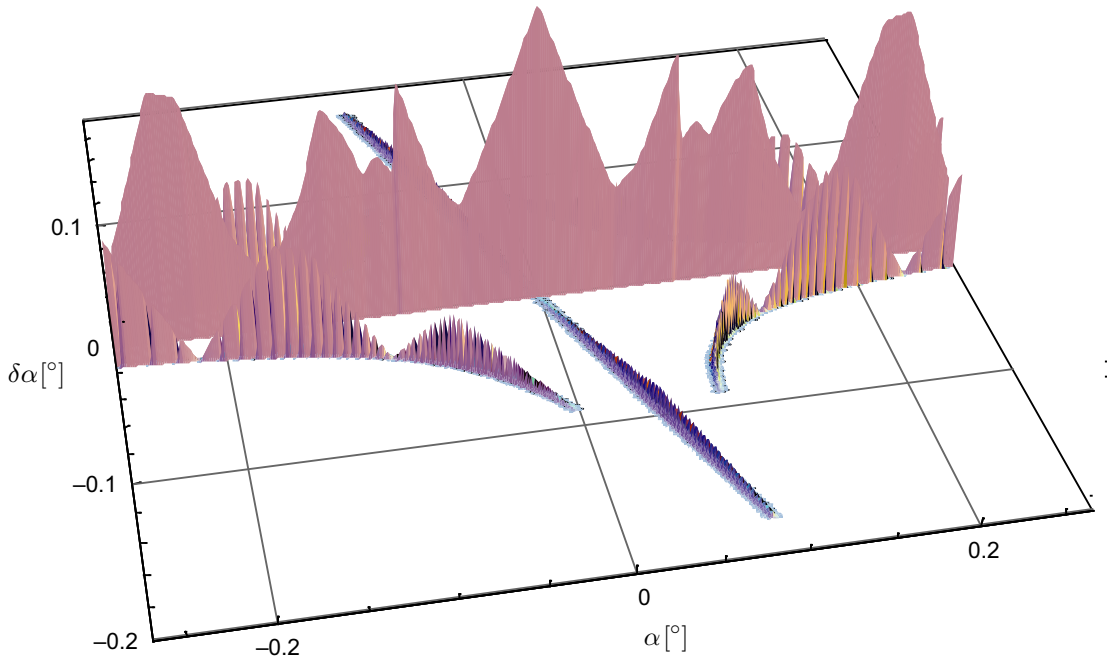

Figure 2.26: Probability for the exit angles, calculated by a Monte Carlo simulation of a channel stack with slightly imperfect geometry.

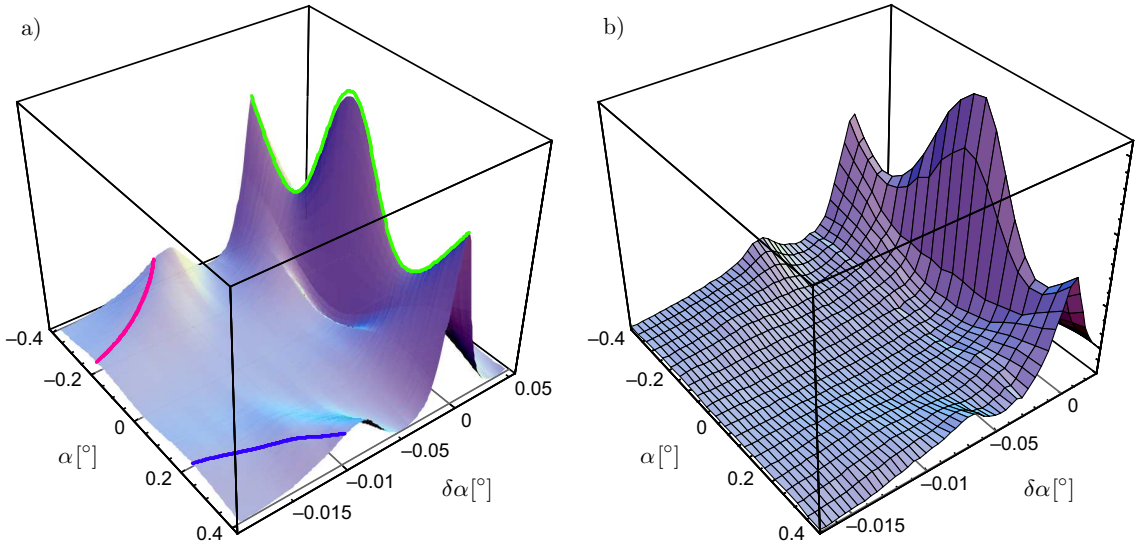

Figure 2.27: a) Monta Carlo simulation of a channel stack with realistic geometry. b) Measurement of the real channel stack with Ultra Small Angle Neutron Scattering (USANS).

parameter	mean value	standard deviation
plate length L	20mm	0.015mm
plate thickness s	17μm	5μm
plate distance = channel width a	22μm	5μm
parallelity of neighbouring plates	0°	0.02°
parallelity of plate surfaces (channel walls)	0°	0.02°
tilt of plate faces (versus beam direction)	0°	50°
beam incident angle	0°	0.1°

Table 2.3: Parameters of the Monte Carlo simulation.

The intensity distribution at $\delta\alpha = 0$ gives the non scattered intensity, marked by the green line in figure 2.27a). This distribution is important, because it is also obtained by a neutron interferometer with one beam blocked, see figure 4.5. Therefore it can be used for the angle alignment of the channel stack in the interferometer. In addition, it gives knowledge about the beam divergence of the experimental setup. The central peak represents the angle distribution of the incident beam convoluted with the triangular peak of the channel transmission, see (A) in figure 2.8. The FWHM of the latter is 0.05°. Subtracting this value from the measured peak width gives roughly the beam divergence, which is in the range of 0.2° to 0.5°, see the experimental results in figure 4.15.

2.9 Talbot Pattern

The Talbot effect [BMS01] was discoverd in 1836 by Henry Fox Talbot. He shone parallel light through a regular grid of slits and discoverd that the shadow behind the slits first became diffuse with increasing distance but then at a certain distance z_T became sharp again, shifted by half the grid period. The so-called Talbot distance z_T was calculated by Rayleigh to be $z_T = l^2/\lambda$ with the wave length λ and the grid periode l.

With our calculations of the wave function within and behind a channel we can easily reproduce this effect by using a short channel and looking at a distance far behind it. For λ=1.9Å, slit width $a = 17\mu$m and wall width $s = 22\mu$m we get a potential periode of $l = 39\mu$m and a Talbot distance of $z_T = 800$cm. At this distance the intensity distribution has the same rectangular shape as at $z = 0$, shifted by $l/2$. See figure 2.28a). We can also see the fractional Talbot effect which means that at distances of fractions of z_T like $z_T/2$ or $z_T/3$ the intensity distribution is a superposition of several narrowed copies of the original rectangular shape. In this calculation, only the bound states have been taken into account because for the Talbot effect the walls should be opaque.

A related effect can be observed if we take a very long channel and look again at the bound states. The channel walls are like mirrors and the system in between is equivalent to a periodic system with the periode equal to the mirror distance a. For $a = 17\mu$m we get a Talbot distance of $z_T = 152$cm where the original intensity distribution of the channel entrance is restored, see figure 2.28a). This is a form of quantum revival, as described in detail by Robinett [Rob04].

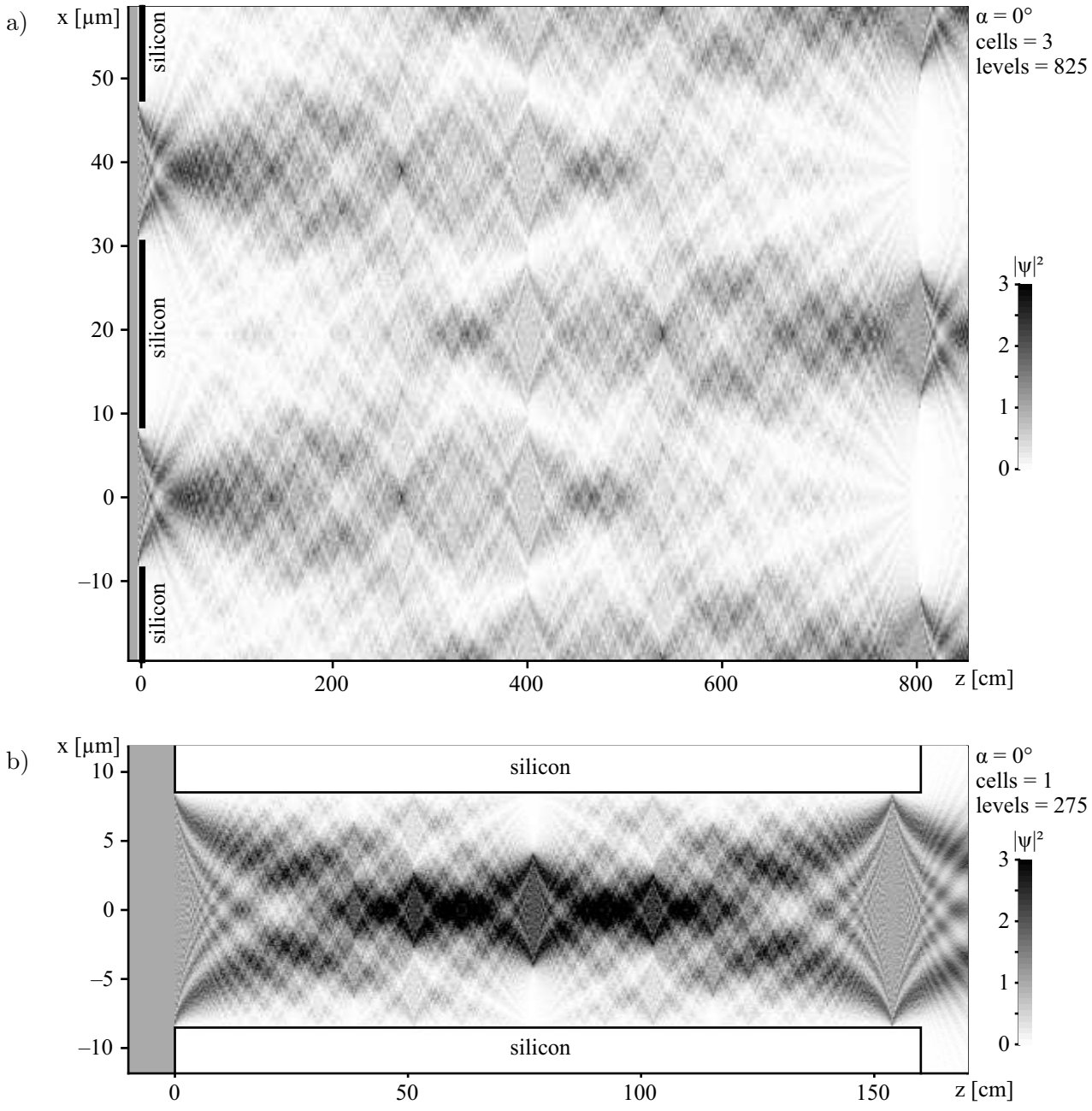

Figure 2.28: a) The original Talbot effect. A plane wave is falling from the left onto a regular grid of opaque and transparent regions with the periode l. The wave is diffracted at the edges but at the Talbot distance $z_T = l^2/\lambda$ behind the grating the original intensity pattern is restored, shifted by $l/2$.
b) A similar effect between two mirrors. In this case the mirror distance a determines the Talbot distance, $z_T = a^2/\lambda$.

Chapter 3

Channel Preparation

3.1 Geometry

The beam cross section in neutron interferometry is in the order of 1cm. A single channel of 20 μm width could use only a tiny fraction of the intensity. Because intensity is a crucial factor in neutron interferometry we should try to pack as many channels as possible into the beam cross section. This can be achieved by a channel stack made of alternating layers of wall plates and spacers, see figure 3.1.

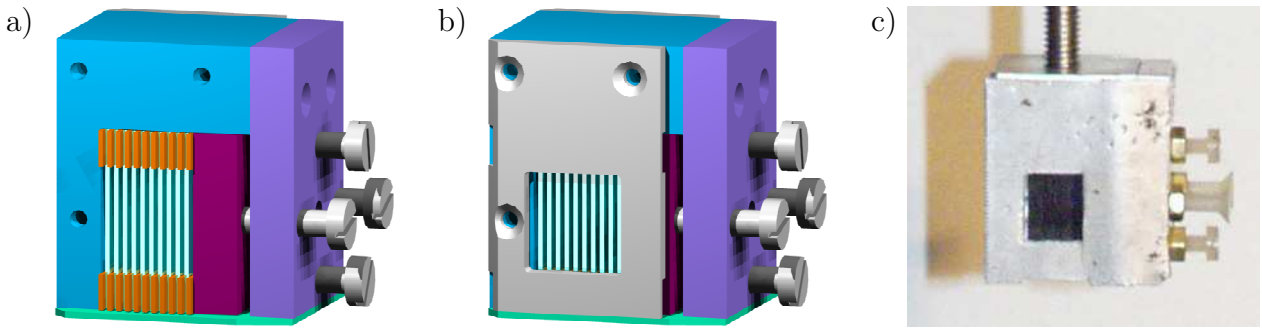

Figure 3.1: The structure of the channel system. The channels are made of alternating layers of thin silicon plates and spacers. The stack is encapsulated in a framework of aluminum parts, shown in blue and green (a). The red plate is pressed by the four screws onto the stack to hold it together. The spacers, shown in orange, stick out of the stack and are hold in place by the grooves in the front and back plates, shown in light gray in (b). The thickness of the layers is scaled up in this picture. Figure (c) shows the real sample. Front and back side are covered with a cadmium sheet so that the neutrons cannot penetrate the aluminum case. The size of the opening in the cadmium is 9×10 mm.

Two samples with the channel length 1cm and 2cm have been built. The framework around the channel stack must be small enough to fit into the neutron interferometers. Figure 3.2 shows the dimensions of the interferometers used in the experiments. In principle there are four different sample positions, labelled with Ia, Ib, IIa, IIb. The roman number indicates the beam path. As a matter of convention, number I denotes the beam which is transmitted by the first blade. The mirror blade divides each beam path into section a and section b. The space in

each position is limited by the interferometer blades and by the overlap region of beam path I and II.

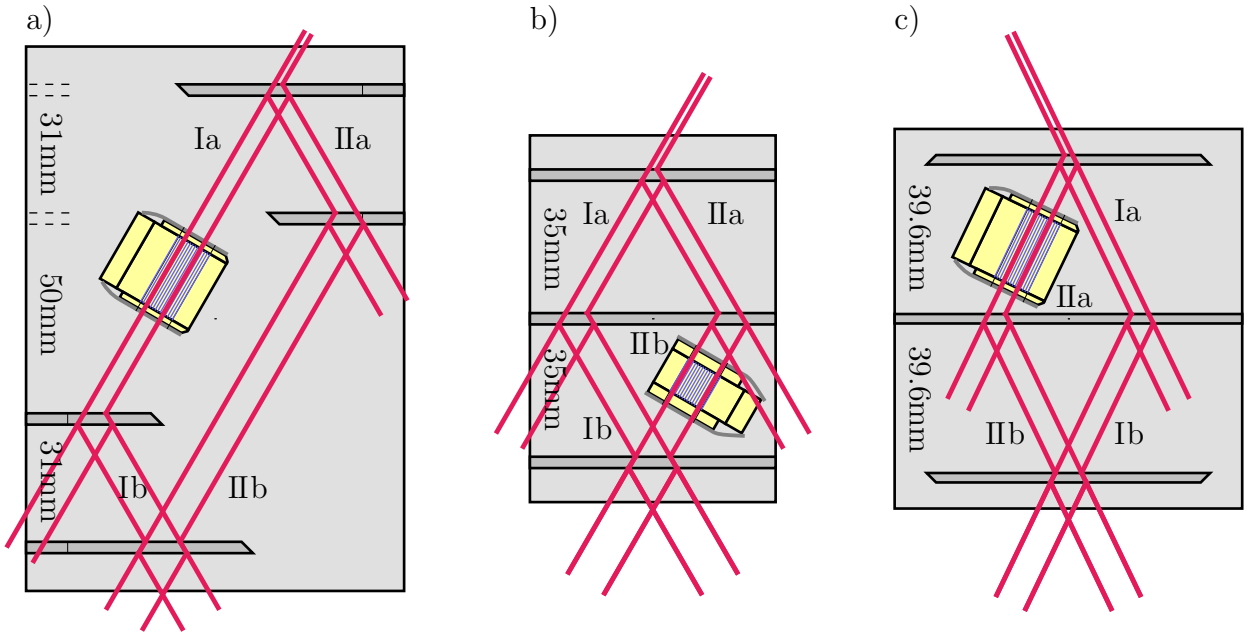

Figure 3.2: The interferometers used in the experiments. a) and b) are use at the ILL. The Bragg planes are oriented in $\langle 220 \rangle$-direction resulting in $\lambda = 1.92$Å at $\theta_B = 30°$. c) is used at NIST and uses $\langle 111 \rangle$ Bragg planes resulting in $\lambda = 2.71$Å at $\theta_B = 26.5°$.

Usually it makes no difference for the phase measurement where the sample is located (up to a sign change between path I and II). Surprisingly it did make a difference in our experiment, as we can see in the measurements (chapter 4) and calculations (chapter 6).

3.2 Selection of Materials

The wall plates separating the channels should be rather thin in order to get many channels into the beam cross section, but they must be stiff enough to create a well defined geometry. For these reasons silicon wafers are very well suited. They are available down to a thickness of 15 to 20μm. This would allow 250 channels in a stack of 1cm total thickness.

The spacers between the walls could be of any material as long as the thickness is well defined. In the end, silicon wafers turned out to be the best choice as well. I also tried stainless steel foils and audio tape.

The steel foils couldn't be cut without producing wrinkles at the edges. Therefore the whole stack had to be compressed to flatten the steel foils. When releasing the pressure the stack expanded like a spring. The problem was that the pressure and the uneven foils transferred stress onto the wall plates causing the plates to bend, and many plates even touched each other in the middle of the channel. This wouldn't work.

The audio tape was very promising. The tape had no wrinkles and the thickness was very constant. Different thicknesses were available, about 10 to 20μm, depending on the playing

time. I assembled the stack and made an interferometry measurement. I got no intensity at all. The problem was that the tape had an imprinted curvature. A tiny piece of tape didn't lie flat on a table but curled up a little bit. I had used all spacers in the same orientation in order to build a very regular stack. Appearently the curvature had been transferred very regularly onto the wall plates, forming a kind of bent neutron guide. This was not apparent by looking through the channels because the reflecting silicon plates formed also a good optical fiber. However, in neutron interferometry it is curcial that the sample does not change the direction of the neutrons.

3.3 Cutting Silicon Wafers

The wall pates and the spacer plates have been cut out of silicon wafers as shown in figure 3.3.

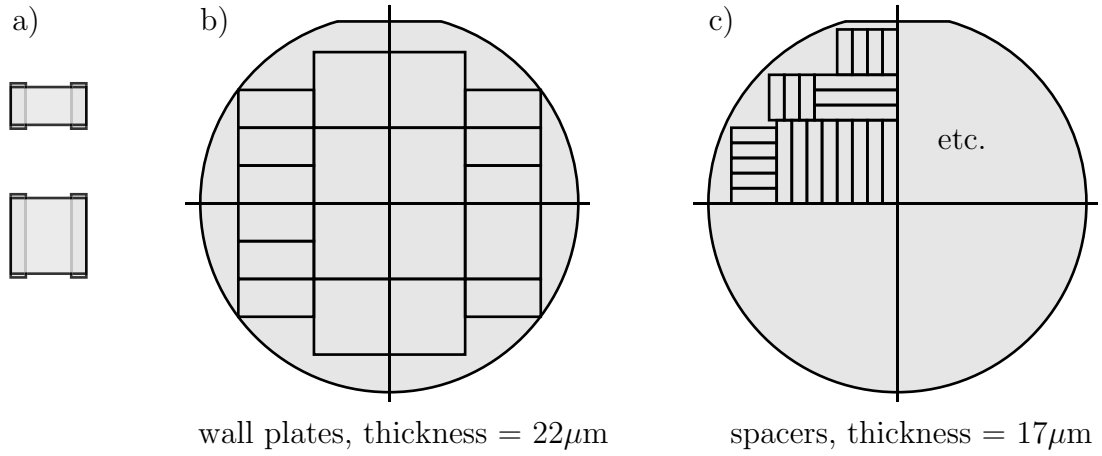

Figure 3.3: The channels are made of alternating layers of wall plates and spacers. Two different channel stacks with the lengths of 1 and 2 cm are built (a). The plates are cut out of silicon wafers of four inch diameter. A thicker wafer is used for the wall plates for better mechanical stability (b). A thinner wafer is used for the spacers (c) because narrower channels increase the phase shift.

Wafers with a thickness in the order of 20μm are bendable like a stiff sheet of paper but they are still very brittle. They break preferably along the cristal planes and can be cut by scratching and bending. It is not necessary to scratch along the whole cutting line. A little scratch at the edge is enough to initiate the crack.

For creating the two channel stacks a few thousand cuts were necessary. I built a cutting device to facilitate the process, see figure 3.4. The device has a little table where the wafers are placed on. A diamond needle mounted on a slider is moved manually over the wafer edge. The slider is guided so that the scratching point on the table is well defined. Different distance plates can be laid onto the table in order to form a limit stop for the wafer. Thus the width of the cutted piece can be controlled. After scratching, one part of the table is lowered, leaving an edge where the wafer is bent over until it cracks.

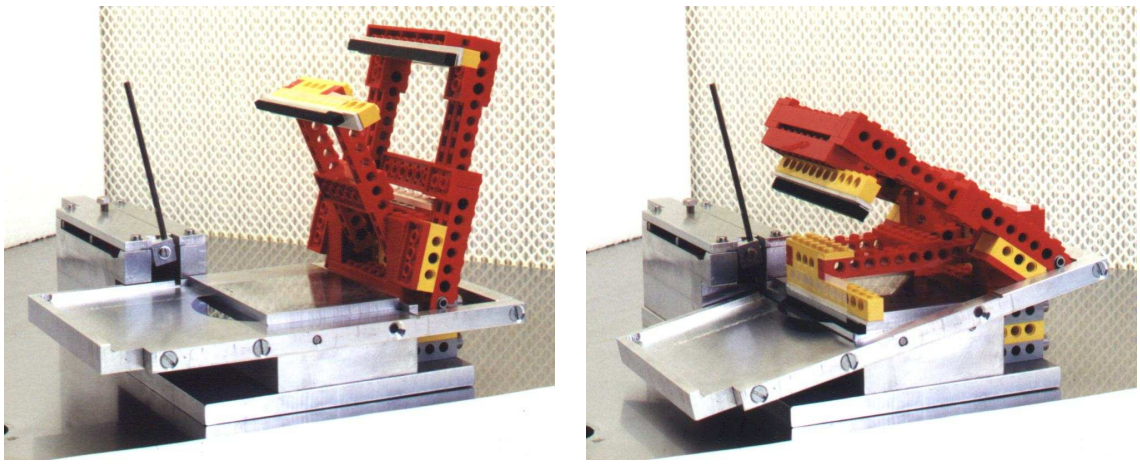

Figure 3.4: A cutting device for thin silicon wafers. It works a little bit like a tile cutter.

3.4 Wafer Thickness

The wafers were available in 12μm and 20μ thickness with a variance of $\pm$2.5μm. Unfortunately it turned out that the thickness does not only vary between different wafers but also within a few centimeters distance on a single wafer. In order to make fast and contact-free measurements of the wafer thickness I built a device which measured the transmission of laser light through the wafers, shown in figure 3.5 and figure 3.6. The transmitted intensity could be translated into the wafer thickness by a calibration curve which was acquired by a few wafer pieces measured with a mechanical micrometer.

a) b)

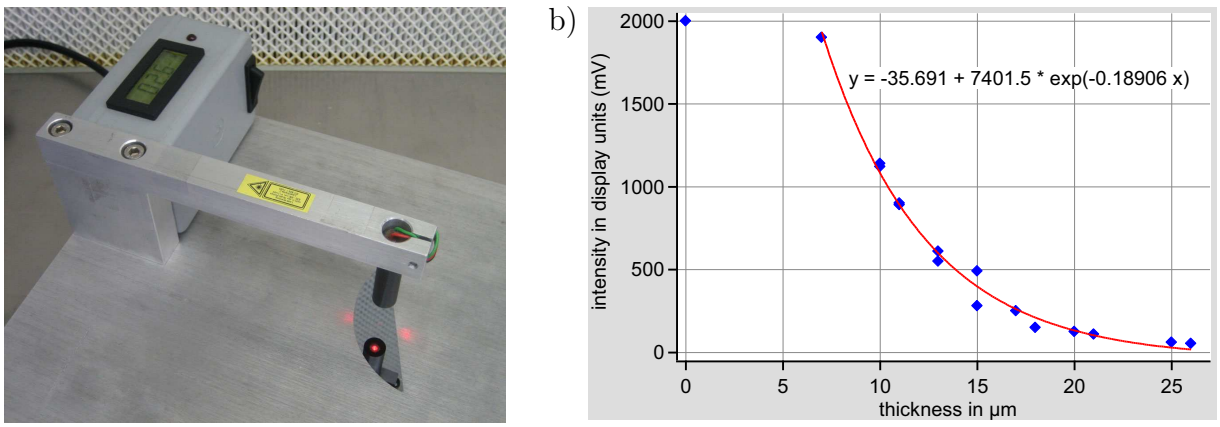

Figure 3.5: a) A light barrier device for measuring the wafer thickness by means of laser transmission. b) A calibration curve translates the measured intensity into the wafer thickness.

In order to avoid stress on the channel walls and to make them as parallel as possible I grouped the spacer plates into pairs of similar thickness and used each pair for a single layer. When the spacers were thinner at one end than at the other I tried to compensate that in the next layer by using similar spacers the other way round.

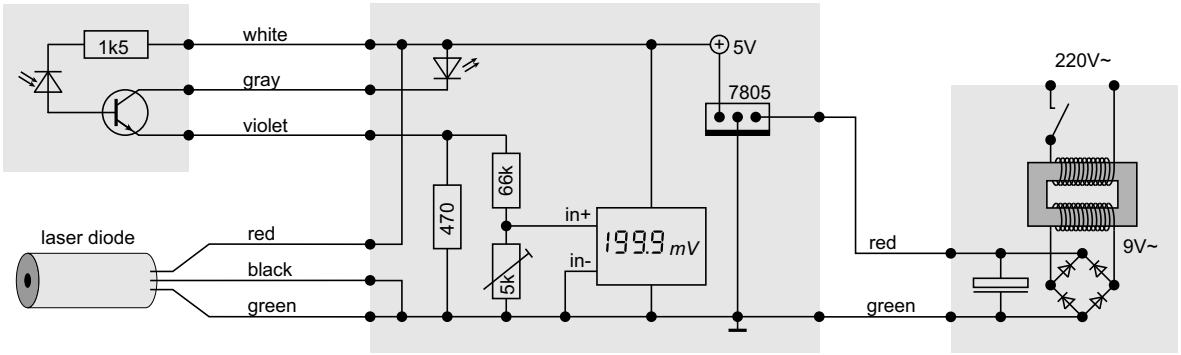

Figure 3.6: The electronic circuit for the light barrier device.

3.5 Photogrammetric Survey

In the end I wanted to measure the real distances of the channel layers. I looked at the stack profile under a microscope and shot a series of pictures covering the whole profile. In addition I took a picture of a micrometer scale in order to make distance measurements on the pictures, see figure 3.7.

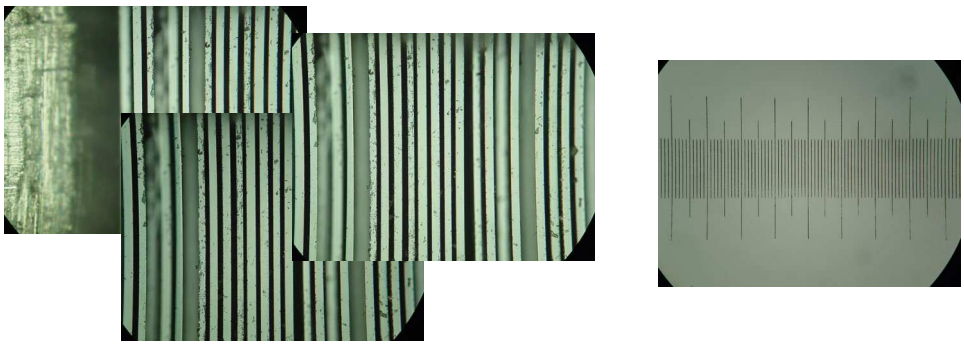

Figure 3.7: A series of overlapping microscope pictures (26 in total) covering the whole profile of the channel stack. The white stripes are the faces of the silicon plate, reflecting the light, and the black stripes are the channels. Some white stripes are very diffuse. These are silicon plates which are out of the focus depth. A picture from a micrometer scale serves as reference for distance measurements.

The distortion due to the microscope and camera optics was apparent. Therefore it was not possible to chain the pictures directly together. Instead I compared each picture with the micrometer scale, which had been taken with the same optical settings and contained the same distortions. In this way I got a series of layer thickness values for each picture. In a second step I identified the layers of one picture with the overlapping layers from the next picture and got a complete histogram of all layers.

I wrote a small computer program to automate the process by means of pattern recognition. The pictures are cut perpendicular to the layers so that only the central profile with a width of 100 pixels $\approx 40\mu$m is left, see figure 3.8 a). Within each pixel column the grayshades are averaged in order to get a brightness function which doesn't fluctuate with the dust particles, figure 3.8 b). This function and its derivative are evaluated to determine the positions of the silicon edges as a function of the pixel column. In a similar way the picture of the micrometer scale is evaluated to get a transformation function from pixel position into μm values. Now

we have local μm coordinates within each picture and have to determine the offset between the pictures. The irregularity of the wafer thickness makes it possible that even this offset can be found automatically, similar to the comparison of tree rings in dendrochronology. We only have to try all possible layer assignments between consecutive pictures and see which fits best. The result is displayed on the screen and can be checked manually, see figure 3.9. When the local scales are fixed to each other, the local coordinates can be transformed into global ones. Coordinates from different pictures but identical edges can be averaged. Finally a width histogram of all channels and walls is calculated. Figure 3.10 shows the histograms of the two channel stacks.

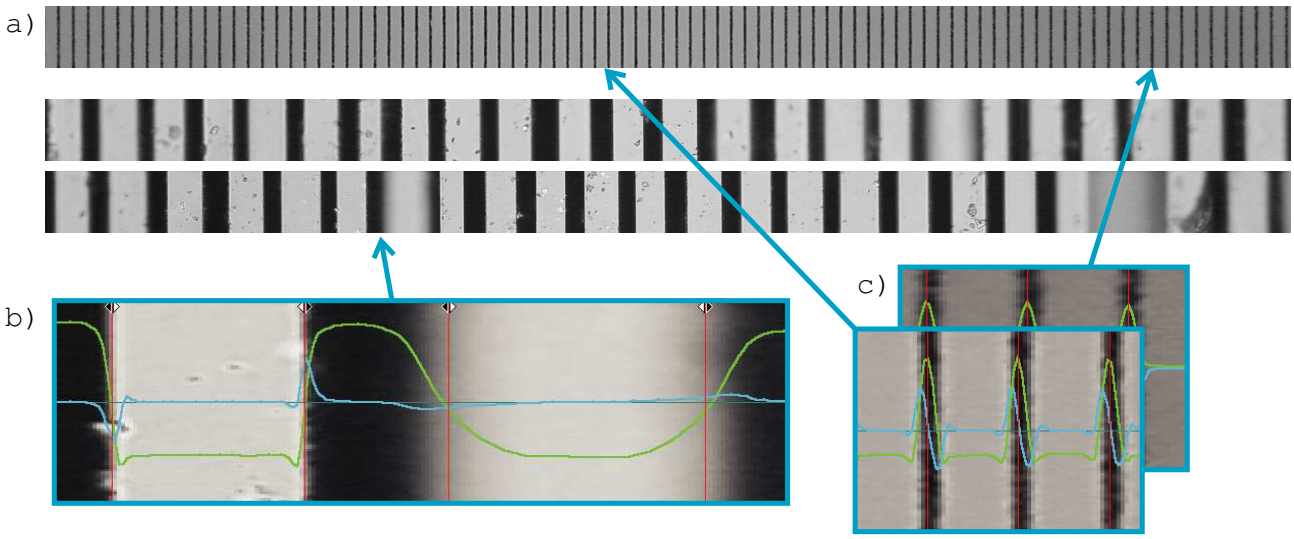

Figure 3.8: a) The micrometer scale with a line distance of 10μm, and the profiles of the channel stack. b) The position of the edges is found automatically by evaluating the brightness curve (green) and its derivative (blue). The optical distortions are illustrated in c). The width in pixels between two scale lines is different in the center and at the border of the picture.

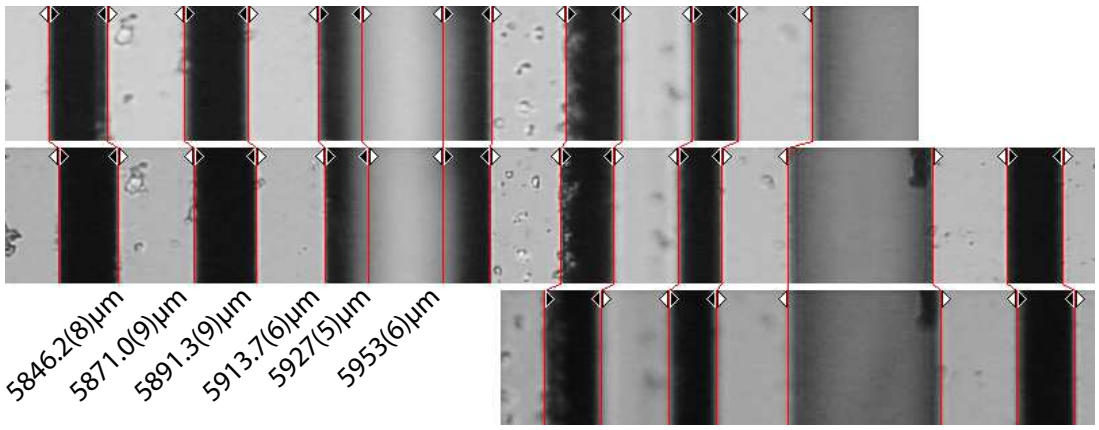

Figure 3.9: The edges (red lines) found in one picture are correlated with the edges in the next picture. This way a global coordinate of each edge is calculated. The correlation is done using the local μm coordinates within each picture. If the silicon plate is totally out of focus then it is skipped and the width is not counted.

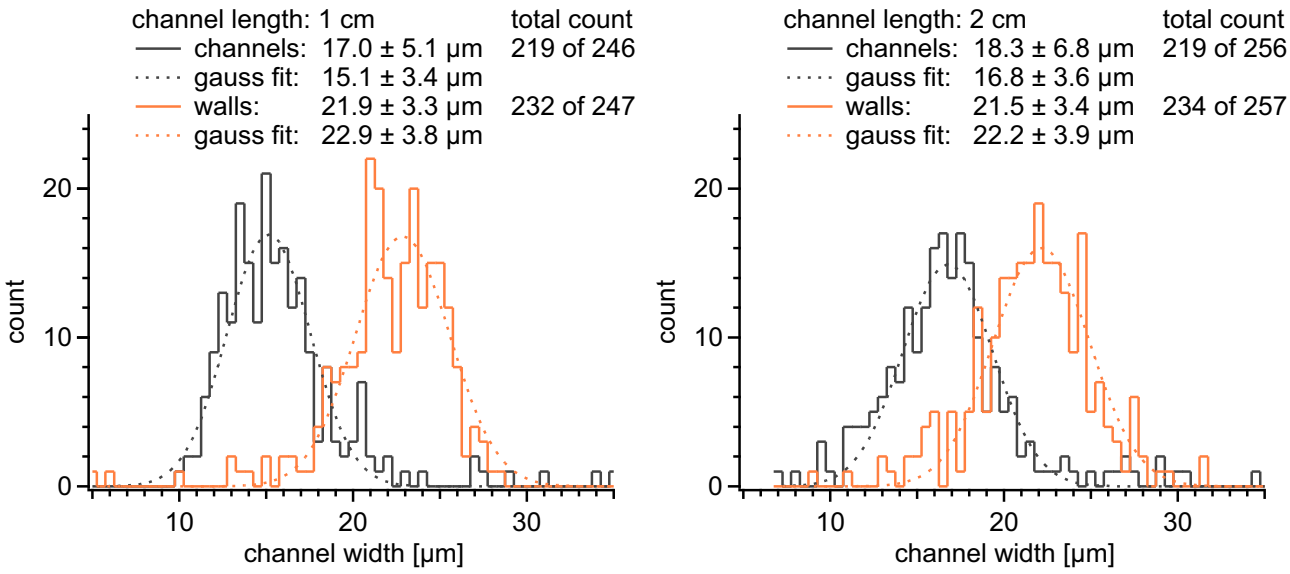

Figure 3.10: The statistics over the channel widths and wall widths for both channel stacks. Two mean values are given, one calculated directly from the data and one derived from the Gaussian fit. The ± values denote one sigma.

3.6 Sandblasting

The silicon plates of the walls are not opaque for neutrons. Neutrons which are inside the channels are totally reflected because of the glancing angle. But neutrons which hit the face of the plates between two channels can easily penetrate. These neutrons undergo a phase shift according to the silicon index of refraction and we have to ensure that these neutrons do not disturb our measurement of the channel phase.

A silicon block of the thickness L causes a phase shift $\varphi = (k_{\text{silicon}} - k_{\text{air}}) \cdot L$. If we put in numbers we get for $L = 2\text{cm}$ a phase shift of roughly $125 \cdot 2\pi$. For calculating the variance $\delta\varphi$ we need the variance of k. The wave length distribution is determined by the beam divergence because in neutron interferometry the wave length and the beam direction are correlated by Bragg's law. The usual divergence of $\delta\theta \approx 0.5°$ results in $\delta k/k \approx 1.5\%$, resulting further in $\delta\varphi \approx 2.4\pi$. Because the phase shift can only be measured modulo 2π, such a wide phase distribution would reveal no contrast at all and would only produce background. However, we are not dealing with a massive block of silicon but with thin plates. As illustrated in figure 3.11 the plates select only a small range of directions $\delta\theta \approx 0.05°$ resulting in $\delta k/k \approx 0.15\%$ and

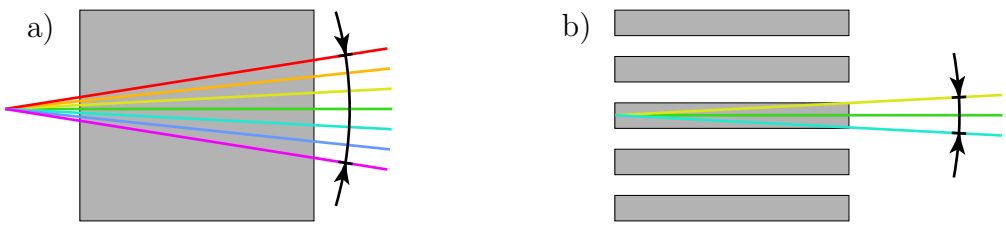

Figure 3.11: Beam direction and wave length are correlated due to Bragg's law. The beam fraction which penetrates the silicon plates in their whole length has only a very small divergence and therefore a narrow wave length distribution.

$\delta\varphi \approx 0.4\pi$. Neutrons with larger $\delta\theta$ do not travel inside the silicon over the full length but drop somewhere into the channel. Their path length inside silicon is completely random and they are lost for interference.

As a consequence we have to find a way to get rid of the phase contributions from neutrons travelling inside the silicon walls. There are different posibilities:

a) Applying an absorbing layer onto the wall faces (figure 3.12a). This would be the ideal solution because we would reduce the background as well. In order to absorb 99% of thermal neutrons we would need 85μm Cd or 31μm Gd or 6μm Cd-157. Unfortunately it doesn't seem feasible to apply such layers without contaminating and even blocking the channels as well.

b) Making the wall faces irregularly orientated in order to diffract the neutrons out of Bragg condition (figure 3.12b). Unfortunately this effect is too small. Two 45° edges result in a diffraction angle of $1.3 \cdot 10^{-4}$ degree which is smaller than the Bragg reflection width of about $5 \cdot 10^{-4}$ degree.

c) Using walls with irregular lengths (figure 3.12c). For a phase difference of 2π we need a length difference of 160μm, the so-called lambda thickness of silicon. A length variance of $\delta L = 160\mu$m would smear out the phase distributon over 2π and make it invisible in the experiment.

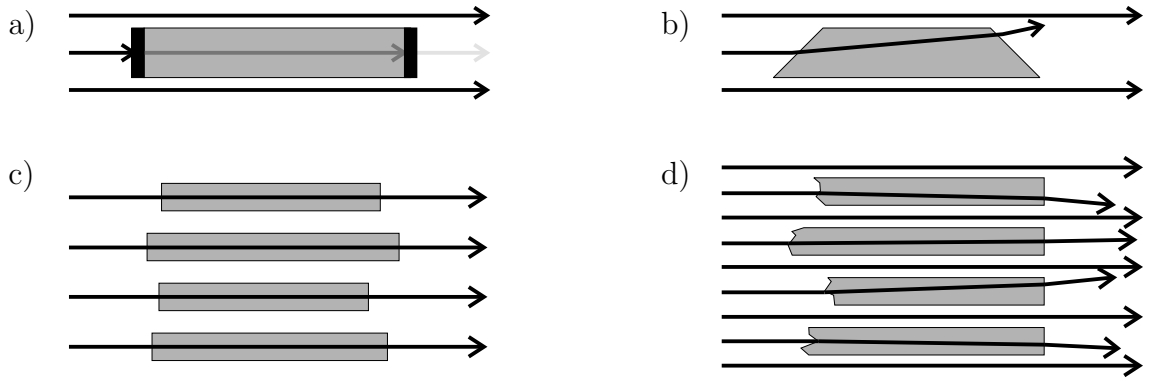

Figure 3.12: Techniques for suppressing the phase contribution from neutrons passing the silion plates: a) absorbing layers, b) diffraction with irregular face orientations, c) varying plate length. Figure d) shows a combination of b) and c) which is used in the real channel stacks.

So I decided to realize a combinatin of b) and c) by sandblasting the surface of the whole silicon stack. In order not to break the layers and to stabilize the stack during sandblasting I poured hot wax into the channels and let it become solid. Afterwards it was not so easy to get it out again because of capillary effects, but a solvent and a hot oven did the job. The final surface of the channel stack is shown in figure 3.13.

3.7 Bragg Reflections

So far we have treated the silicon walls only according to their Fermi pseudo potential. Since the walls are made of perfect crystal wafers we should also consider the possibility of Bragg

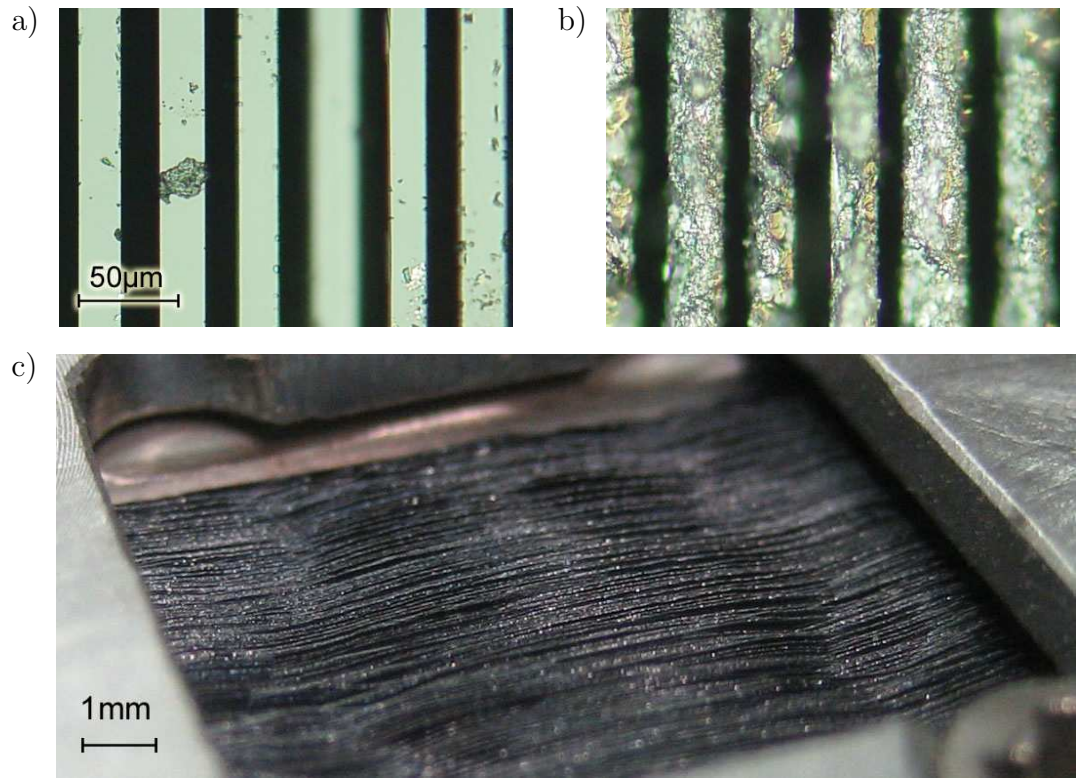

Figure 3.13: The wall faces before (a) and after (b) sandblasting. In addition a wavyness was introduced over the whole surface of the channel stack (c) so that the channel length varies in the order of the lambda thickness.

reflections. Silicon has a diamond crystal structure which provides reflection planes according to the following rules. Either all Miller indices h, k, l are odd or all are even and their sum is a multiple of 4. The wafer surface is oriented in $\langle 100 \rangle$ direction. The cutting edges facing the beam have $\langle 110 \rangle$ orientation. The angle enclosed between the beam and a certain plane is given by

$$\vec{a} = \begin{pmatrix} h \\ k \\ l \end{pmatrix}, \qquad \vec{b} = \begin{pmatrix} 1 \\ 1 \\ 0 \end{pmatrix}, \qquad \varphi = \sphericalangle(\vec{a}, \vec{b}) = \arccos\left(\frac{\vec{a} \cdot \vec{b}}{|\vec{a}| \cdot |\vec{b}|} \right). \tag{3.1}$$

We have to compare this angle with the Bragg angle of the plane for the wave length we use. Bragg's law for a given set of h, k, l reads

$$\lambda = 2\, d \sin\theta_B = \frac{2\, a_{\mathrm{Si}} \sin\theta_B}{\sqrt{h^2+k^2+l^2}}, \qquad a_{\mathrm{Si}} = \text{crystal constant of silicon.} \tag{3.2}$$

This relation is plotted in figure 3.14 for all possible crystal planes, which play a role in our wave length range. The bullets on the curves denote the points where the Bragg angle is equal to the angle between the plane and the beam direction $\langle 110 \rangle$. The wave lengths used in the experiments were 1.9Å and 2.7Å which is indicated by the gray horizontal lines in the plots. The 1.9Å line comes pretty near to the bullet of the $\langle 331 \rangle$ curve. Considering a beam divergence of 0.5° and a variation of the plate alignment of 0.05° we can assume, that part of the beam fullfills the Bragg condition. However, this is a very tiny fraction of the beam, because the reflection width of the Bragg peak is in the order of 10^{-4} degree and the crystal planes of different Bragg

types are always more or less in dispersive position, see figure 3.15. That's why we can very well neglect any effects coming from Bragg reflections in the wall material.

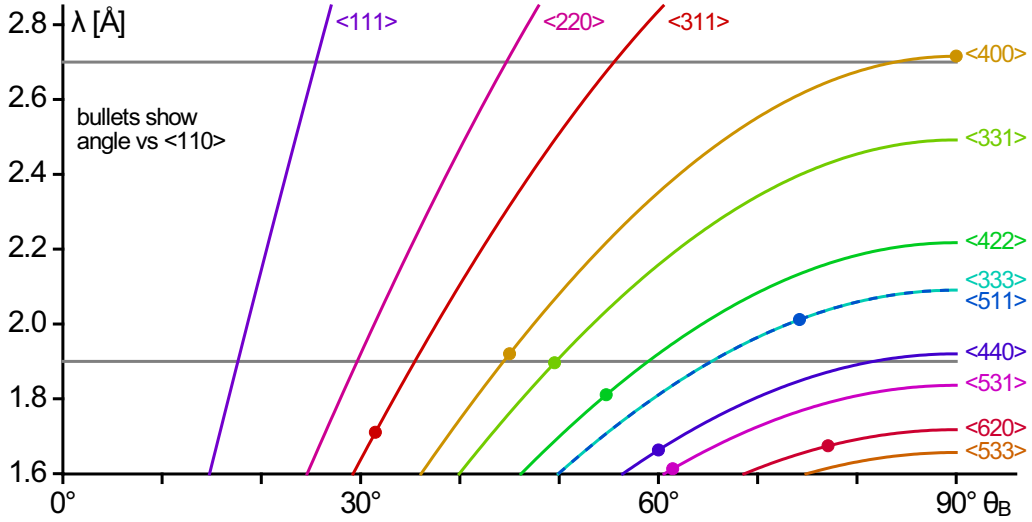

Figure 3.14: Bragg reflection curves for different types of plane orientations. The bullets represent the angles enclosed by the planes and the incident beam. The horizontal gray lines indicate the wave lengths used in the experiment. If they cross a bullet then a Bragg reflection occurs.

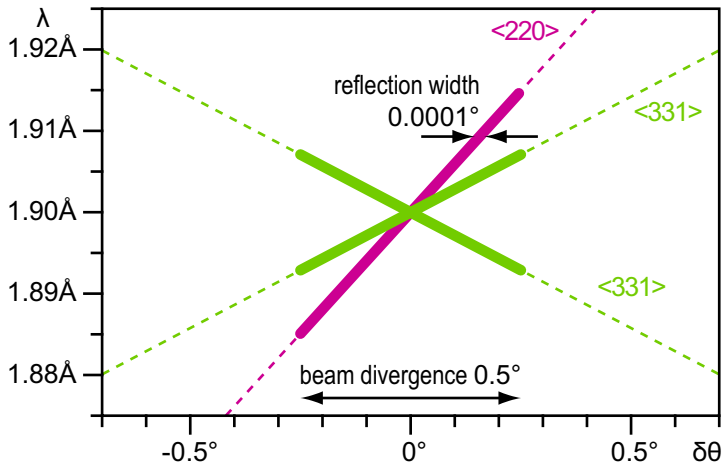

Figure 3.15: Dumont diagram. The dashed lines show the Bragg relations for the denoted Bragg planes. The beam divergence determines which range of these curves is affected, marked by the thick solid lines. These thick "lines" are actually areas with a width given by the Bragg reflection width. The neutron intensity is proportional to these areas. Neutrons which pass both the monochromator reflection $\langle 220 \rangle$ and the $\langle 331 \rangle$ reflection in the wall material have to fulfill both Bragg relations. Their intensity is given by the intersection area and amounts about 10^{-4} of the total beam intensity.

Chapter 4

Measurements

4.1 Setups

Most measurements have been done at the Institut Laue-Langevin (ILL) in Grenoble at the interferometry instrument S18 [KBB+00]. In addition, some measurements have been performed at the National Institute of Standards and Technology (NIST) in Gaithersburg, Maryland, USA [NAD+05]. The setups are shown in figure 4.1.

A triple Laue neutron interferometer consists of three crystal blades which split, reflect and recombine the neutron beam. The three blades are called Splitter, Mirror and Analyzer respectively. The two exit beams behind the Analyzer are called O beam and H beam. The crystal orientation has to be kept parallel in all three blades, that's why the blades are usually cut from a single crystal block. The Mirror can be realized in two parts in order to create more space for samples, see figure 3.2 and top of figure 4.1. Comprehensive information on neutron interferometry is given in [RW00].

At the ILL setup we have a perfect crystal silicon monochromator. The monochromator and the interferometer use the same Bragg planes $\langle 220 \rangle$ and are carefully aligned to each other. See top of figure 4.2. The intererometers are designed for Bragg angles of 30° and 45°. The former gives a wave length of 1.9Å using the maximum of the thermal neutron spectrum at the ILL. The latter gives a wave length of 2.7Å with about half the intensity.

At the NIST setup we have a double graphite monochromator system. The second monochromator focuses the beam vertically to increase the intensity. See bottom of figure 4.2. The interferometer uses the 111-Bragg planes at a Bragg angle of 25.6° and a wave length of 2.7Å.

4.2 Measurement Process

For measuring the phase shift of a sample an auxiliary phase shifter is required. The phase shifter is a blade of a non-absorbing and non-scattering material (e.g. Si, Al or Al_2O_3) which intersects both beams at a position where the beams are not parallel. If the phase shifter is parallel to the interferometer blades, both beam paths have the same optical path length. If the phase shifter is rotated, then the optical path length is increased in one path and decreased in the other, resulting in a controlled phase shift between the two paths. See section 5.5 for

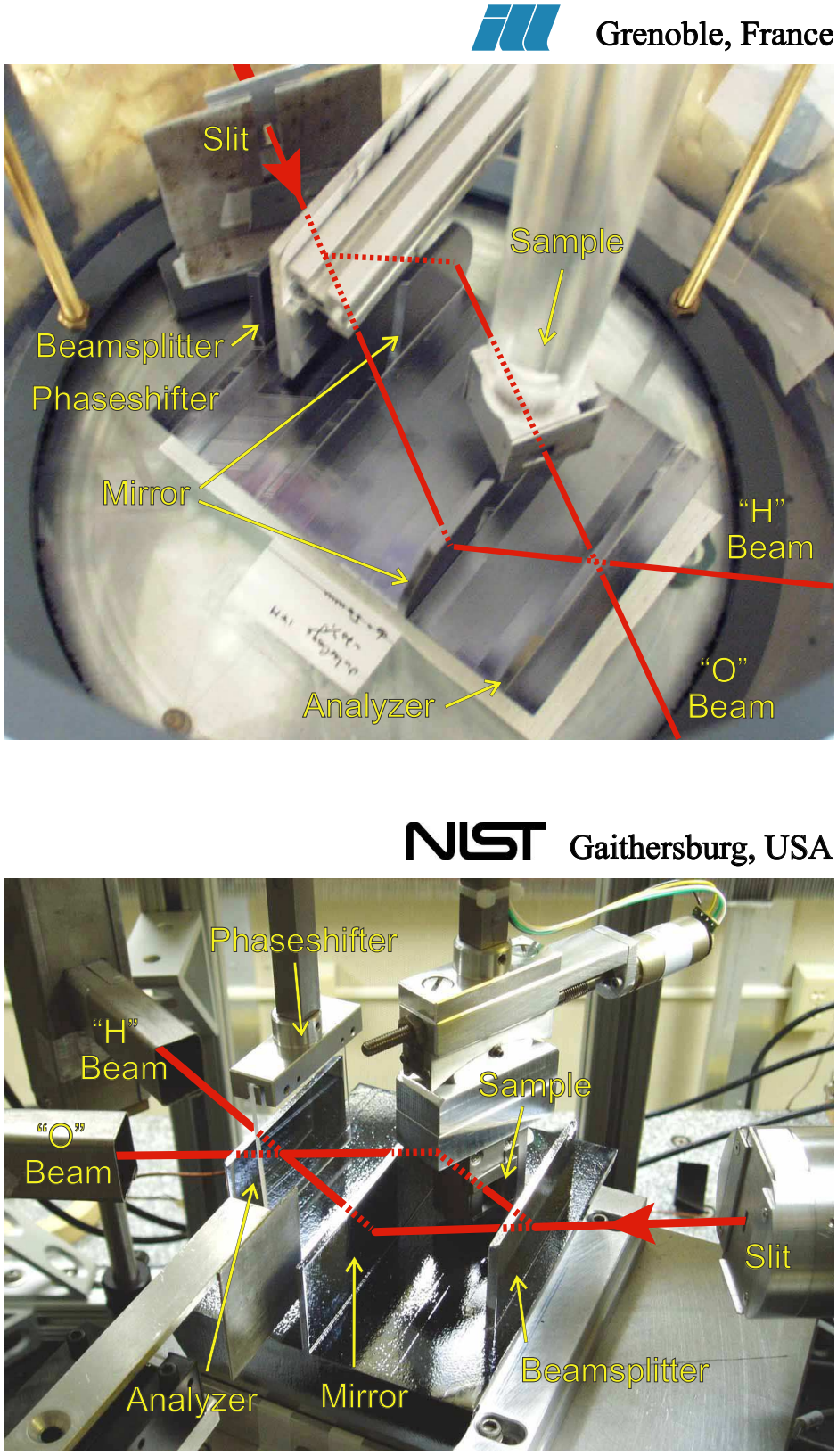

Figure 4.1: The interferometer setups at ILL and NIST.

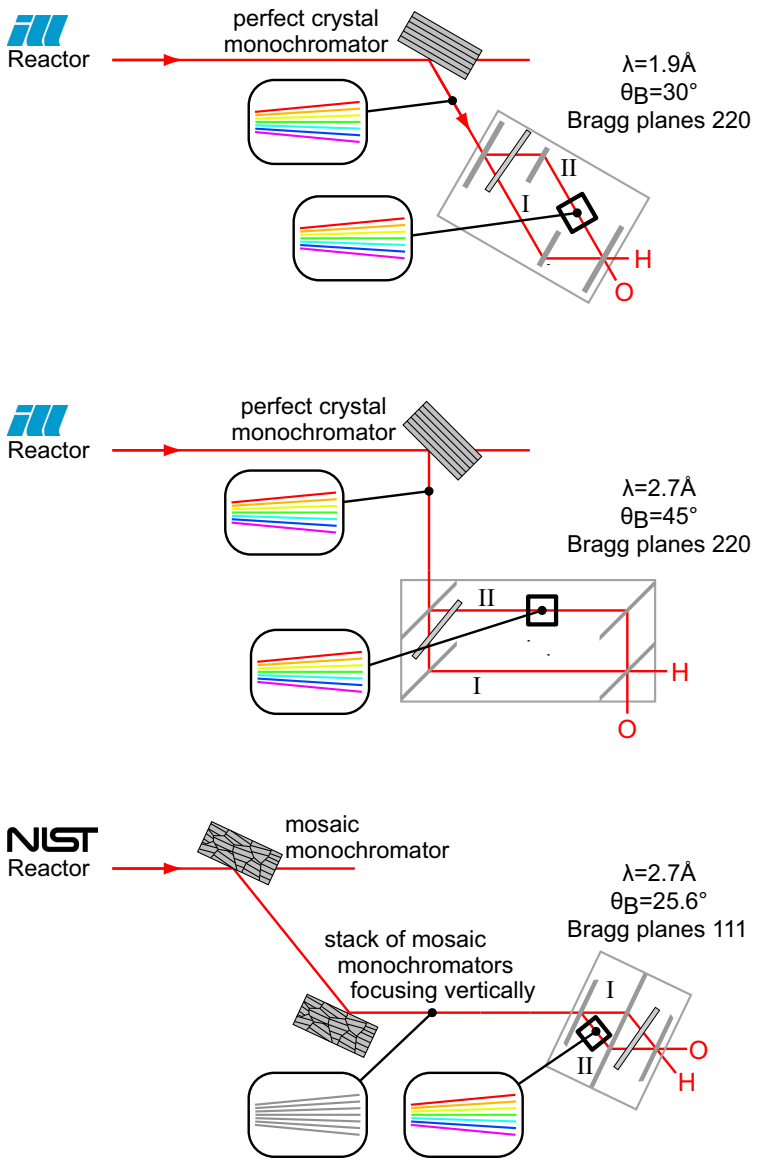

Figure 4.2: Sketches of the different setups. At the NIST setup the monochromator is a mosaic crystal which does not create a correlation between wave length and angle. Nevertheless the beam properties should be the same after the first reflection in the interferometer.

details. As a consequence of the phase shift, the intensity of the exit beams oscillates between the O and the H beam. A mathematical description is given in chapter 5.

The phase shift of a sample is measured in the following way. If we rotate the phase shifter in the empty interferometer (without sample) we get the intensity oscillations as shown in figure 4.3a). We can make a sine fit and get an absolute phase of the oscillation in respect to the parallel position of the phase shifter. Then we insert the sample into one beam path and take again an interferogram, fit the data and get the phase, as shown in figure 4.3b). The difference of the phases is the phase shift caused by the sample. We can put the sample into the other beam and measure the phase shift there, figure 4.3c). Usually one should get the same phase shift with an opposite sign. (Surprisingly, this is not the case with the channel stack.)

The measurement of one interferogram with the channel stack in the interferometer takes

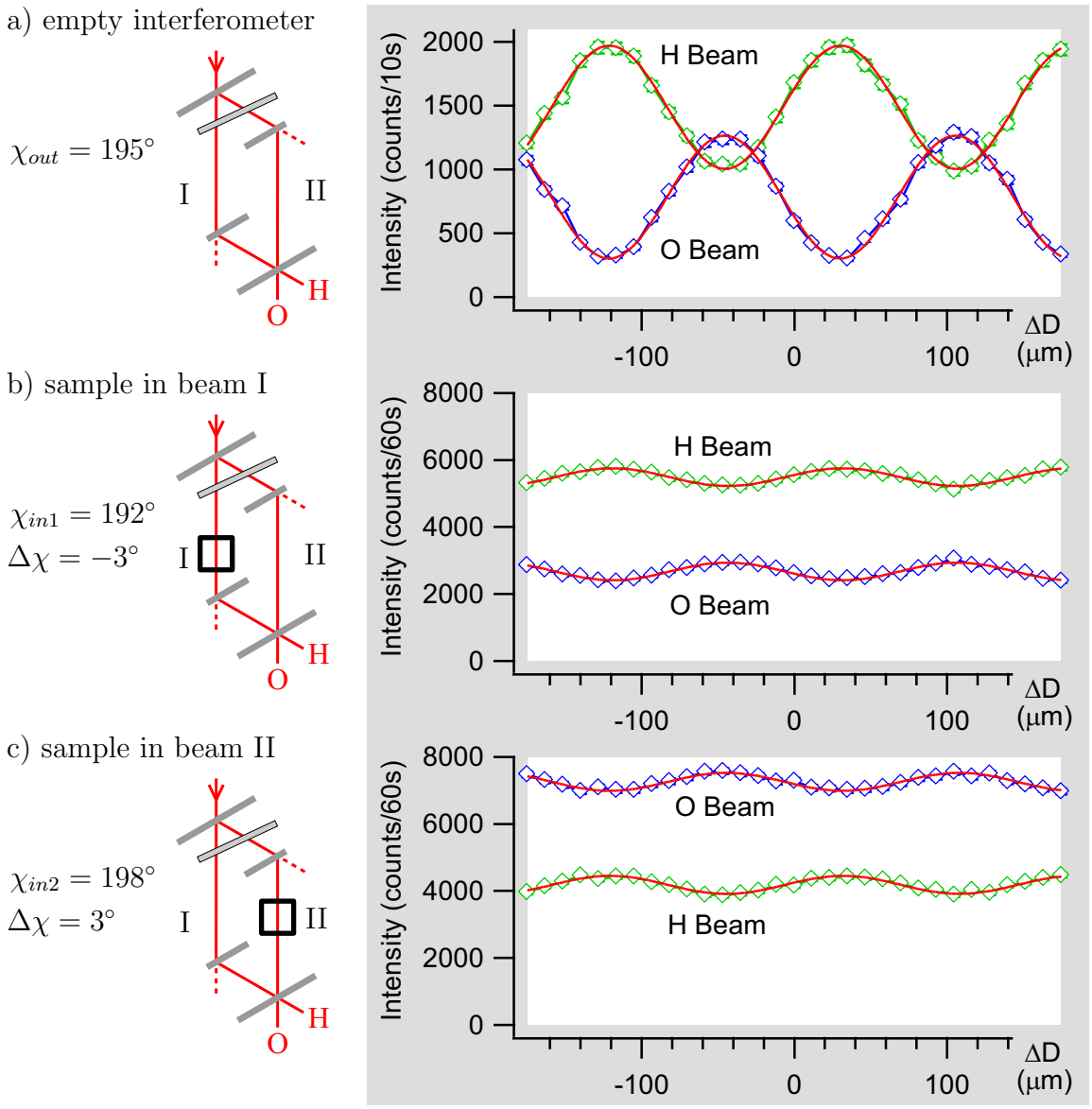

Figure 4.3: The measurement process. For each sample position an interferogram is taken, which shows the intensities of the O and the H beam as a function of the optical path length difference ΔD which is controlled by the phase shifter angle. Fitting the data with a sine curve gives an absolute phase χ. The phase difference to the empty interferometer phase gives the phase shift made by the sample.

approximately one hour. During that time the reference phase (phase of the empty interferometer) can drift by a couple of degrees because of environmental influences, especially temperature changes and vibrations. In spite of extensive thermal and vibrational isolation of the setups, these phase drifts can never be completely suppressed. This means that the phases are not comparable if the interferograms with and without the sample are taken one after the other. Therefore the interferograms must be taken in "parallel" mode as sketched in figure 4.4. After the phase shifter is set to a certain angle, the sample is moved in and out and the intensities are measured for each position. Then the phase shifter is moved to the next angle and again the measurement is done for all sample positions etc. If the reference phase drifts, then the shape of all interferograms is changed in a similar way and the phase shift between the curves

is not affected. A variation of this mode is the "alternating" mode which saves a little bit time on sample movement and even improves the accuracy in case of phase drifting [KHB+05].

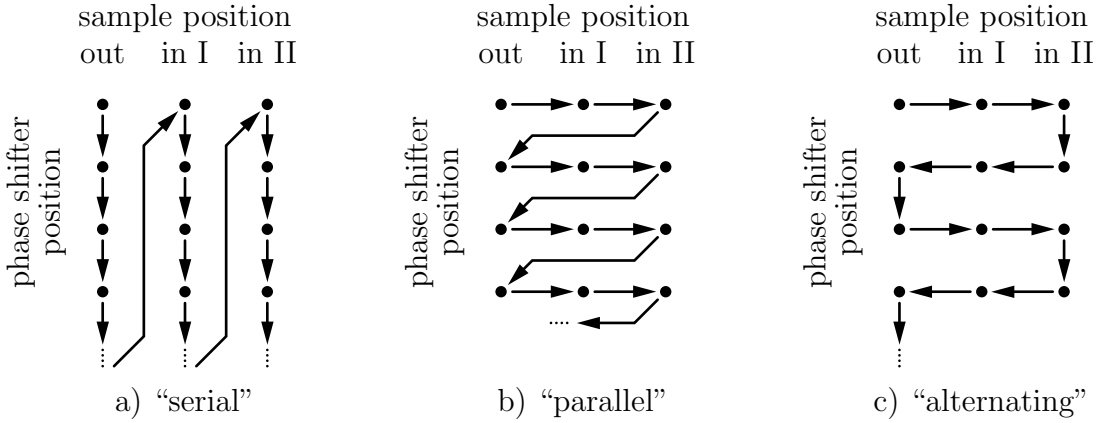

Figure 4.4: a) The interferograms for sample out and sample in are measured one after the other. b) The interferograms are measured in an interlaced way. c) A variation of b) which saves time and improves the accuracy.

4.3 Interferograms

Figure 4.3 also illustrates the typical features of the channel interferograms. The contrast is very low, about 5% to 10%, compared to the 60% contrast without the channels. The reason is that about half of the neutrons hit the faces of the wall plates and don't enter any channel. The other half, which is passing through the channels, is partly diffracted out of Bragg condition. This means that many neutrons are either lost completely or do not contribute to the interference but just increase the background.

In figure 4.3c) the O beam has larger intensity than the H beam, which is rather uncommon. The reason is, that the sample is in position IIb (cf. fig. 3.2) and in this position all neutrons which are scattered out of Bragg condition go straight through the last interferometer blade into the O detector. In the case of figure 4.3b) these neutrons are already filtered out by the mirror blade. In the empty interferometer, figure 4.3a), the mean H intensity is higher than the mean O intensity because of the intrinsic properties of neutron interferometers. See formula (5.34).

4.4 Data Fitting

The raw data of an interferogram consists of the beam intensities o_i and h_i measured at the phase shifter angles δ_i. $\delta_i = 0$ means that the phase shifter is parallel to the interferometer blades. With (5.56) we convert δ_i to the phase shift

$$x_i = kD_0(n-1)\left(\frac{1}{\cos(\theta_B+\delta_i)} - \frac{1}{\cos(\theta_B-\delta_i)}\right). \tag{4.1}$$

with the phase shifter thickness D_0 and the index of refraction n, see section 5.5. The statistical error (standard deviation) of the raw data is given by $\sigma_{oi} = \sqrt{o_i}$ and $\sigma_{hi} = \sqrt{h_i}$. We feed the

data and its errors to a least square fit routine, using the fit function

$$y_o(x) = A + B\sin(Cx + D). \tag{4.2}$$

with the four fit parameters A (offset), B (amplitude), C (periode) and D (phase). We obtain the fit parameters and its errors. If B comes out negative we make it positive and add π to the phase. Besides the phase we can retrieve the contrast or visibility $V = A/B$.

We can reduce the statistical error if we make also use of the H data. There are different methodes to do so.

1. Fit o_i and h_i independently:

$$\text{fit } o_i \pm \sqrt{o_i} \text{ with } y_o(x) = A_o + B_o\sin(C_o x + D_o) \tag{4.3}$$

$$\text{fit } h_i \pm \sqrt{h_i} \text{ with } y_h(x) = A_h - B_h\sin(C_h x + D_h) \tag{4.4}$$

   Obtain the fit parameters and calculate the weighed averages:

$$X = X_o\frac{\sigma_X^2}{\sigma_{Xo}^2} + X_h\frac{\sigma_X^2}{\sigma_{Xh}^2}, \qquad \sigma_X^2 = 1/\left(\frac{1}{\sigma_{Xo}^2} + \frac{1}{\sigma_{Xh}^2}\right), \qquad X \in \{A, B, C, D\} \tag{4.5}$$

Usually we obtain better results (smaller errors) if we eliminate the fluctuations of the beam intensity. We know that the intensities o_i and h_i correspond to probabilities which always sum up to one. In other words, the sum $o_i + h_i$ can be normalized to a constant value, provided that no neutrons in the O or H beam are lost. This can be very well fulfilled because the efficiency of a neutron detector is practically 100%. The normalization is done by one of the following methodes.

2. Calculate the mean total intensity $t = \langle o_i + h_i \rangle$ and normalize all data $o_i, \sigma_{oi}, h_i, \sigma_{hi}$ by a multiplication by $t/(o_i + h_i)$. Continue with methode 1.

   This methode obtains better results and is quite popular, because the normalized data still shows the original count rate. Nevertheless the error calculation is a bit "dirty" because the data values o_i and h_i are no longer statistically independent after normalization. The correct way is shown in methode 3. The differences are in the order of one ‰.

3. Convert the O intensity to a probability value and calculate the error according to the law of error propagation.

$$p_i = \frac{o_i}{o_i + h_i}, \qquad \sigma_i = \sqrt{\left(\frac{\partial p_i}{\partial o_i}\right)^2\sigma_{oi}^2 + \left(\frac{\partial p_i}{\partial h_i}\right)^2\sigma_{hi}^2} = \sqrt{\frac{o_i h_i}{(o_i + h_i)^3}} \tag{4.6}$$

   A sine fit to this data gives the final result. There is no need to fit $h_i/(o_i + h_i)$ which would be just the complement to one. If you want to plot the interferogram with the original count rate you can still multiply p_i and σ_i by the mean total intensity t.

   All measurements have been evaluated with methode 3.

The statistical error can be further reduced by repeating the measurement a couple of times. Each measurement yields a phase shift value $\varphi_i \pm \sigma_i$. The weighted mean value is given by [Bra75]

$$\overline{\varphi} = \frac{\sum_i \frac{\varphi_i}{\sigma_i^2}}{\sum_i \frac{1}{\sigma_i^2}} \tag{4.7}$$

Using the error propagation law we get the statistical error of the mean value:

$$\overline{\sigma}_{stat} = \sqrt{\frac{1}{\sum_i \frac{1}{\sigma_i^2}}} \tag{4.8}$$

On the other hand we can calculate the total error of the mean value by using the standard deviation of the single values around the mean value. Taking into account the different weights of the single values we get the formula [Bra75]

$$\overline{\sigma}_{tot} = \sqrt{\frac{\sum_i \frac{1}{\sigma_i^2}(\varphi_i - \overline{\varphi})^2}{(N-1)\sum_i \frac{1}{\sigma_i^2}}} \tag{4.9}$$

The results in the sections below are always given with both errors in the form "$\overline{\varphi} \pm \overline{\sigma}_{stat} (\pm \overline{\sigma}_{tot})$". By comparing both errors we can check against systematical errors. $\overline{\sigma}_{tot}$ being larger than $\overline{\sigma}_{stat}$ means that the statistical error alone cannot explain the total error. In this case some systematical error must have occured.

All experiments have been evaluated with the computer software "Igor Pro 4".

4.5 Channel Alignment

The channels have to be aligned very well to the beam. This is done by blocking the reference beam in the interferometer and measuring the intensity which is transmitted by the channels and still reflected by the next interferometer blade. See figure 4.5.

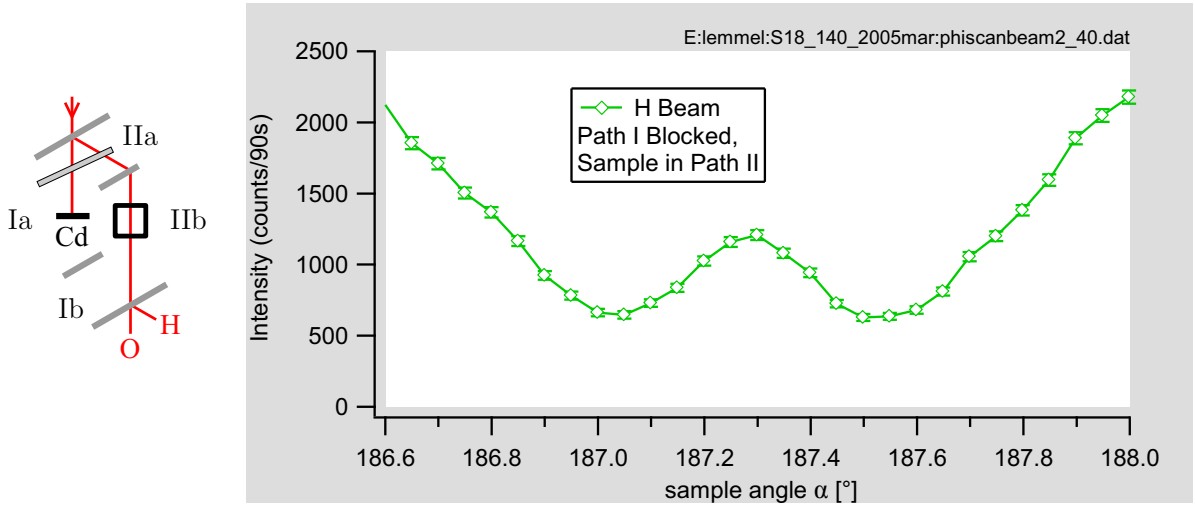

Figure 4.5: The typical W-shape of the alignment scan for the channel angle

Typical alignment scans have a W shape. The central peak can be understood as the convolution of the beam divergence and the channel transmission curve as explained in section 2.8. The increasing intensities on the sides come from beam trajectories which partially penetrate the silicon walls.

4.6 Phase Shift Measurements

The measurements are presented in chronological order. They have been performed under various conditions and parameters as listed below. The right column shows the expected phase shift values as calculated in section 2.1.2.

Parameters	Expected Phase	
Channel Length		
• 1 cm channel length		
• 2 cm channel length	$L=1$cm	$L=2$cm
Setups		
• ILL30: $\theta_B = 30°$, $hkl = 220$, $\lambda = 1.9$Å, interferomerters: skew symmetric, small symmetric	0.53°	0.87°
• ILL45: $\theta_B = 45°$, $hkl = 220$, $\lambda = 2.7$Å, interferomerters: large skew symmetric, double loop	0.70°	1.19°
• NIST: $\theta_B = 25.6°$, $hkl = 111$, $\lambda = 2.7$Å, interferomerters: symmetric	0.70°	1.19°
Wall Faces	blank faces could	
• blank	allow wall contrib.	
• sandblasted		
Channel Angle Measurements have been done at different angle positions around the central peak of figure 4.5.	no effect expected	
Position in the Interferometer In principle an interferometer offers four different sample positions with different coherence properties of the beam. Some positions may be inaccessible because of the interferometer geometry. See figure 3.2.	no effect expected	

If the phase shift values obtained in the different sample positions are compared to each other, one has to take into account the following points, as illustrated in figure 4.6.

a) Switching the beam path of the sample inverts the phase shift. The illustration shows how the wave packet coming from beam path I is ahead or behind, depending on the sample position. A mathematical description is given in section 5.3.

b) If the phase shifter is in position a then a counter clockwise rotation increases the optical path length in beam I and decreases it in beam II. If the phase shifter is in position b then it is the other way round. In the data evaluation this has been compensated by inverting the phase shifter angle if the phase shifter is in position b.

c) The correlation between the beam angle and the wave length is inverted by each Bragg reflection. If the sample angle α is increased in position Ib or IIa then the channels are aligned to shorter wave lengths. In position Ia and IIb it is the other way round.

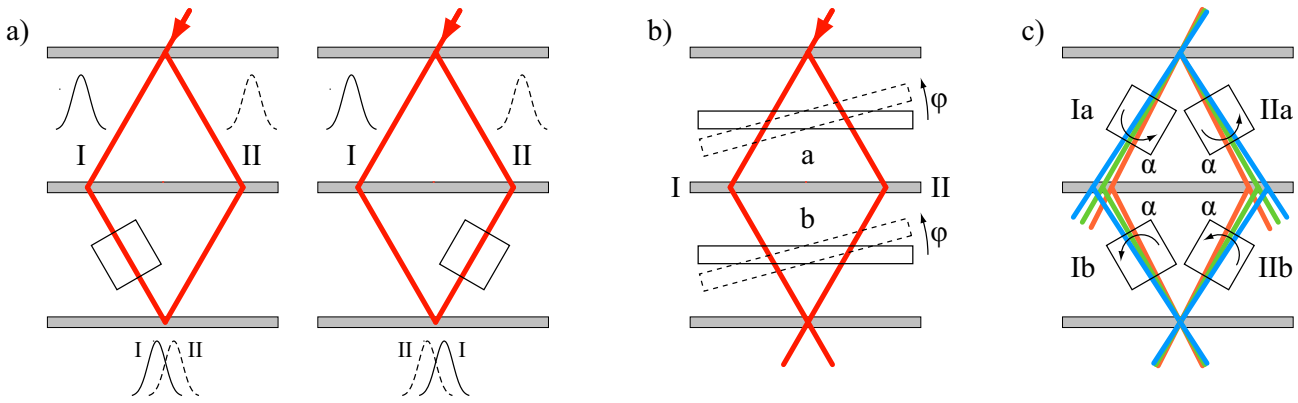

Figure 4.6: Effects to keep in mind when measuring the sample at different positions within the interferometer.

4.6.1 1 and 2 cm channel length, ILL30, November 2002

The channels have been aligned to the parallel position, i.e. to the central peak of figure 4.5. The results are given in figures 4.7 to 4.9.

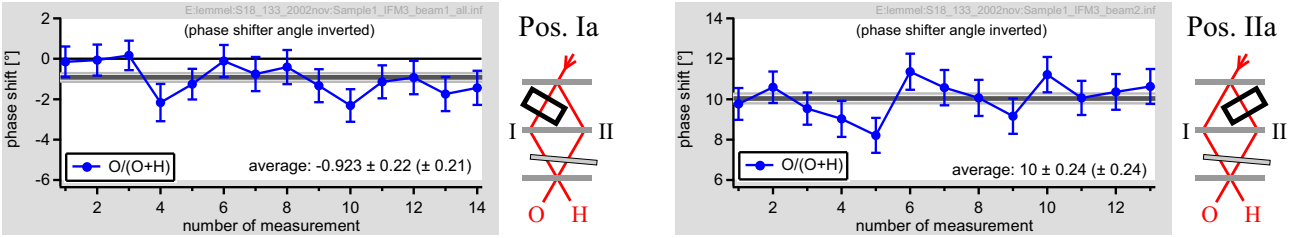

Figure 4.7: The 1-cm-sample measured in the small interferometer at the setup ILL30. The phase shift is -0.9° at position Ia and +10° at position IIa.

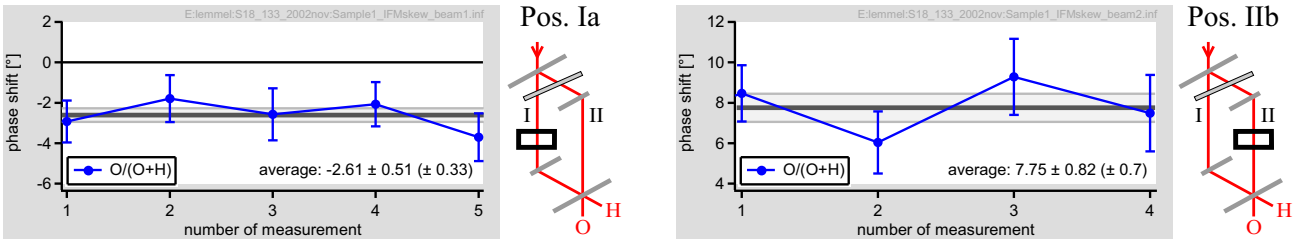

Figure 4.8: The 1-cm-sample measured in the skew symmetric interferometer at the setup ILL30. The phase shift is -2.61° at position Ia and +7.75° at position IIb.

The magnitude of the phase shift is up to 10° which is about ten times larger than expected, and the phase shift has different absolute values in beam I and II.

After this measurement the samples have been sandblasted as described in section 3.6, in order to make sure that the silicon walls do not contribute to the interference. However, this measure didn't seem to make any difference. The asymmetry and the too large phase value remained.

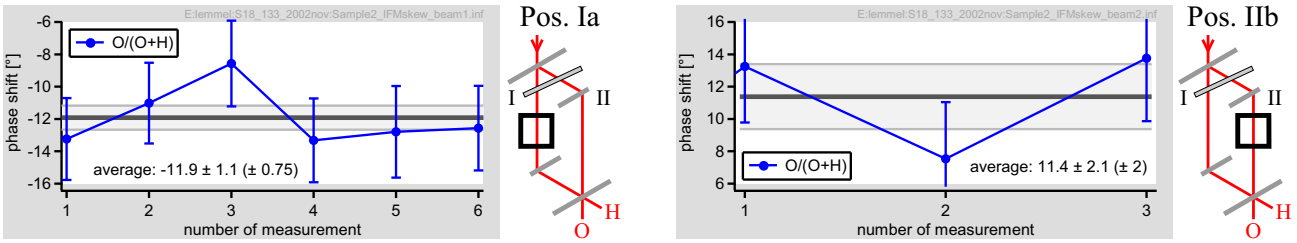

Figure 4.9: The 2-cm-sample measured in the skew symmetric interferometer at the setup ILL30. The phase shift is -11.9° at position Ia and +11.4° at position IIb.

4.6.2 1 cm channel length, ILL30, May 2003

The 1-cm-sample has been measured in all four interferometer positions at different alignment angles. The results are shown in figure 4.11. The positions Ia and IIb have also been measured with the skew symmetric interferometer, see figure 4.10. The scans labeled "sample alignment" show the central peak of the W-curve. The phase shift has been measured at different points around this peak.

The contrast curve reproduces the intensity of the alignment peak as expected. At larger angles where the W-curve increases again the contrast remains zero. (Not shown here.)

The phase shift shows a clear drift with the sample angle α. A possible explanation would be a wave length dependency of the phase shift. The channel stack acts like a collimator with an acceptance angle of about 0.05° which is smaller than the beam divergence of about 0.4°. By changing the sample angle a different beam direction is selected which changes the center of the wave length distribution according to Bragg's law.

The drift of the phase shift with the sample angle shows different directions in the four sample positions of the interferometer. This is consistent with the wave length explanation. At

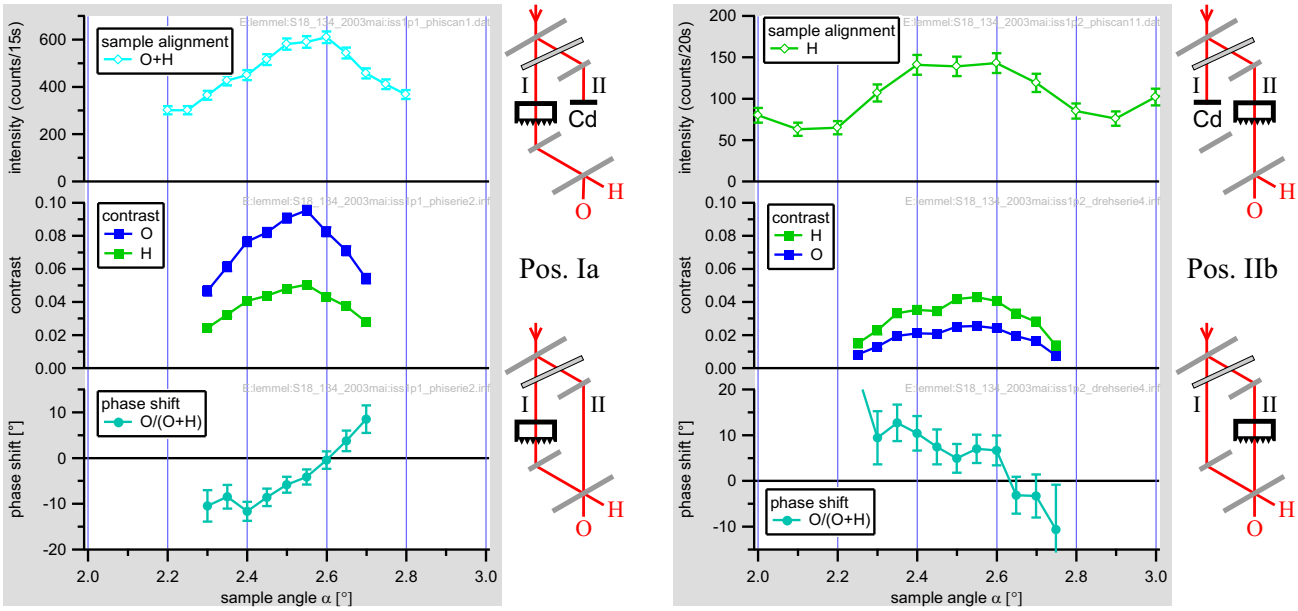

Figure 4.10: The 1-cm channel measured in the skew symmetric interferometer at the setup ILL30.

the position IIa the phase shift is increased with α while it is decreased at position IIb. This is because the mirror blade in between reverses the correlation between λ and α, see figure 4.6c. The drifts between position Ib and IIb are parallel because they are reversed two times: First again by the different number of Bragg reflections and second because a negative phase shift in beam I is equivalent to a positive phase shift in beam II. No clear drift can be seen in position Ia. However when the measurement was repeated in the equivalent position of the skew symmetric interferometer the drift shows up with the expected slope.

In the phase shift calculations (section 2.1.2) a phase drift with λ arises only from the neutrons which go all the way through the silicon walls. Would it be possible that the silicon walls still contribute to the interference, in spite of the sandblasting? The slope of this drift

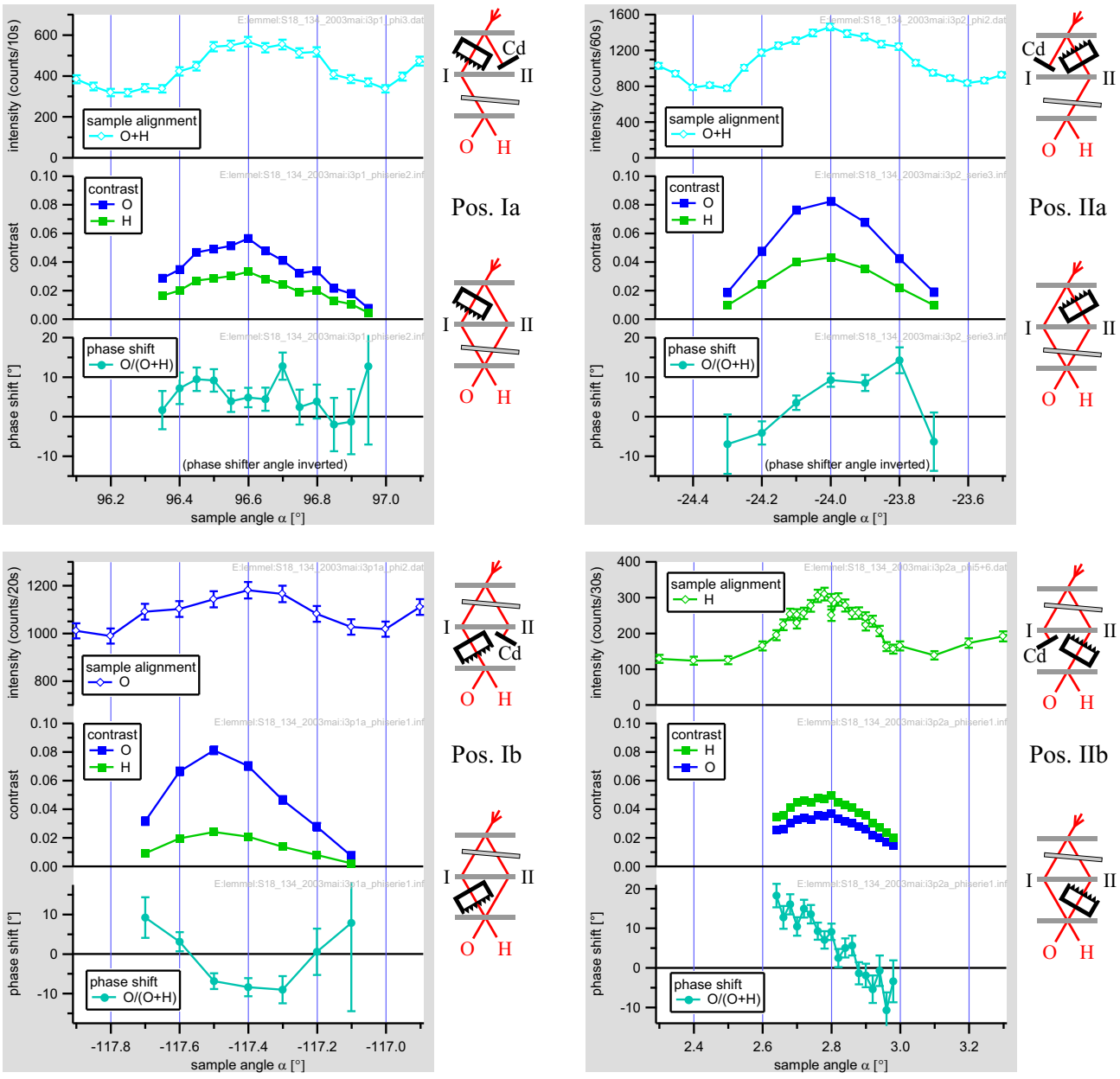

Figure 4.11: The 1-cm channel measured at different sample angles in the small symmetric interferometer at the setup ILL30.

would be:

$$\text{phase shift of silicon: } \chi = \Delta k \cdot L = kL\left(1-\sqrt{1-V/E}\right) \approx kLV/(2E) = L\frac{Vm}{\hbar^2 k} = L\frac{Vm}{\hbar^2 2\pi}\lambda = \\ = \frac{LVm}{\hbar^2\pi}\, d\, \sin\theta_B \tag{4.10}$$

$$\text{slope of phase shift: } \frac{\mathrm{d}\chi}{\mathrm{d}\theta_B} = \frac{LVm}{\hbar^2\pi}\, d\, \cos\theta_B \tag{4.11}$$

For 1 cm silicon and $\theta_B = 30°$ we get $\chi \approx 63 \cdot 360$ and $\frac{d\chi}{d\theta_B} = 690$ degree phase per degree angle. For 2 cm silicon both values double. This does not fit very well to the slope of 50 to 150 in the measurements. In addition, it would be rather unlikely that the silicon phase shift of 63 orders ends up in values which are nicely grouped around zero. It could be any arbitrary value between 0 and 360°.

4.6.3 2 cm channel length, ILL30, July 2003

The 2-cm channels could only be measured in the skew symmetric interferometer because it is too large for the small one. Consequently it could only be measured in the positions Ia and IIb. The result is shown in figure 4.12.

Each sample angle is measured a couple of times in order to improve the statistics. Nevertheless the fluctuations are still high because of the low contrast. No clear drift of the phase shift can be observed. It makes no significant difference whether the rough or the blank side of the channel stack face the beam. The phase shifts are again larger than expected and not symmetric in beam I and II.

The central peak in the alignment scans is more or less missing completely. At that time I only thought of a bad channel geometry. If some traces of wax from the sandblasting procedure were left in the channels then the silicon plates could be sticky and generate stress to each other resulting in bent plates. However, in later measurements I got very clear W shapes of the alignment scans and I found out that the beam divergence plays an important role.

4.6.4 NIST, February 2004

The NIST measurements show the sharpest alignment peaks and the highest contrast ever observed with our channel stacks. This is probably due to a very narrow beam divergence. Other differences to the previous measurements were:

- longer wave length, 2.7Å instead of 1.9Å
- Bragg planes $\langle 111 \rangle$ instead of $\langle 220 \rangle$
- mosaic monochromator instead of a single crystal (figure 4.2)

The longer wave length changes the expected phase shift from 1° to 1.2°. The other parameters shouldn't make any difference to a phase shift measurement.

The disadvantages at NIST were the longer measurement time due to the lower intensity and the rather unflexible sample robot which both prevented us from measuring the channels at different interferometer positions.

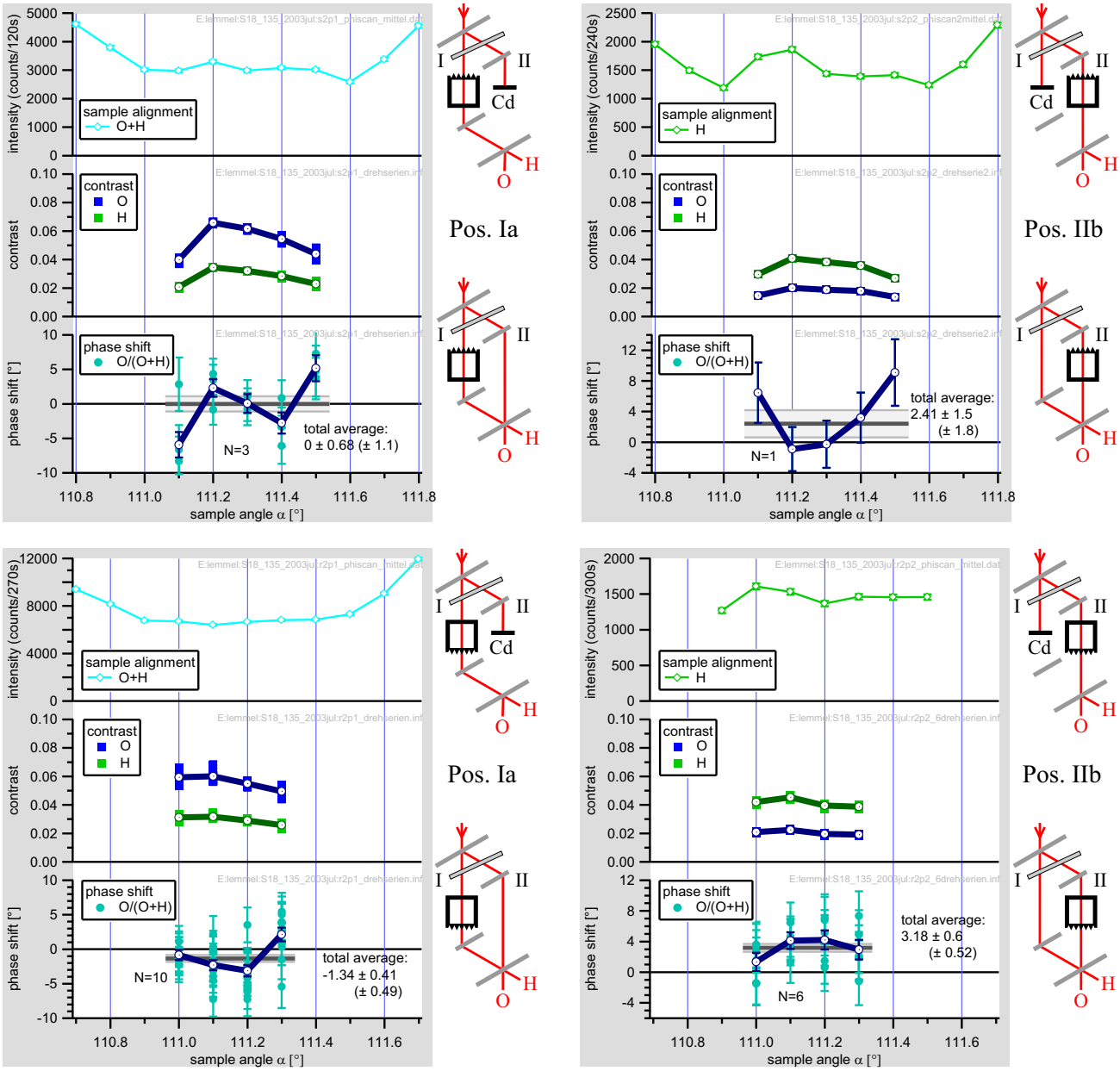

Figure 4.12: The 2-cm sample measured in the skew symmetric interferometer at the setup ILL30. In the upper measurements the rough side of the silicon walls face the beam. In the lower measurements the sample has been turned around by 180°.

Figure 4.13 shows the result for both channel stacks measured at position IIa. The right figure is directly comparable to the ILL measurement shown on the top right of figure 4.11. The drift of the phase shift with α does not appeare in the NIST measurement.

The measurement of the 2-cm channels was repeated over a long time to reduce the statistical error. The result is given in figure 4.14. The stability of the setup was very good but not perfect. The overall mean value of the phase shift is $-0.375 \pm 0.16(\pm 0.16)°$. Averaging over measurements 0 to 45 give $-0.68 \pm 0.22(\pm 0.22)°$. Measurements 45 to 84 give $0 \pm 0.23(\pm 0.22)°$. This means that the phase shift has increased a little bit during the time.

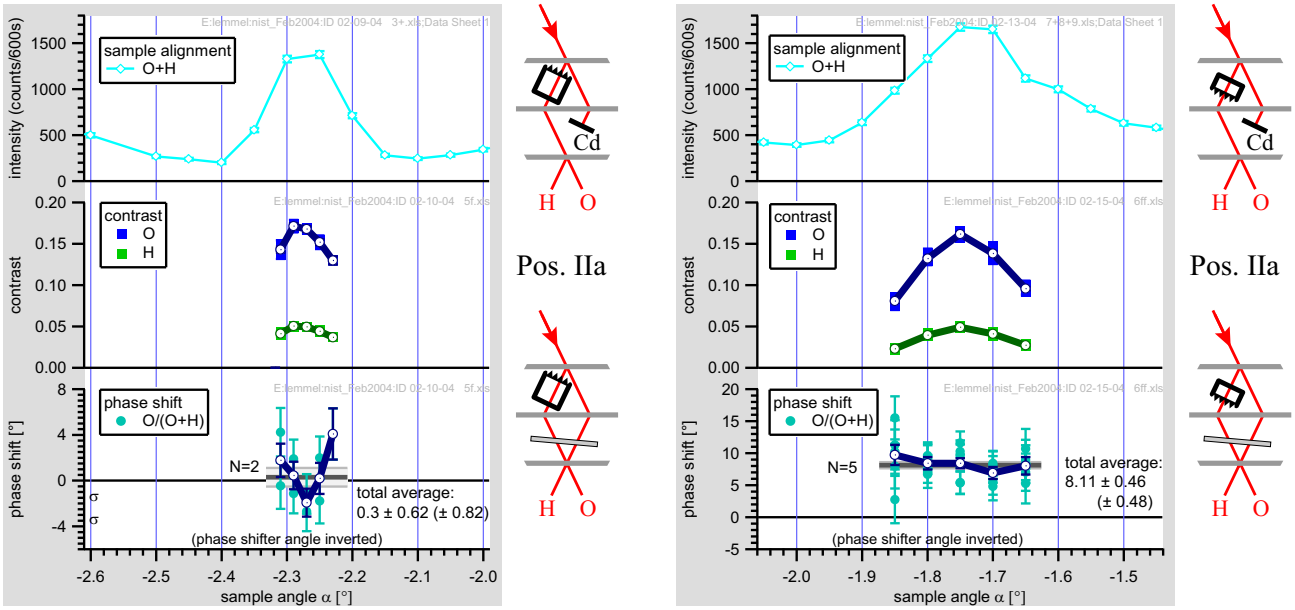

Figure 4.13: Both samples measured at NIST. The alignment curve shows a very sharp center peak and the contrast is accordingly high. No drift of the phase shift with α can be recognized.

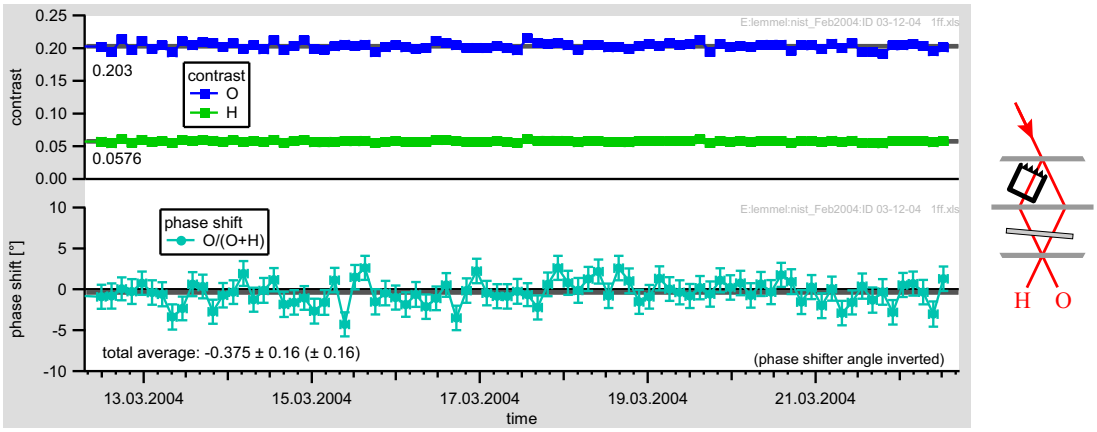

Figure 4.14: The 2-cm sample measured over a long periode of time.

4.6.5 ILL45, May 2004

These measurements with a Bragg angle of 45° and $\lambda = 2.7$Å were performed in order to check if the NIST results could be reproduced at the ILL, now using the same wave length. The only differences to the NIST setup were the Bragg planes and the monochromator type which, as already pointed out, should have no influence on phase shift measurements.

First I tried to reproduce the sharp alignment with a small beam divergence. Figure 4.15 shows the geometry of the slits and how a narrow beam divergence reduces the background and makes the peak sharper. In the end I used a 3mm slit for the measurements.

The results of the phase shift measurements are given in figure 4.16. The phase shift shows a strong drift with the sample angle. The right figure (position IIa) is directly comparable to the left of figure 4.13, where no phase drift is observable.

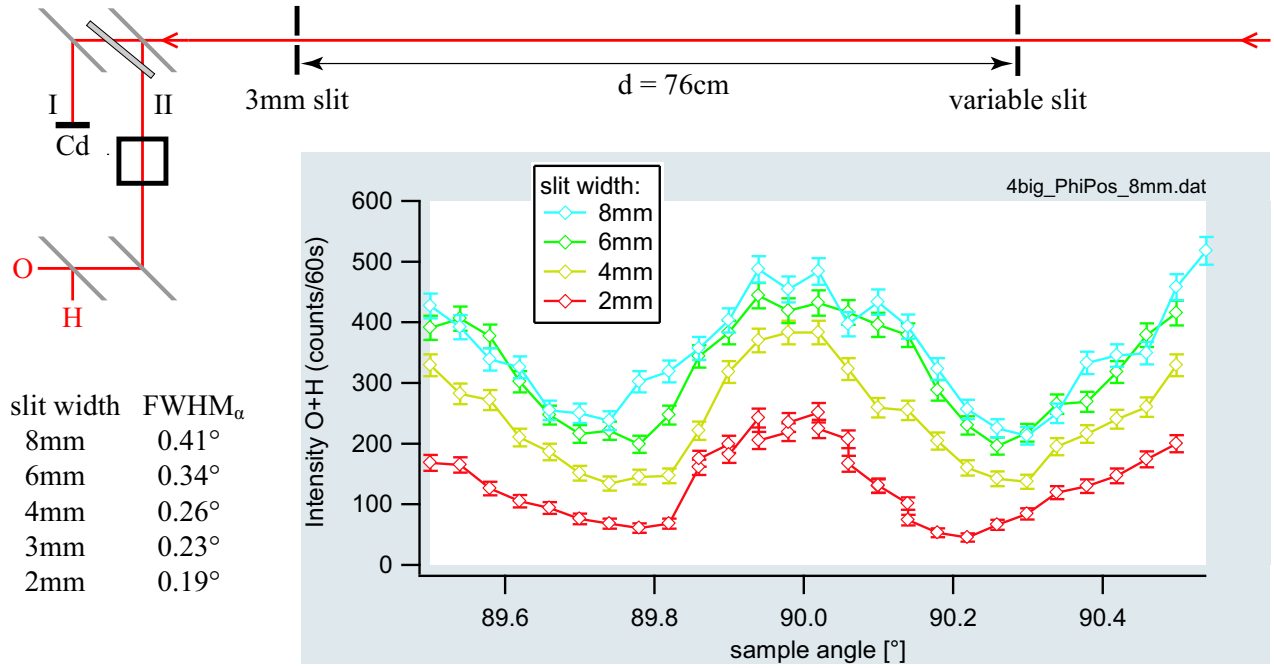

slit width	FWHM$_\alpha$
8mm	0.41°
6mm	0.34°
4mm	0.26°
3mm	0.23°
2mm	0.19°

Figure 4.15: The alignment scan of the 2-cm sample in the large interferometer for different values of the beam divergence. The beam is coming from the right, passing two slits. The first slit width w_1 is variable, the second w_2 is fixed at 3 mm. The distance d between the slits is 76 cm. The beam divergence is given by $\mathrm{FWHM}_\alpha = \arctan(\frac{w_1+w_2}{2}/d)$.

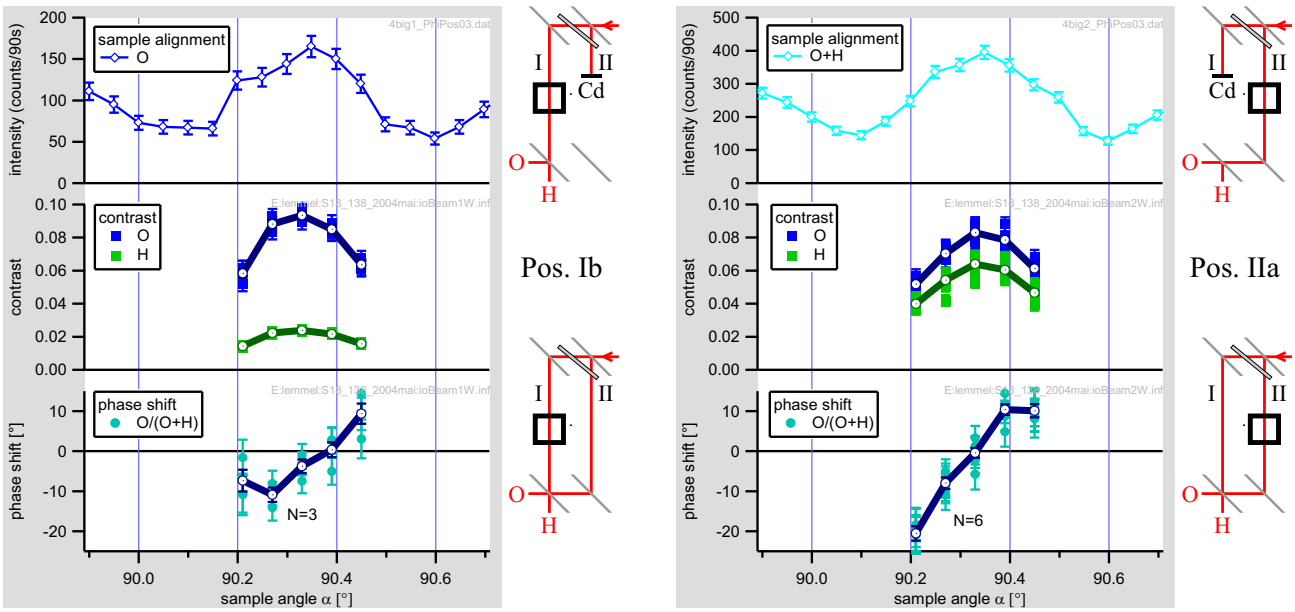

Figure 4.16: The 2-cm sample in the large interferometer.

The slope of the phase drift is equal in position Ib and IIa. This is not consistent with the conjecture derived from figure 4.11 that the phase drift could be proportional to the wave length. In figure 4.11 the slope in position Ib and IIa is opposite.

Figure 4.17 shows a long term measurement. The fluctuations are quite strong, which is also expressed in the total error being larger than the statistical error. The reason is probably the strong phase drift in figure 4.16. As long as this drift is not understood and cannot be controlled, it is quite useless to make a precision measurement.

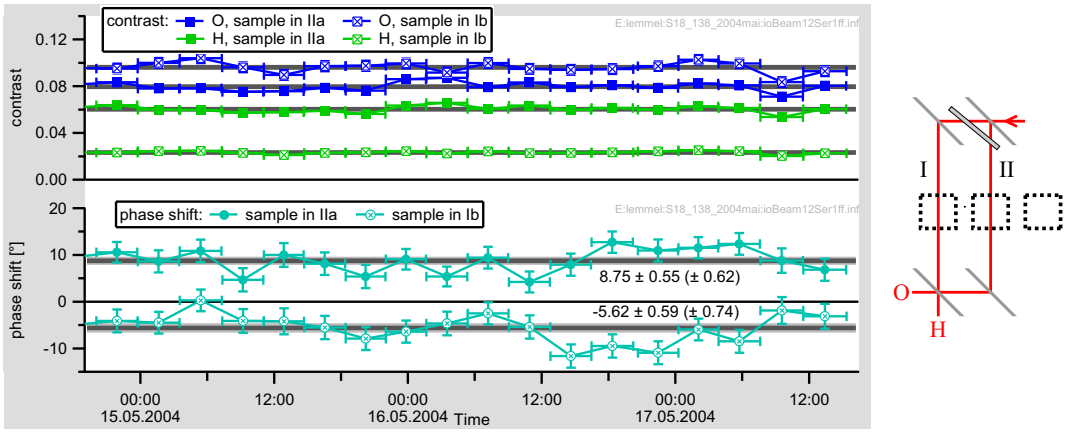

Figure 4.17: A long term measurement for the positions Ib and IIa.

4.6.6 ILL30, March 2005

Now we wanted to check if the phase shift is sensible to a small change of the Bragg angle. Small means some 0.1° which is the periode of the intensity oscillation of the Laue reflection

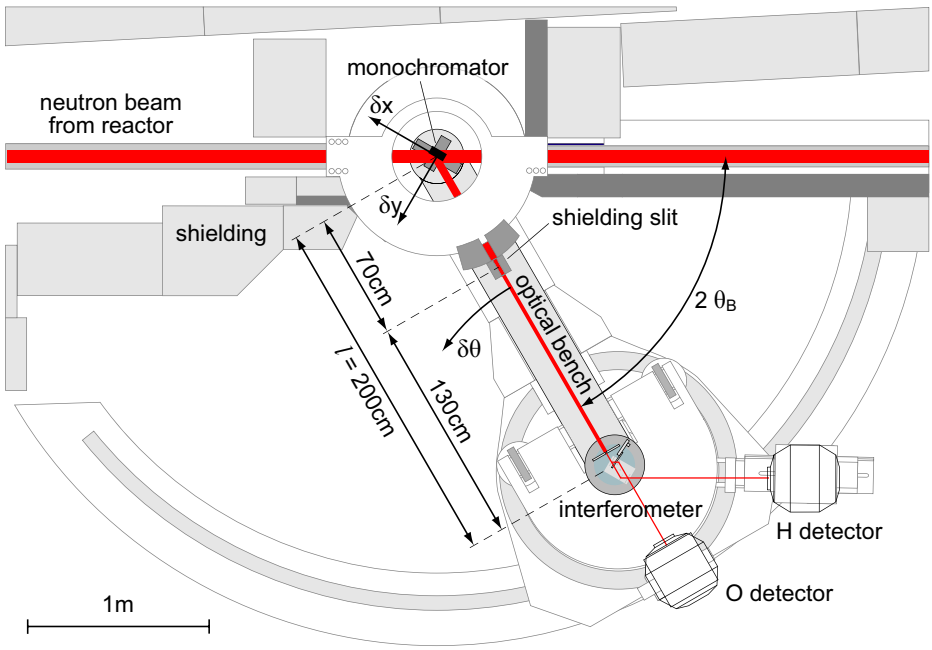

Figure 4.18: The interferometer setup S18 at the ILL.

θ_B [°]	29.66	29.77	29.9	30.0	30.1	mean
phase shift pos. Ia [°]	−5.09	−6.53	−8.24	−7.24	−4.75	−6.43
statistical error	±0.73	±0.55	±0.63	±0.57	±0.93	±0.27
total error	(±0.55)	(±0.5)	(±0.48)	(±1.1)	(±1.1)	(±0.36)
phase shift pos. IIb [°]	0.25	0.08	0.95	−1.57	0.7	−0.04
statistical error	±0.86	±0.67	±0.79	±0.74	±1.1	±0.33
total error	(±1.1)	(±0.86)	(±1.1)	(±0.73)	(±1.4)	(±0.4)
contrast[1)] pos. Ia (O beam)	9.1%	7.0%	5.5%	6.5%	9.0%	
contrast[1)] pos. IIb (H beam)	5.9%	4.1%	3.2%	3.6%	6.0%	
W contrast[2)] pos Ia (O+H)	48%	22%	20%	31%	57%	
W contrast[2)] pos IIb (H)	75%	48%	25%	48%	72%	
intensity[3)]	3780	8630	10750	8200	2272	
number of measurements	8	11	10	13	8	

Table 4.1: Results of the measurements at different Bragg angles.
[1)] visibility of the interference oscillations, [2)] visibility of the alignment peak,
[3)] counts per 10s in O+H without channel stack.

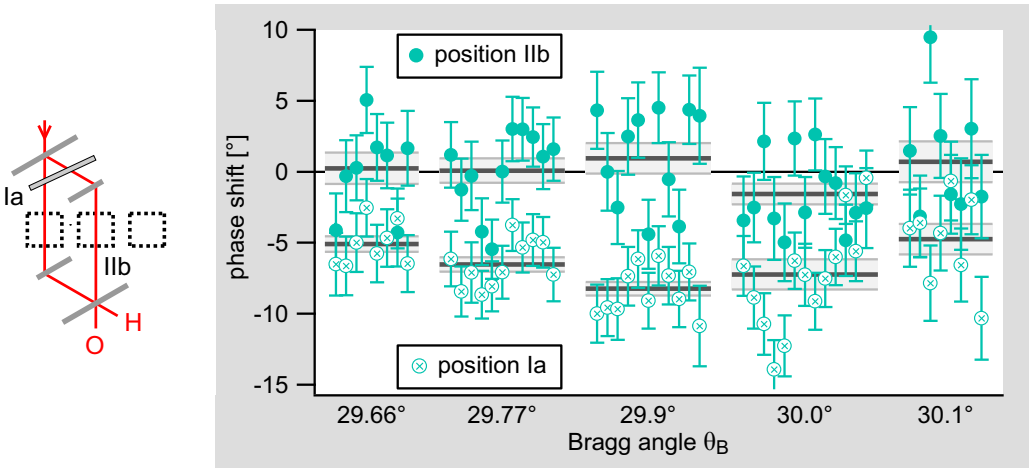

Figure 4.19: The 2-cm sample in the skew symmetric interferometer. Interferometer and monochromator have been turned slightly to different bragg angles.

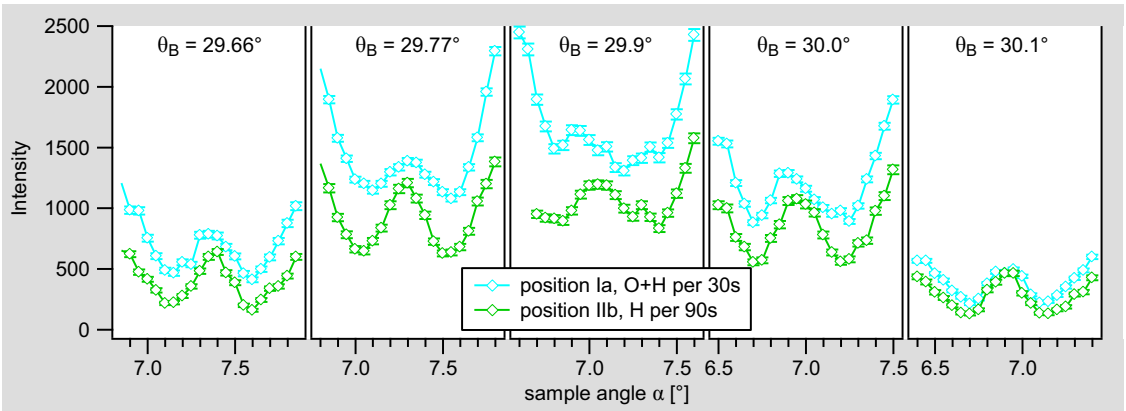

Figure 4.20: Alignment scans at different Bragg angles, indicating a change of the beam divergence which the Bragg angle.

curve, see section 5.6, figure 5.9.

The whole ILL setup is sketched in figure 4.18. Usually the Bragg angle is changed by rotating the whole optical bench around the monochromator axis. This rotation is quite complicated and it is designed for coarse rotation (e.g. switch between 30° and 45°) but not for precision adjustments. Therefore I decided to keep the optical bench fixed and just rotate the interferometer and adjust the monochromator accordingly. A change of the Bragg angle by $\delta\theta = 0.1°$ requires a

- rotation of the interferometer by $2\delta\theta = 0.2°$
- rotation of the monochromator by $\delta\theta = 0.1°$.
- translation of the monochromator parallel to the Bragg planes by $\delta x = l \sin\delta\theta \ \cos 2\theta_B / \sin(2\theta_B - \delta\theta) = 7\text{mm}$
- translation of the monochromator perpendicular to the Bragg planes by $\delta y = l \sin\delta\theta \ \sin 2\theta_B / \sin(2\theta_B - \delta\theta) = 4\text{mm}$

The phase shift has been measured a couple of times at the center of the alignment peak for five different Bragg angles. The results are given in table 4.1 and figure 4.19. The phase shift in position Ia shows a Bragg dependency to some extent. Unfortunately the beam divergence has not been kept constant, which can be clearly seen at the intensity and contrast values given in the table and in the alignment scans, figure 4.20. The slit in the shielding (figure 4.18) should have been moved too, along with the monochromator. So we cannot tell if the modulation of the phase shift was caused by the Bragg angle or the beam divergence.

4.7 Conclusion

The measurements clearly show that the phase shift

1. is up to ten times larger then explicable by the confinement,
2. depends on the position within the interferometer,
3. depends on the sample angle in a way that cannot be explained as a linear wave length dependency,
4. may be sensible to changes of the Bragg angle or the beam divergence.

It follows from point 2 that the plane wave theory of the interferometer is not sufficient in this situation. Only the spherical theory describes the differences of the wave fields in the four different positions within the interferometer. The plane wave theory (chapter 5) was implicitly used in chapter 2 for the calculation of the phase shift.

In addition, only the spherical theory can handle the wave components diffracted by the channels. Although the diffraction was calculated in section 2.3, it could not be taken into account for the phase shift, as the plane wave theory was used. The spherical theory is presented in chapter 6.

Chapter 5

Plane Wave Theory of the Interferometer

The plane wave theory is the basic theory for the description of neutron interferometers. A neutron interferometer (of triple Laue type) consists of three perfect crystal blades. The first blade (Splitter) splits the incident beam into two beam paths. These beams are reflected by the second blade (Mirror) and recombined by the third blade (Analyzer). The two beams leaving the Analyzer are called O- and H-beam. Depending on the phase shift between beam path I and II the intensity oscillates between the O- and the H-beam. In a skew symmetric interferometer the Mirror blade is cut in two to allow more space for samples. However this makes no difference in the theory.

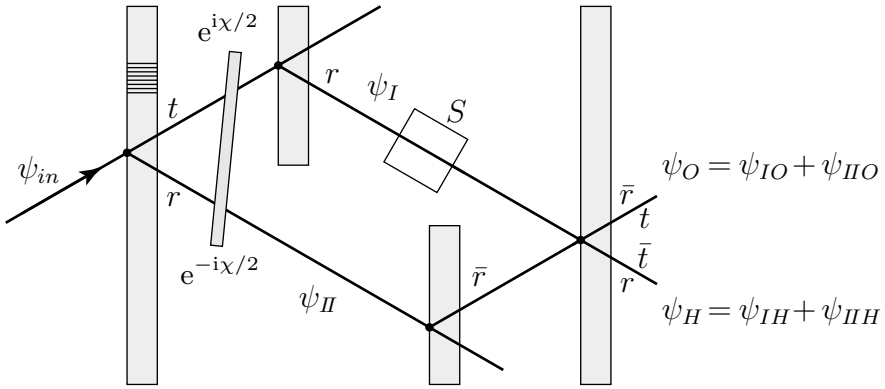

Figure 5.1: Sketch of a neutron interferometer.

The plane wave theory of the neutron interferometer calculates the transmission and reflection amplitudes of a plane wave falling onto the crystal blades and passing the whole interferometer. The crystal blades are described by the dynamical theory of diffraction. The plane wave theory can handle different wave lengths and/or incident angles (also off-Bragg) but assumes that the different components are not mixed up. Each component is treated independently from the others. No localized wave function is calculated.

We will see, that if the interferometer is well focused and if the sample can be described by a simple complex factor, then the interferometric results (phase shift and contrast) are independent from the exact angle of the incident wave.

In order to calculate the wave functions of the O- and H-beam we will take a plane wave as ψ_{in} and start on the left in figure 5.1. We will follow the beam paths and accumulate all contributions of the crystal blades, the phase shifter and the sample.

5.1 Single Crystal Blade

The neutron wave function in a perfect crystal blade is described in detail by the theory of dynamical diffraction which solves the time independent Schrödinger equation on the periodic crystal potential [RP74], [BBG76]. Here I only summarize the results which are important for neutron interferometry, which means that the following restrictions apply:

- The wave functions inside the crystals are omitted. Only the transmitted and reflected wave functions behind the crystals are calculated.
- Symmetrical Laue geometry is assumed, which means that the crystal planes are perpendicular to the surface of the blade.
- The plane wave theory is used, which means that the incident beam is considered a plane wave. In chapter 6 a superposition of many plane waves will be used to form a localized beam.

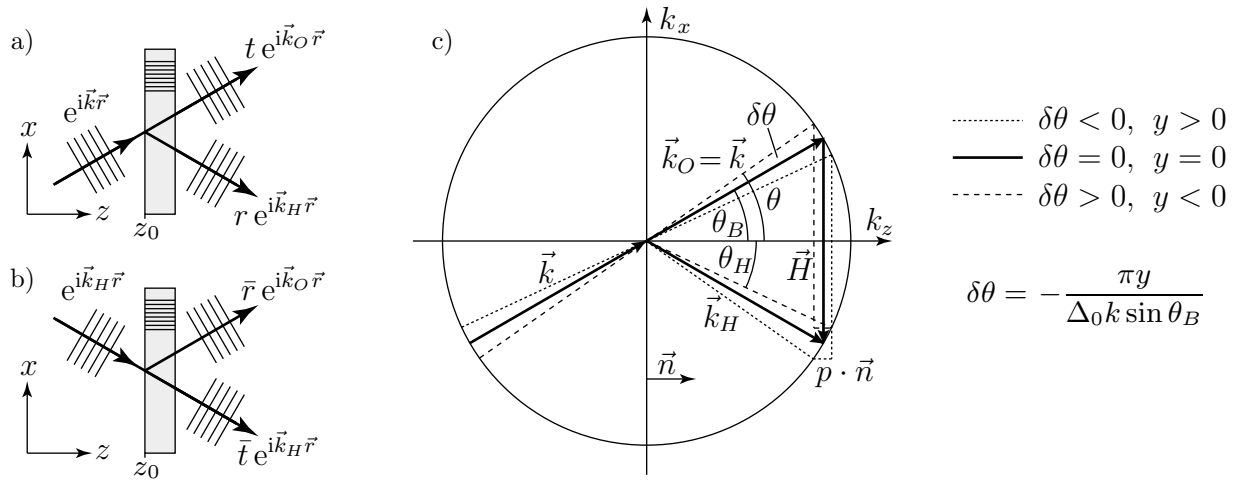

Figure 5.2: Transmission and reflection at a single beam splitter (a,b); illustration of the wave vectors for $\delta\theta \neq 0$ (c).

As illustrated in figure 5.2a let $\vec{k}$ be the wave vector of the incident plane wave $\psi_{in} = \exp(i\vec{k}\vec{r})$ with the incident angle θ. Let θ deviate from the exact Bragg angle by a small amount $\delta\theta$.

$$\theta = \theta_B + \delta\theta \tag{5.1}$$

Then the amplitudes and directions of the transmitted wave ψ_O and the reflected wave ψ_H follow from the dynamical theory of diffraction:

$$\psi_O = t(y)\,\mathrm{e}^{\mathrm{i}\vec{k}_O\vec{r}} \qquad t(y) = \mathrm{e}^{-\mathrm{i}A}\,\mathrm{e}^{-\mathrm{i}Ay}\left\{\cos\left(A\sqrt{1+y^2}\right) + \mathrm{i}\,y\,\frac{1}{\sqrt{1+y^2}}\sin\left(A\sqrt{1+y^2}\right)\right\} \tag{5.2}$$

$$\psi_H = r(y)\,\mathrm{e}^{\mathrm{i}\vec{k}_H\vec{r}} \qquad r(y) = \mathrm{e}^{-\mathrm{i}A}\,\mathrm{e}^{+\mathrm{i}Ay}\;\mathrm{e}^{\mathrm{i}yz_0 2\pi/\Delta_0}\left\{\quad -\mathrm{i}\;\frac{1}{\sqrt{1+y^2}}\sin\left(A\sqrt{1+y^2}\right)\right\} \tag{5.3}$$

$$A = \frac{\pi D}{\Delta_0}, \qquad D = \text{thickness of crystal blade} \tag{5.4}$$

$$\Delta_0 = \frac{\pi V_c \cos\theta_B}{b_c|F|\lambda} = \text{Pendellösung length} \tag{5.5}$$

$$z_0 = z \text{ position of the front surface of the crystal} \tag{5.6}$$

y is a dimensionless parameterization of the Bragg deviation $\delta\theta$. (In literature the minus sign is sometimes put into $\delta\theta$.)

$$y = -\frac{\delta\theta\,\sin 2\theta_B}{V_0/E_{in}} = -\frac{k^2\delta\theta\,\sin 2\theta_B}{4\pi b_c N} = -\frac{k\Delta_0\,\delta\theta\,\sin\theta_B}{\pi} \tag{5.7}$$

The material constants are summarized in table (5.1).

The reflected wavevector is given as

$$\vec{k}_H = \vec{k} + \vec{H} + p\,\vec{n} \tag{5.8}$$

$$H = 2\pi/d = 2k\sin\theta_B \qquad \text{reciprocal vector of reflecting planes} \tag{5.9}$$

$$p = 2\pi y/\Delta_0 = -2k\sin\theta_B\,\delta\theta \qquad \text{correction vector perpendicular to the surface} \tag{5.10}$$

and is illustrated in figure 5.2c. $\vec{H}$ is the reciprocal vector of the reflecting planes and describes the Bragg reflection. p is a correction term perpendicular to the surface and ensures that the absolute value of $\vec{k}$ is conserved. The reflection shows a non-specular behaviour for $\delta\theta \neq 0$ as indicated with the dotted and dashed lines. If the incident angle θ is larger than θ_B then the reflected angle θ_H is smaller than θ_B and vice versa.

$$\vec{k} \equiv \vec{k}_O = \begin{pmatrix} k_{Ox} \\ k_{Oz} \end{pmatrix} = k\begin{pmatrix} \sin(\theta_B+\delta\theta) \\ \cos(\theta_B+\delta\theta) \end{pmatrix} \approx k\begin{pmatrix} \sin\theta_B + \delta\theta\,\cos\theta_B \\ \cos\theta_B - \delta\theta\,\sin\theta_B \end{pmatrix} \tag{5.11}$$

$$\vec{k}_H = \begin{pmatrix} k_{Hx} \\ k_{Hz} \end{pmatrix} = \vec{k}_O + \underbrace{2k\sin\theta_B\begin{pmatrix} -1 \\ \delta\theta \end{pmatrix}}_{\Delta\vec{k}} \approx k\begin{pmatrix} -\sin\theta_B + \delta\theta\,\cos\theta_B \\ \cos\theta_B + \delta\theta\,\sin\theta_B \end{pmatrix} \tag{5.12}$$

$$\Delta\vec{k} = \begin{pmatrix} \Delta k_x \\ \Delta k_z \end{pmatrix} = 2k\sin\theta_B\begin{pmatrix} -1 \\ \delta\theta \end{pmatrix} \qquad = \begin{pmatrix} -2k\sin\theta_B \\ -2\pi y/\Delta_0 \end{pmatrix} \tag{5.13}$$

The neutron wave length is typically in the range of 1.9 to 2.7 Å which corresponds to energies of 22 to 11 meV and bragg angles of 30° to 45°.

b_c	coherent neutron scattering length	$b_{cSi} = 4.1507\ 10^{-15}\,\mathrm{m}$
a	lattice constant	$a_{Si} = 5.43101993\ 10^{-10}\,\mathrm{m}$
V_c	volume of crystal elementary cell	$V_{cSi} = a_{Si}^3$
N	density of crystal atoms	$N_{Si} = 8/V_{cSi}$
d	distance of Bragg planes	$d_{Sihkl} = a_{Si}/\sqrt{h^2+k^2+l^2}$
F	structure factor	$F_{Si220} = 8,\ F_{Si111} = 4\,(1 \pm \mathrm{i})$
$V_0 = N b_c 2\pi\hbar^2/m$	optical potential	$V_{0Si} = 53.9751\,\mathrm{neV}$
Δ_0	Pendellösung length	$\Delta_0 = \begin{cases} 68\mu\mathrm{m} & Si220, \lambda = 1.9\text{Å} \\ 39\mu\mathrm{m} & Si220, \lambda = 2.7\text{Å} \\ 71\mu\mathrm{m} & Si111, \lambda = 2.7\text{Å} \end{cases}$
m	neutron mass	$m = 1.6749286\ 10^{-27}\,\mathrm{kg}$
$\hbar$	Planck's constant	$\hbar = 1.05457266\ 10^{-34}\,\mathrm{Js}$
e	elementary charge	$e = 1.60217733\ 10^{-19}\,\mathrm{C}$

Table 5.1: Fundamental and material constants

5.2 The Whole Interferometer

If we apply the formulas (5.2) and (5.3) also to the second and third interferometer blade, the incident wave may also be in $\vec{k}_H$ direction, as shown in figure 5.2b. In this case we have to replace $t(y)$ and $r(y)$ by $t(-y)$ and $r(-y)$. This is a consequence of the non-specular reflection. We will use the short notation

$$t = t(y) \qquad \bar{t} = t(-y) \qquad r = r(y) \qquad \bar{r} = r(-y) \tag{5.14}$$

(Please note: The vector $\vec{r}$ denotes a point in space whereas the complex scalars r and $\bar{r}$ denote the reflection factors.)

The factors t and r also depend on the z position of the crystal and on the crystal thickness D. For the general case we assume different thicknesses for each blade and we will mark r, t, D, etc. with the subscripts $j \in \{S, M\mathrm{I}, M\mathrm{II}, A\}$ to distinguish the splitter, mirror and analyzer blades, see figure 5.3. For the subsequent calculation we will split up r and t in the following way:

$$t_j = \tau_j\ \mathrm{e}^{-\mathrm{i}yA_j} \qquad \tau_j = \mathrm{e}^{-\mathrm{i}A_j}\left\{\cos\!\left(A_j\sqrt{1+y^2}\right) + \mathrm{i}\,y\,\frac{\sin\!\left(A_j\sqrt{1+y^2}\right)}{\sqrt{1+y^2}}\right\} \tag{5.15}$$

$$\bar{t}_j = \tau_j^*\ \mathrm{e}^{+\mathrm{i}yA_j} \tag{5.16}$$

$$r_j = \rho_j\ \mathrm{e}^{+\mathrm{i}yA_j}\ \mathrm{e}^{\mathrm{i}yz_j 2\pi/\Delta_0} \qquad \rho_j = \mathrm{e}^{-\mathrm{i}A_j}\left\{-\mathrm{i}\ \frac{\sin\!\left(A_j\sqrt{1+y^2}\right)}{\sqrt{1+y^2}}\right\} \tag{5.17}$$

$$\bar{r}_j = \rho_j\ \mathrm{e}^{-\mathrm{i}yA_j}\ \mathrm{e}^{-\mathrm{i}yz_j 2\pi/\Delta_0} \tag{5.18}$$

Now we can follow the beam paths as indicated in figure 5.3 and collect all factors. Behind the first blade we get for the transmitted wave function $\psi_{\mathrm{I}a} = \exp(\mathrm{i}\vec{k}_O\vec{r})\exp(-\mathrm{i}yA_S)\tau_S$. This is

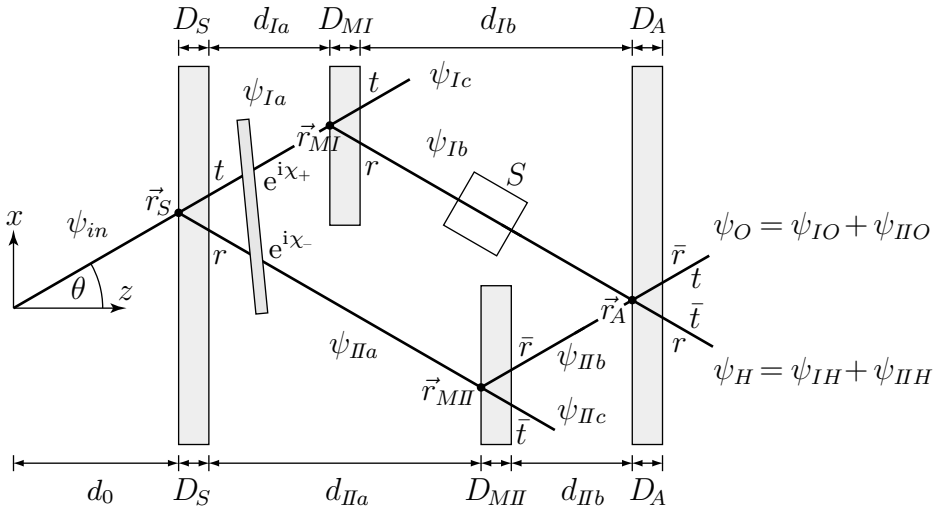

Figure 5.3: Calculating the wave functions.

again a plane wave now falling onto the mirror blade. Applying the reflection formula (5.3) with (5.17) we get behinde the mirror $\psi_{\mathrm{I}b} = \exp(\mathrm{i}\vec{k}_H\vec{r})\exp(-\mathrm{i}yA_S)\tau_S\rho_{M\mathrm{I}}\exp(+\mathrm{i}yA_{M\mathrm{I}})\exp(\mathrm{i}yz_{M\mathrm{I}}\frac{2\pi}{\Delta_0})$. With $z_{M\mathrm{I}} = d_0 + D_S + d_{\mathrm{I}a}$ we get $\psi_{\mathrm{I}b} = \exp(\mathrm{i}\vec{k}_H\vec{r})\tau_S\rho_{M\mathrm{I}}\exp(\mathrm{i}y(A_S+A_{M\mathrm{I}}))\exp(\mathrm{i}y(d_0+d_{\mathrm{I}a})\frac{2\pi}{\Delta_0})$. The wave functions in the other regions are calculated in a similar way and are summarized below.

$$\psi_{in} = \exp\big(\mathrm{i}\vec{k}_O\vec{r}\big) \tag{5.19}$$
$$\psi_{\mathrm{I}a} = \exp\big(\mathrm{i}\vec{k}_O\vec{r}\big)\,\tau_S\exp\big(-\mathrm{i}\tfrac{y\pi}{\Delta_0}D_S\big) \tag{5.20}$$
$$\psi_{\mathrm{II}a} = \exp\big(\mathrm{i}\vec{k}_H\vec{r}\big)\,\rho_S\exp\big(+\mathrm{i}\tfrac{y\pi}{\Delta_0}(D_S+2d_0)\big) \tag{5.21}$$
$$\psi_{\mathrm{I}a} = \exp\big(\mathrm{i}\vec{k}_H\vec{r}\big)\,\tau_S\;\rho_{M\mathrm{I}}\;\exp\big(+\mathrm{i}\tfrac{y\pi}{\Delta_0}(D_S+D_{M\mathrm{I}}+2d_{\mathrm{I}a}+2d_0)\big) \tag{5.22}$$
$$\psi_{\mathrm{II}b} = \exp\big(\mathrm{i}\vec{k}_O\vec{r}\big)\,\rho_S\,\rho_{M\mathrm{II}}\exp\big(-\mathrm{i}\tfrac{y\pi}{\Delta_0}(D_S+D_{M\mathrm{II}}+2d_{\mathrm{II}a})\big) \tag{5.23}$$
$$\psi_{\mathrm{I}c} = \exp\big(\mathrm{i}\vec{k}_O\vec{r}\big)\,\tau_S\;\tau_{M\mathrm{I}}\;\exp\big(-\mathrm{i}\tfrac{y\pi}{\Delta_0}(D_S+D_{M\mathrm{I}})\big) \tag{5.24}$$
$$\psi_{\mathrm{II}c} = \exp\big(\mathrm{i}\vec{k}_H\vec{r}\big)\,\rho_S\,\tau^*_{M\mathrm{II}}\exp\big(+\mathrm{i}\tfrac{y\pi}{\Delta_0}(D_S+D_{M\mathrm{II}}+2d_0)\big) \tag{5.25}$$
$$\psi_{\mathrm{I}O} = \exp\big(\mathrm{i}\vec{k}_O\vec{r}\big)\;\tau_S\;\rho_{M\mathrm{I}}\,\rho_A\exp\big(-\mathrm{i}\tfrac{y\pi}{\Delta_0}(D_S+D_{M\mathrm{I}}+D_A+2d_{\mathrm{I}b})\big) \tag{5.26}$$
$$\psi_{\mathrm{II}O} = \exp\big(\mathrm{i}\vec{k}_O\vec{r}\big)\,\rho_S\,\rho_{M\mathrm{II}}\,\tau_A\exp\big(-\mathrm{i}\tfrac{y\pi}{\Delta_0}(D_S+D_{M\mathrm{II}}+D_A+2d_{\mathrm{II}a})\big) \tag{5.27}$$
$$\psi_{\mathrm{I}H} = \exp\big(\mathrm{i}\vec{k}_H\vec{r}\big)\;\tau_S\;\rho_{M\mathrm{I}}\,\tau^*_A\;\exp\big(+\mathrm{i}\tfrac{y\pi}{\Delta_0}(D_S+D_{M\mathrm{I}}+D_A+2d_{\mathrm{I}a}+2d_0)\big) \tag{5.28}$$
$$\psi_{\mathrm{II}H} = \exp\big(\mathrm{i}\vec{k}_H\vec{r}\big)\,\rho_S\,\rho_{M\mathrm{II}}\rho_A\exp\big(+\mathrm{i}\tfrac{y\pi}{\Delta_0}(D_S+D_{M\mathrm{II}}+D_A+2d_{\mathrm{II}b}+2d_0)\big) \tag{5.29}$$

The final wavefunctions in the O and H beam are the superpositions of both path contributions, $\psi_O = \psi_{\mathrm{I}O} + \psi_{\mathrm{II}O}$ and $\psi_H = \psi_{\mathrm{I}H} + \psi_{\mathrm{II}H}$. Comparing (5.26) and (5.27) one can derive the focus conditions for fully constructive interference in the O beam:

$$D_S = D_A \qquad D_{M\mathrm{I}} = D_{M\mathrm{II}} \qquad d_{\mathrm{I}b} = d_{\mathrm{II}a} \tag{5.30}$$

5.3 Interferometer plus Sample

In a standard interferometer experiment we have a phase shifter and a sample. The phase shifter adds the phase $\exp(\mathrm{i}\chi_\pm)$ to each beam. See section 5.5 for details. The sample just contributes with the complex factor S as long as it doesn't change the beam direction.

$$\psi_O = S\,\mathrm{e}^{\mathrm{i}\chi_+}\psi_{\mathrm{I}O} + \mathrm{e}^{\mathrm{i}\chi_-}\psi_{\mathrm{II}O} \tag{5.31}$$

$$\psi_H = S\,\mathrm{e}^{\mathrm{i}\chi_+}\psi_{\mathrm{I}H} + \mathrm{e}^{\mathrm{i}\chi_-}\psi_{\mathrm{II}H} \tag{5.32}$$

If the focus conditions (5.30) are fullfilled $\psi_{\mathrm{I}O}$ and $\psi_{\mathrm{II}O}$ are equal and we get with $\chi := \chi_+ - \chi_-$

$$\psi_O \propto \big(S\ \exp(\mathrm{i}\chi) + 1\big) \tag{5.33}$$

$$\psi_H \propto \big(|\tau_S|^2\ S\ \exp(\mathrm{i}\chi) + \rho_S^2\big). \tag{5.34}$$

The intensity measured in the O beam is

$$|\psi_O|^2 \ \propto\ \frac{2|S|}{|S|^2+1}\cos(\chi + \arg S) + 1. \tag{5.35}$$

The phase shift $\arg S$ of the sample can be directly probed by the phase shifter χ. The absolute value of the sample factor $|S|$ is smaller than one in case of absorption and equal to one in case of no absorption by the sample. It influences the contrast or visibility of the oscillations:

$$V = 2|S|/(|S|^2+1) \tag{5.36}$$

In real experiments the contrast will always be smaller because of interferometer imperfections.

5.4 Coherent and Incoherent Superposition

The neutron beam has a macroscopic diameter (cm) but a microscopic transverse coherence length (μm). This means that the beam is an incoherent superposition of small wave packets. Which phase shift do we observe, if a sample has different phase factors S_j depending on the beam trajectory? All trajectories within the transverse coherence length have to be averaged coherently. Trajectories which are further apart have to be averaged incoherently.

• Recapitulation of the pure state:

$$\text{reference beam:}\quad \psi_I = \mathrm{e}^{\mathrm{i}kr} \tag{5.37}$$

$$\text{sample beam:}\quad \psi_{II} = \mathrm{e}^{\mathrm{i}kr}\,S, \qquad S = a\,\mathrm{e}^{\mathrm{i}\varphi} \tag{5.38}$$

$$\text{intensity:}\quad I = |\psi_I + \mathrm{e}^{\mathrm{i}\chi}\psi_{II}|^2 = |1 + \mathrm{e}^{\mathrm{i}\chi}S|^2 = 1 + a^2 + 2a\cos(\varphi+\chi) \tag{5.39}$$

$$\text{phase shift:}\quad \Phi = \arg S = \varphi \tag{5.40}$$

$$\text{visibility:}\quad V = \frac{2a}{1+a^2} = \frac{2\,|S|}{1+|S|^2} \tag{5.41}$$

• Coherent Superposition:

$$\psi_{II} = \textstyle\sum_j \psi_{IIj} = \mathrm{e}^{\mathrm{i}kr}\sum_j S_j \tag{5.42}$$

$$\Phi = \arg\textstyle\sum_j S_j \tag{5.43}$$

$$V = \frac{2\left|\sum_j S_j\right|}{1+\left|\sum_j S_j\right|^2} \tag{5.44}$$

• Incoherent Superposition:

$$I = \sum_j I_j = \sum_j \left(1 + a_j^2 + 2a_j \cos(\varphi_j + \chi)\right) \tag{5.45}$$

$$= \sum_j (1 + a_j^2) + 2\sum_j (a_j \cos\varphi_j \sin\chi + a_j \sin\varphi_j \cos\chi) \tag{5.46}$$

$$= \sum_j (1 + |S_j|^2) + 2\sum_j \mathrm{Re}S_j \sin\chi + 2\sum_j \mathrm{Im}S_j \cos\chi \tag{5.47}$$

$$= \underbrace{\left(\sum_j (1 + |S_j|^2)\right)}_{} \cdot \left(1 + \underbrace{\frac{2\,\mathrm{Re}\sum_j S_j}{\sum_j (1 + |S_j|^2)}}_{} \sin\chi + \underbrace{\frac{2\,\mathrm{Im}\sum_j S_j}{\sum_j (1 + |S_j|^2)}}_{} \cos\chi\right) \tag{5.48}$$

$$= \quad A \quad \cdot (\, 1 + \quad C\cos\Phi \quad \sin\chi + \quad C\sin\Phi \quad \cos\chi\,) \tag{5.49}$$

$$\Phi \equiv \arctan\frac{C\sin\Phi}{C\cos\Phi} = \arctan\frac{\mathrm{Im}\sum_j S_j}{\mathrm{Re}\sum_j S_j} = \arg\sum_j S_j \tag{5.50}$$

$$V \equiv \sqrt{C^2\cos^2\Phi + C^2\sin^2\Phi} = \frac{2\sqrt{(\mathrm{Re}\sum_j S_j)^2 + (\mathrm{Im}\sum_j S_j)^2}}{\sum_j (1 + |S_j|^2)} = \frac{2\left|\sum_j S_j\right|}{\sum_j (1 + |S_j|^2)} \tag{5.51}$$

The phase shifts are the same in both cases, (5.43) and (5.50). There is only a difference in the contrast. The difference depends on the actual distribution of S_j.

5.5 The Phase Shifter

The phase shifter is usually made of aluminum, sapphire or silicon in non Bragg condition. Its optical properties are described by the index of refraction $n = K/k = \sqrt{1 - V_0/E}$ which describes the ratio of the wave vector inside (K) and outside (k) of the material. The refraction of a plane wave k entering the phase shifter with an angle φ is shown in figure 5.4a and is described by the formulas

$$k_\parallel = k\sin\varphi \qquad K_\parallel = K\sin\Phi \qquad K_\parallel = k_\parallel \tag{5.52}$$

$$k_\perp = k\cos\varphi \qquad K_\perp = K\cos\Phi \qquad K_\perp = \sqrt{K^2 - K_\parallel^2} = \sqrt{n^2k^2 - k_\parallel^2} = k\sqrt{n^2 - \sin^2\varphi} \tag{5.53}$$

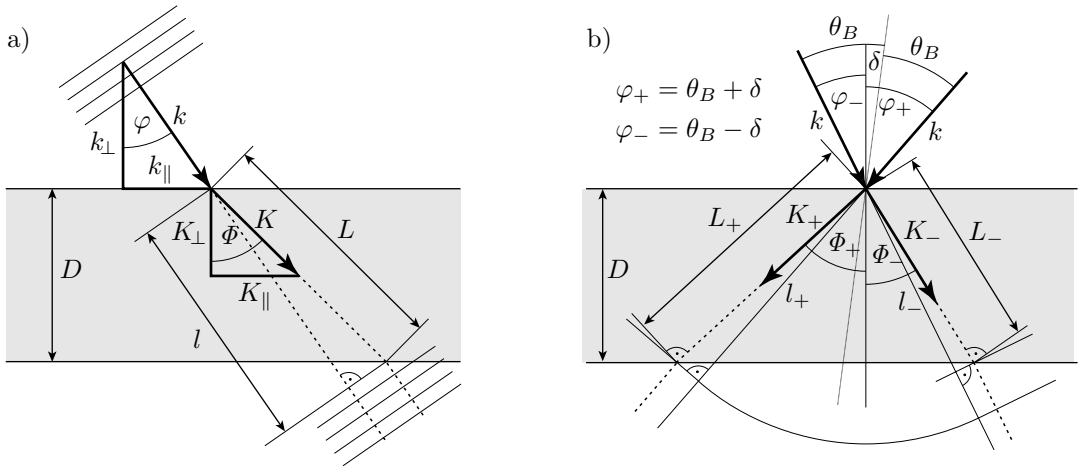

Figure 5.4: Phase Shifter

Comparing the phase of the transmitted plane wave with the phase without phase shifter we get the phase shift $\chi_0 = KL - kl$. With $L = D/\cos\Phi = DK/K_\perp$ and $l = L\cos(\Phi - \varphi) = L(K_\perp k_\perp + K_\parallel k_\parallel)/(Kk)$ we get:

$$\chi_0 = KL - kl = \frac{D}{K_\perp}\left(K^2 - K_\perp k_\perp - K_\parallel k_\parallel\right) = D\left(K_\perp - k_\perp\right) = Dk\left(\sqrt{n^2 - \sin^2\varphi} - \cos\varphi\right) \quad (5.54)$$

The neutron index of refraction is very close to one, e.g. in silicon $(n_{\mathrm{Si}} - 1) = -0.97 \cdot 10^{-6}$. A series expansion leads to

$$\chi_0 = Dk\left(\frac{n-1}{\cos\varphi} + \mathcal{O}(n-1)^2\right) \approx Dk\frac{n-1}{\cos\varphi}\,. \quad (5.55)$$

The phase shifter in a neutron interferometer intersects both beam paths which enclose the angle $2\theta_B$ as illustrated in figure 5.4b. If the phase shifter is parallel to the interferometer blade both beams enter the phase shifter with the same angle $\varphi = \theta_B$. If the phase shifter is rotated by a small angle δ we get $\varphi_\pm = \theta_B \pm \delta$ and the phase shift between the two beams results in

$$\chi = \chi_+ - \chi_- = D_0 k(n-1)\left(\frac{1}{\cos(\theta_B + \delta)} - \frac{1}{\cos(\theta_B - \delta)}\right). \quad (5.56)$$

5.6 Discussion of the Laue Reflection

The reflection curve $|r|^2$ (5.3) of a single crystal blade is shown in figure 5.5 by the green curve. It consists of a Lorentzian envelope $\frac{1}{1+y^2}$ and an oscillation $\sin^2(A\sqrt{1+y^2})$. The transmission curve would be the complement to one. The O beam intensity is shown by the blue curve. It consists of two reflections and one transmission. At positions with maximum reflection the transmission becomes a minimum and therefore the O beam intensity shows a minimum as well.

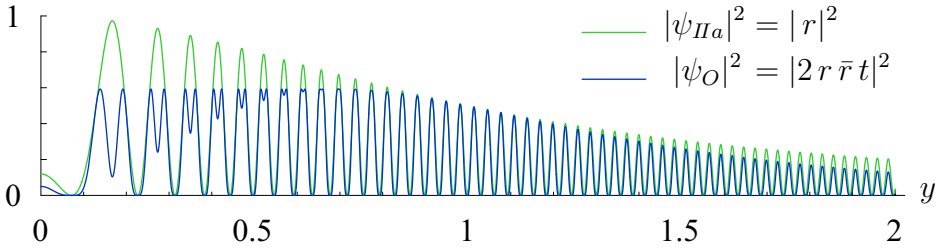

Figure 5.5: y dependance of the intensity behind the first and the third interferometer blade.

The intensity at $y = 0$ depends on the crystal thickness and on the selected wavelength or Bragg angle as illustrated in figure 5.6. The wavelength and the Bragg angle are coupled by Bragg's law $\lambda = 2d\sin\theta_B$. Moving along this line we get a slow intensity oscillation for $y = 0$. Moving perpendicular to this line means violating Bragg's law, $y \neq 0$ and we get the fast oscillations shown in figure 5.5. In order to show both oscillations in a single plot we chose a coordinate system where the axes of λ and θ are no longer perpendicular. A very strong distortion as shown on the right of figure 5.6 leads to figure 5.7 where the axes λ and θ already seem to be parallel (which is nevertheless not the case). Figure 5.8 shows the same as figure 5.7 but for the NIST parameters. Figure 5.9 shows the O beam intensity and its integration over $\delta\theta$. If the beam divergence is small enough, an intensity modulation of $\pm 7\%$ should be observable when changing the Bragg angle.

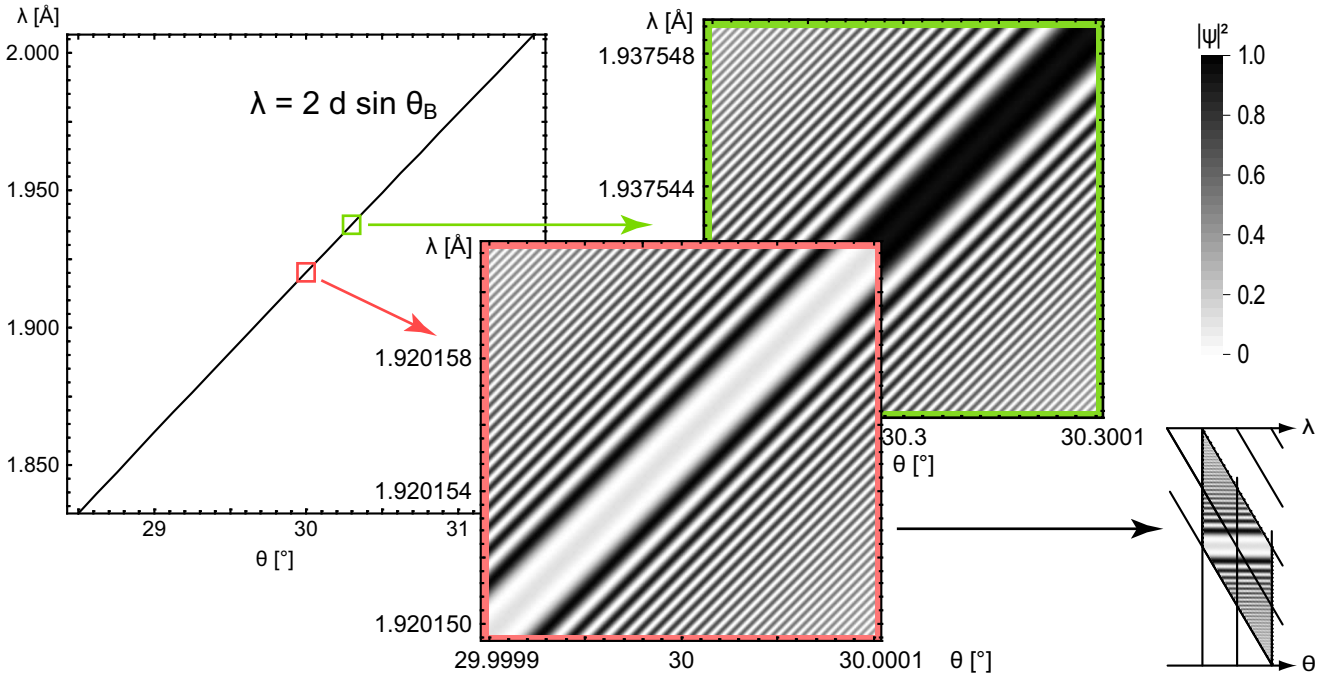

Figure 5.6: Bragg's law and two blow-ups showing the intensity of a single Laue reflection on a 3mm thick silicon blade. The distortion shown by the small figure on the right leads to figure 5.7 showing the oscillations over a wide range of λ and θ in a single plot.

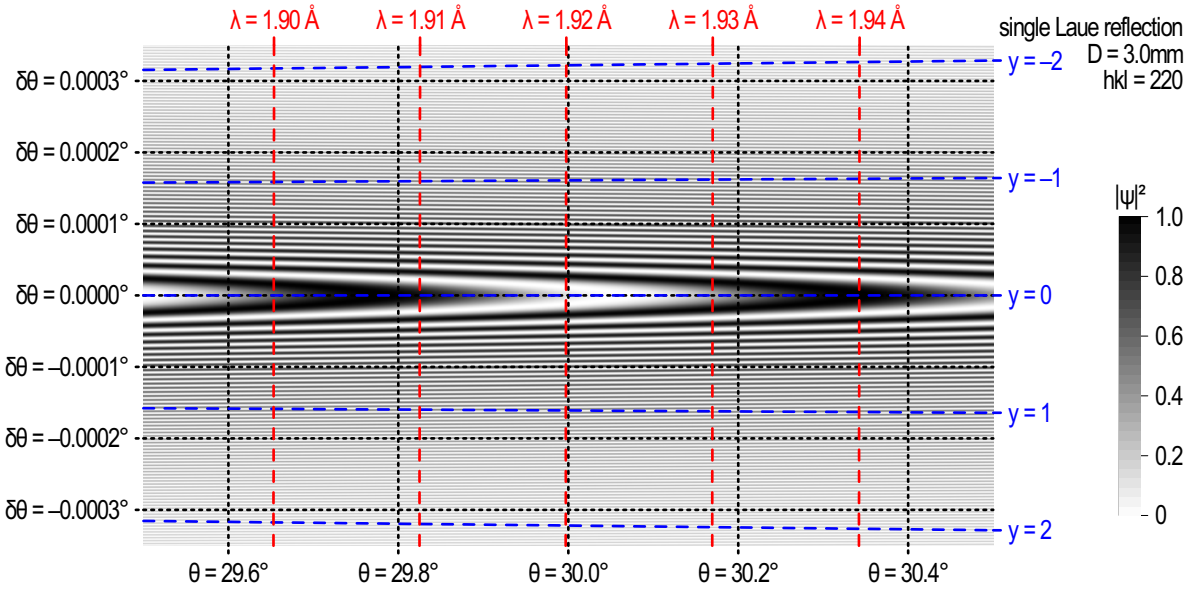

Figure 5.7: Intensity of a single Laue reflection on a 3mm thick silicon blade with $hkl = 220$. The lines of constant λ and θ just seem to be parallel as a consequence of the strong distortion shown in figure 5.6.

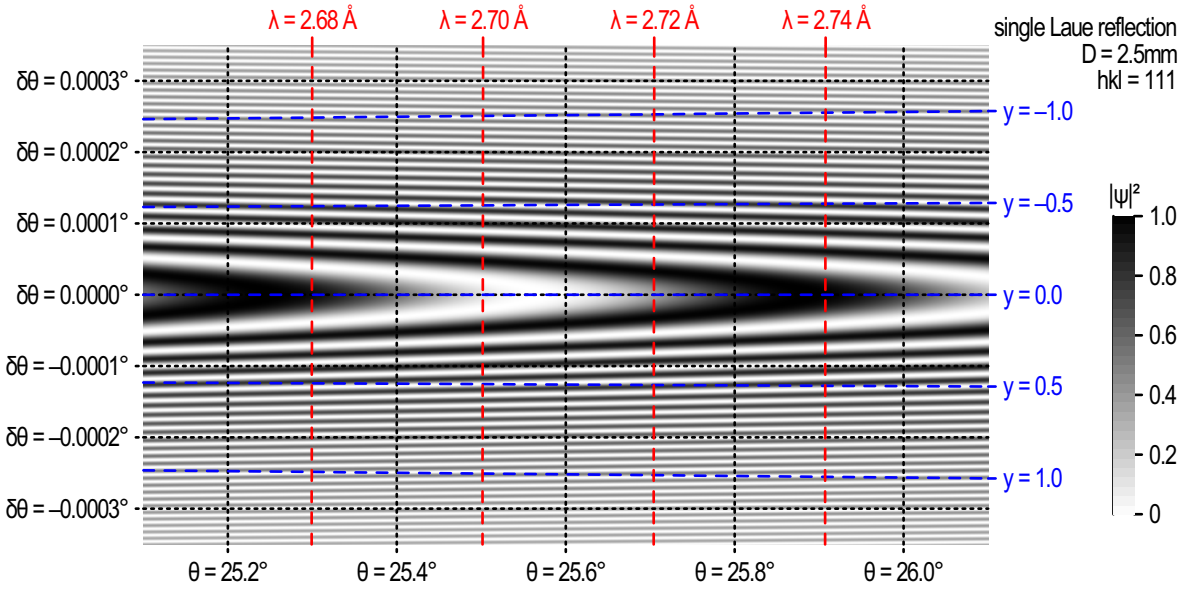

Figure 5.8: Intensity of a single Laue reflection on a 2.5mm thick silicon blade with $hkl = 111$ which was used at the NIST setup. The oscillations are wider in both directions.

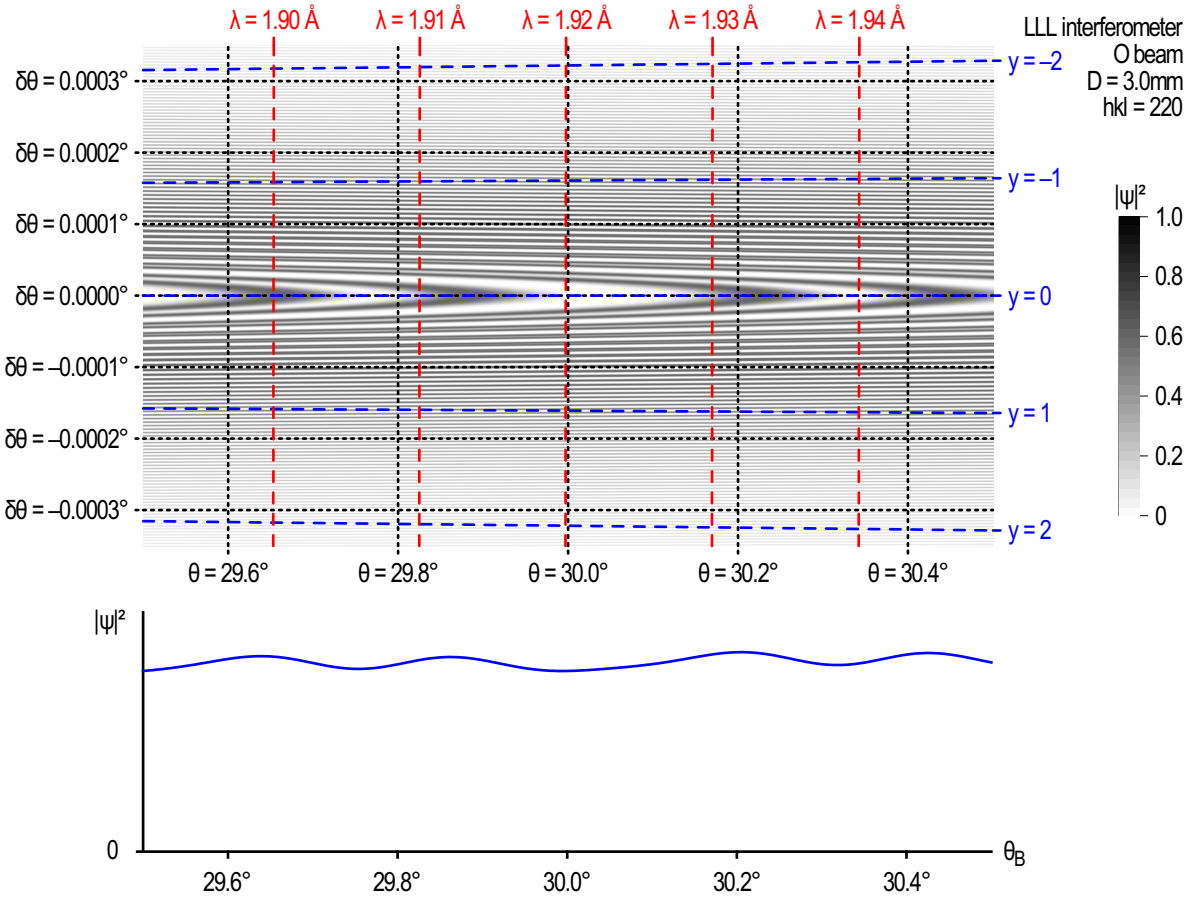

Figure 5.9: Top: O beam intensity of a triple Laue interferometer. Bottom: intensity integrated over $\delta\theta$. The integrated intensity oscillates with an amplitude of 7%.

5.7 Fluctuations of the Blade Thickness

Let all eight crystal surfaces fluctuate in z direction by small amounts $\Delta_{...}$.

$$D_S \to D_S - \Delta_{S1} + \Delta_{S2} \qquad d_{\mathrm{I}a} \to d_a - \Delta_{S2} + \Delta_{M\mathrm{I}1} \tag{5.57}$$

$$D_{M\mathrm{I}} \to D_M - \Delta_{M\mathrm{I}1} + \Delta_{M\mathrm{I}2} \qquad d_{\mathrm{I}b} \to d_b - \Delta_{M\mathrm{I}2} + \Delta_{A1} \tag{5.58}$$

$$D_{M\mathrm{II}} \to D_M - \Delta_{M\mathrm{II}1} + \Delta_{M\mathrm{II}2} \qquad d_{\mathrm{II}a} \to d_b - \Delta_{S2} + \Delta_{M\mathrm{II}1} \tag{5.59}$$

$$D_A \to D_S - \Delta_{A1} + \Delta_{A2} \qquad d_{\mathrm{II}b} \to d_a - \Delta_{M\mathrm{II}2} + \Delta_{A1} \tag{5.60}$$

The average wave function is calculated by integrating over all 8 fluctuations. Using Gaussian distributions with the standard deviation σ one obtains the analytic result (after a long calculation with Mathematica):

$$\begin{aligned}\langle|\psi_O|^2\rangle = \frac{1}{4(1+y^2)^3}\Big[&\big(1-\mathrm{e}^{-v^2\eta^2\sigma^2}\cos(D_M v\eta)\big)\big(1-\mathrm{e}^{-v^2\eta^2\sigma^2}\cos(D_S v\eta)\big)\big(1+2y^2+\mathrm{e}^{-v^2\eta^2\sigma^2}\cos(D_S v\eta)\big)+\\ &+\mathrm{e}^{-(2v^2+y^2)\eta^2\sigma^2}\big(\cosh(v\eta^2\sigma^2)-\cos(D_M v\eta)\big)\times\\ &\times\Big\{\mathrm{e}^{-v^2\eta^2\sigma^2}\big(\cosh^2(vy\eta^2\sigma^2)-\cos^2(D_S v\eta)\big)+2y^2\sinh(v^2\eta^2\sigma^2)+\\ &+\Big(\mathrm{e}^{-v^2\eta^2\sigma^2}\cosh(vy\eta^2\sigma^2)-\cos(D_S v\eta)\Big)\big(2y^2\cosh(vy\eta^2\sigma^2)-2vy\sinh(vy\eta^2\sigma^2)\big)\Big\}\Big]\end{aligned} \tag{5.61}$$

with $v=\sqrt{1+y^2}$, $\eta=\frac{2\pi}{\Delta_0}$. The result is shown in figure 5.10 for various values of σ.

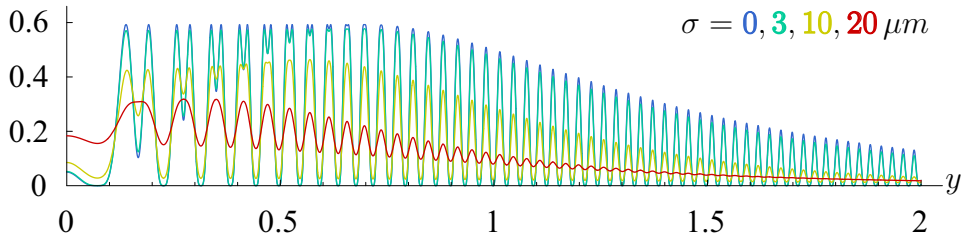

Figure 5.10: Pendellösung oscillations for different surfaces wavyness. Parameters: Si220, θ_B=30°, $\Delta_0 = 68\mu$m, $D_S = D_M = D_A = 3$mm.

Chapter 6

Spherical Theory of the Interferometer

The plane wave theory described in chapter 5 is sufficient to calculate the phase shift of a sample which does not diffract the beam. If the sample creates diffraction patterns then the spherical wave theory provides more accurate results. It calculates the spacial distribution of the neutron wave function within the interferometer.

By expanding spherical waves in plane waves the results of the plane wave theory can be used. As both the interferometer and the sample are not sensitive to the vertical component, we will calculate the spherical waves only in two dimensions, which means that we are actually using cylindrical waves.

6.1 Incoming Beam

The incoming beam is considered a monochromatic beam with a given angle distribution g_θ. In k space the wave function can be written as $g(\vec{k}) = \delta(k-k_0)\ g_\theta(\theta)$, see figure 6.1. The fourier transform gives the wave function in real space

$$\psi(\vec{r}) = \frac{1}{2\pi}\int d^2k\, \mathrm{e}^{\mathrm{i}\vec{k}\vec{r}} g(\vec{k}) = \frac{1}{2\pi}\int_{-\pi}^{\pi} d\theta \int_0^\infty k\ dk\, \mathrm{e}^{\mathrm{i}\vec{k}\vec{r}}\delta(k-k_0)\ g_\theta(\theta) = \frac{k_0}{2\pi}\int_{-\pi}^{\pi} d\theta\, \mathrm{e}^{\mathrm{i}\vec{k}_0\vec{r}} g_\theta(\theta) \qquad (6.1)$$

A simple coordinate transformation shifts the beam origin to an arbitrary point $\vec{r}_0$.

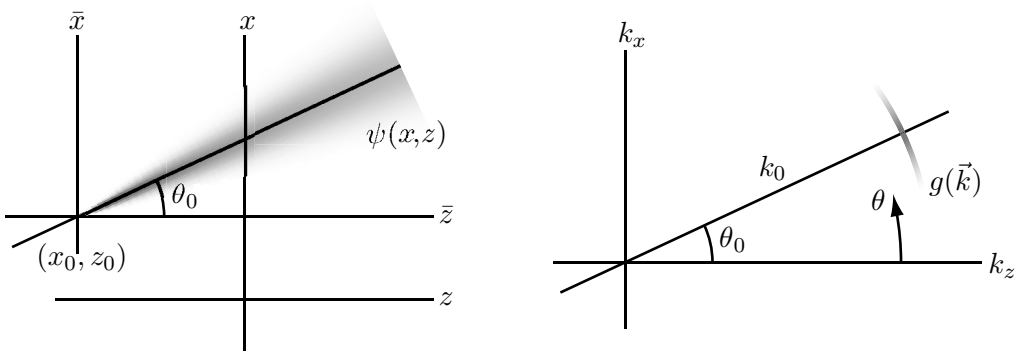

Figure 6.1: A two dimensional monochromatic beam with a given divergence

We use a Gaussian angle distribution $g_\theta = \exp\left(-(\theta-\theta_0)^2/(2\sigma_\theta)^2\right)/\sqrt{2\pi\sigma_\theta^2}$ with $\sigma_\theta \ll 1$. For calculating the beam width at a given distance r we can approximate the intensity distribution by a Gaussian distribution which depends on the distance r and the transverse coordinate t.

$$|\psi(r,t)|^2 = \frac{1}{\sqrt{1+k^2r^2\sigma_\theta^4}}\exp\left(-\frac{t^2}{2\sigma_t^2}\right) \qquad \sigma_t = \sqrt{\frac{1}{2}\left(\frac{1}{k^2\sigma_\theta^2}+\sigma_\theta^2 r^2\right)} \tag{6.2}$$

Thus the beam width σ_t can be controlled by chosing an appropriate source distance r.

For the interferometer calculations we will express the beam direction θ in terms of y according to (5.7).

$$\psi_{in}(\vec{r}) = \int dy\, g(y) \exp\left(\mathrm{i}\vec{k}_O(\vec{r}-\vec{r}_0)\right) \tag{6.3}$$

$$g = g(y) = \frac{1}{\sqrt{2\pi}\,\sigma_y}\exp\left(-\frac{y^2}{2\sigma_y^2}\right) \tag{6.4}$$

6.2 Empty Interferometer

Now we want to calculate the wave functions inside the interferometer for an incident beam given by (6.3). We take the plane wave formulas (5.19) to (5.29), put $\int dy g(y)$ in front of it and replace $\vec{r}$ by $(\vec{r}-\vec{r}_0)$. The result is shown in figure 6.2. The beam profiles are plotted in figure 6.3. The transverse coordinate is given in terms of Γ. The entry point of the beam defines $\Gamma = 0$. After the first interferometer blade the beam is spread to a width of $\pm\Gamma = \pm D\tan\theta_B$.

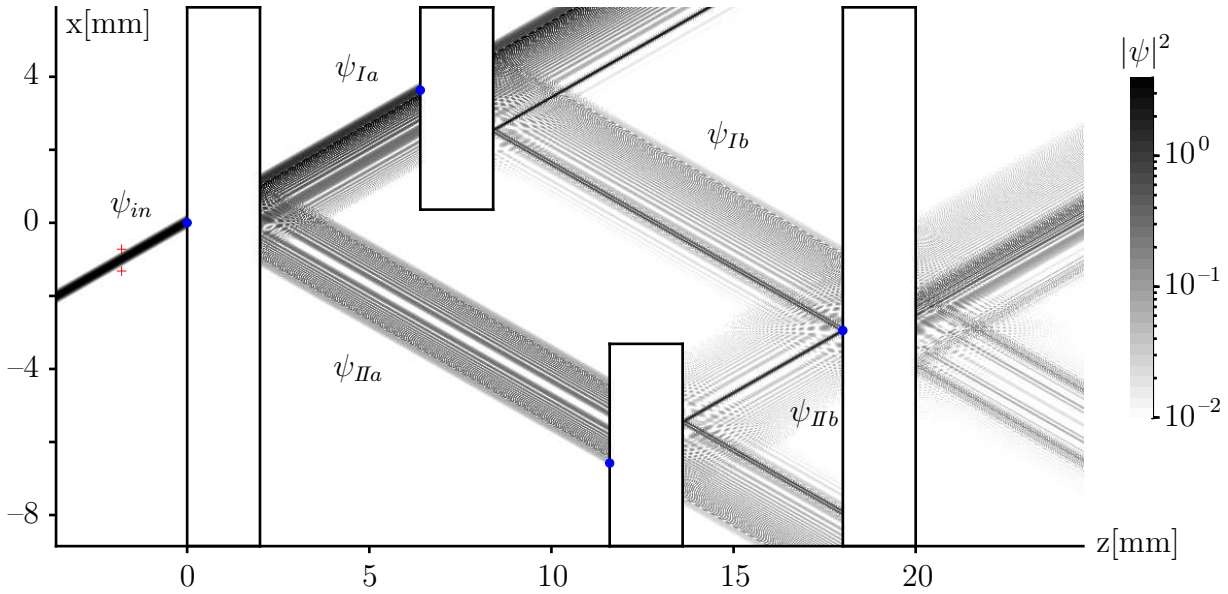

Figure 6.2: Intensity distribution in an empty interferometer. The physical dimensions are reduced in order to show both the whole interferometer and a detailed view of the transverse beam pattern. The distance from the source $\vec{r}_0$ to the entry point $\vec{0}$ is 10m. A beam divergence of 0.0004° is used. (The real beam divergence is much larger but for a monochromatic calculation it is useless to assume a divergence larger than the Laue reflection width.)

After the second and the third blade we have a width of $\pm 2\Gamma$ and $\pm 3\Gamma$ respectively. The shape of these profiles is well known from perfect crystal neutron optics [BG77], [Wer80], [RW00].

The profiles of the O and the H beam are shown in figure 6.4 for different phase shifter values. The integration over the transverse direction of the O and the H beam gives the intensities measured in an experiment. Plotting the intensity versus the phase shifter value gives an interferogram as shown in figure 6.5. The interferogram can be evaluated in the same way as experimental data. A sine fit provides the phase and the visibility.

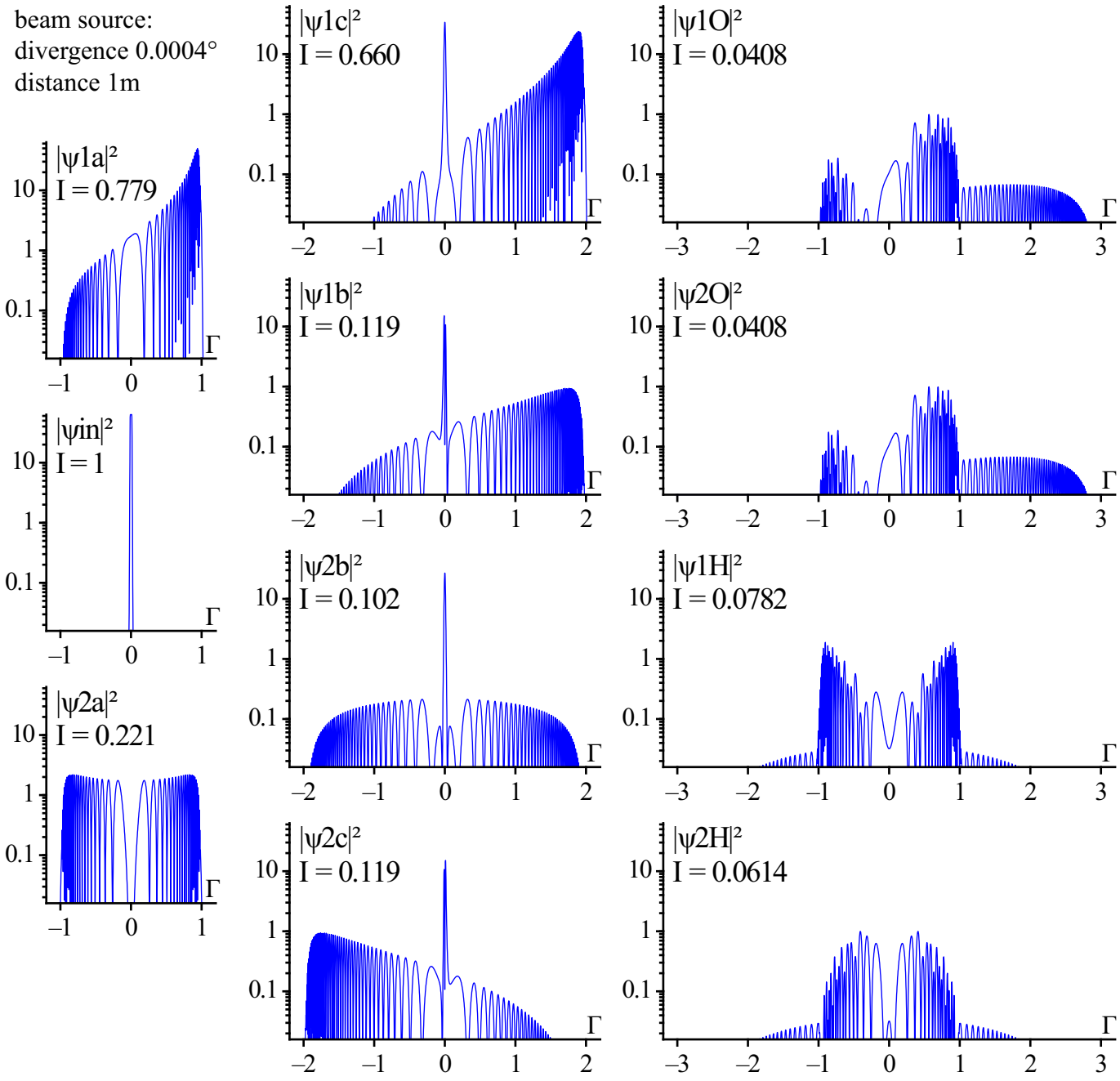

Figure 6.3: Intensity profiles for the different beam path sections. The total intensity I is calculated by integration over Γ.

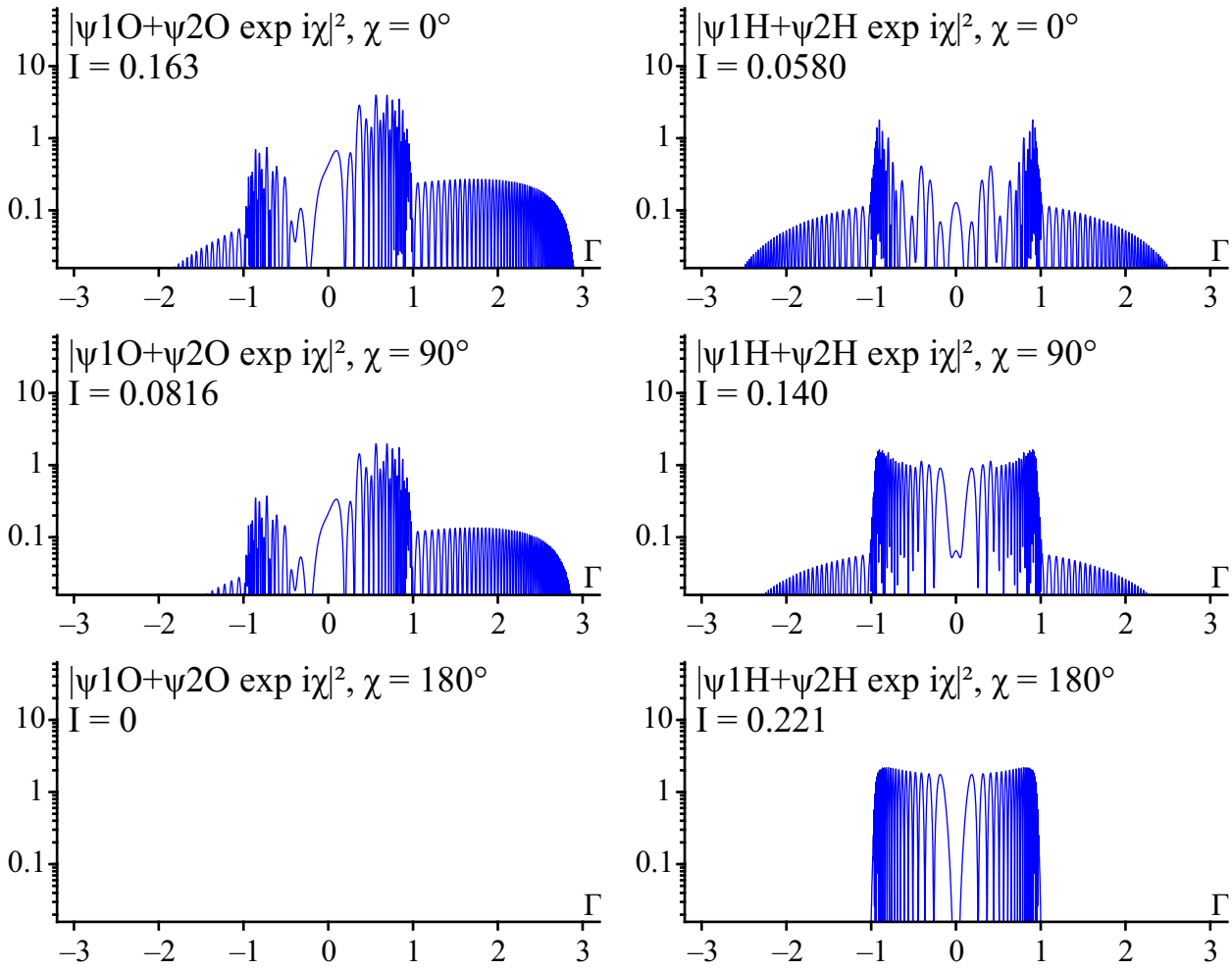

Figure 6.4: Intensity profile of the O and H beam for different phase shifter settings.

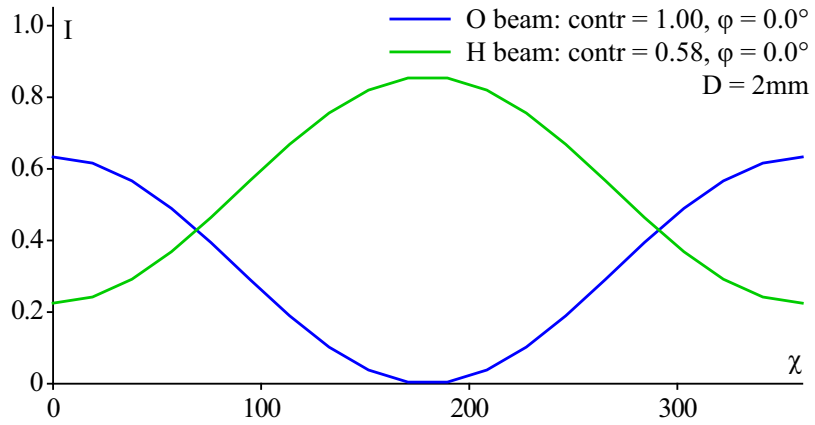

Figure 6.5: Interferogram of the empty interferometer, calculated by integration of the intensity profiles of figure 6.4. The contrast and phase shift is obtained by fitting a sine curve to the data, similar to the evaluation of experimental data.

For the numerical integration the integrals have to be approximated by a discrete sum

$$\int_{y_1}^{y_2} dy\, f(y) \;\to\; \sum_{i=1}^{N} \Delta y_i\; f(y_i) \;\xrightarrow{\Delta y_i \text{ const}}\; \frac{y_2-y_1}{N} \sum_{i=1}^{N} y_i\; f(y_i) \tag{6.5}$$

This discretization produces artificial copies of the beam with the transverse periodicity of $w \approx \lambda/\Delta\theta$ where $\Delta\theta$ denotes the step size Δy in radiant units according to (5.7). We have to chose the step size small enough so that the artefacts lie outside the region of interest

$$\Delta\theta \lesssim \frac{\lambda}{w} \tag{6.6}$$

For a neutron wavelength of $\lambda = 2\text{Å}$ and a beam width w of a few mm we get $\Delta\theta \approx 10^{-8}$ or $\Delta y \approx 0.01$. This should also be checked against the width of the Pendellösung fringes as shown in figure 5.5.

6.3 Interferometer with a Diffracting Sample

Let a diffracting sample like a slit be inserted into the interferometer at a position denoted by $\vec{r}_P$. The slit has the property to spread an incoming plane wave ψ of direction y into different directions $\widetilde{y}$ according to the function $S(y,\widetilde{y})$:

$$\widetilde{\psi}(\vec{r}) = \psi(\vec{r}_P) \int d\widetilde{y}\, S(y,\widetilde{y}) \exp\bigl(\mathrm{i}\vec{\widetilde{k}}(\vec{r}-\vec{r}_P)\bigr) \tag{6.7}$$

with $\vec{\widetilde{k}}$ representing the wave vector in the diffracted direction $\widetilde{y}$. For our channel experiment S is taken from tabulated data calculated by (2.50).

Now we can calculate the wave functions $\widetilde{\psi}_{\dots}$ in the interferometer downstream of the sample. All expressions depending on $\widetilde{y}$ instead of y are marked with $\widetilde{\ }$: $\widetilde{\rho} := \rho(\widetilde{y})$, $\widetilde{\tau} := \tau(\widetilde{y})$, etc. $\widetilde{d}_j$ represents the distance from $\vec{r}_P$ to the next interferometer blade.

- sample position $\vec{r}_P$ in region Ia:

$$\widetilde{\psi}_{\mathrm{I}a} = \int dy\, g\, \tau_S \exp\bigl(\mathrm{i}\vec{k}_O\vec{r}_P - \mathrm{i}\tfrac{y\pi}{\Delta_0}D_S\bigr) \int d\widetilde{y} \quad S \quad \exp\bigl(\mathrm{i}\vec{\widetilde{k}}_O(\vec{r}-\vec{r}_P)\bigr) \tag{6.8}$$

$$\widetilde{\psi}_{\mathrm{I}b} = \int dy\, g\, \tau_S \exp\bigl(\mathrm{i}\vec{k}_O\vec{r}_P - \mathrm{i}\tfrac{y\pi}{\Delta_0}D_S\bigr) \int d\widetilde{y}\; S\; \widetilde{\rho}_M \exp\bigl(\mathrm{i}\vec{\widetilde{k}}_H(\vec{r}-\vec{r}_P) + \mathrm{i}\tfrac{\widetilde{y}\pi}{\Delta_0}(D_M+2\widetilde{d}_{\mathrm{I}a})\bigr) \tag{6.9}$$

$$\widetilde{\psi}_{\mathrm{I}c} = \int dy\, g\, \tau_S \exp\bigl(\mathrm{i}\vec{k}_O\vec{r}_P - \mathrm{i}\tfrac{y\pi}{\Delta_0}D_S\bigr) \int d\widetilde{y}\; S\; \widetilde{\tau}_M \exp\bigl(\mathrm{i}\vec{\widetilde{k}}_O(\vec{r}-\vec{r}_P) - \mathrm{i}\tfrac{\widetilde{y}\pi}{\Delta_0}D_M\bigr) \tag{6.10}$$

$$\widetilde{\psi}_{\mathrm{I}O} = \int dy\, g\, \tau_S \exp\bigl(\mathrm{i}\vec{k}_O\vec{r}_P - \mathrm{i}\tfrac{y\pi}{\Delta_0}D_S\bigr) \int d\widetilde{y}\, S\, \widetilde{\rho}_M\, \widetilde{\rho}_A \exp\bigl(\mathrm{i}\vec{\widetilde{k}}_O(\vec{r}-\vec{r}_P) - \mathrm{i}\tfrac{\widetilde{y}\pi}{\Delta_0}(D_M+D_A+2d_{\mathrm{I}b})\bigr) \tag{6.11}$$

$$\widetilde{\psi}_{\mathrm{I}H} = \int dy\, g\, \tau_S \exp\bigl(\mathrm{i}\vec{k}_O\vec{r}_P - \mathrm{i}\tfrac{y\pi}{\Delta_0}D_S\bigr) \int d\widetilde{y}\, S\, \widetilde{\rho}_M\, \widetilde{\tau}_A \exp\bigl(\mathrm{i}\vec{\widetilde{k}}_H(\vec{r}-\vec{r}_P) + \mathrm{i}\tfrac{\widetilde{y}\pi}{\Delta_0}(D_M+D_A+2\widetilde{d}_{\mathrm{I}a})\bigr) \tag{6.12}$$

- sample position $\vec{r}_P$ in region IIa:

$$\widetilde{\psi}_{\mathrm{II}a} = \int dy\, g\, \rho_S \exp\bigl(\mathrm{i}\vec{k}_H\vec{r}_P + \mathrm{i}\tfrac{y\pi}{\Delta_0}(D_S+d_0)\bigr) \int d\widetilde{y} \quad S \quad \exp\bigl(\mathrm{i}\vec{\widetilde{k}}_H(\vec{r}-\vec{r}_P)\bigr) \tag{6.13}$$

$$\widetilde{\psi}_{\mathrm{II}b} = \int dy\, g\, \rho_S \exp\bigl(\mathrm{i}\vec{k}_H\vec{r}_P + \mathrm{i}\tfrac{y\pi}{\Delta_0}(D_S+d_0)\bigr) \int d\widetilde{y}\; S\; \widetilde{\rho}_M \exp\bigl(\mathrm{i}\vec{\widetilde{k}}_O(\vec{r}-\vec{r}_P) - \mathrm{i}\tfrac{\widetilde{y}\pi}{\Delta_0}(D_M+2\widetilde{d}_{\mathrm{II}a})\bigr) \tag{6.14}$$

$$\widetilde{\psi}_{\mathrm{II}c} = \int dy\, g\, \rho_S \exp\bigl(\mathrm{i}\vec{k}_H\vec{r}_P + \mathrm{i}\tfrac{y\pi}{\Delta_0}(D_S+d_0)\bigr) \int d\widetilde{y}\; S\; \widetilde{\tau}_M \exp\bigl(\mathrm{i}\vec{\widetilde{k}}_H(\vec{r}-\vec{r}_P) + \mathrm{i}\tfrac{\widetilde{y}\pi}{\Delta_0}D_M\bigr) \tag{6.15}$$

$$\widetilde{\psi}_{\mathrm{II}O} = \int dy\, g\, \rho_S \exp\bigl(\mathrm{i}\vec{k}_H\vec{r}_P + \mathrm{i}\tfrac{y\pi}{\Delta_0}(D_S+d_0)\bigr) \int d\widetilde{y}\, S\, \widetilde{\rho}_M\, \widetilde{\rho}_A \exp\bigl(\mathrm{i}\vec{\widetilde{k}}_O(\vec{r}-\vec{r}_P) - \mathrm{i}\tfrac{\widetilde{y}\pi}{\Delta_0}(D_M+D_A+2\widetilde{d}_{\mathrm{II}a})\bigr) \tag{6.16}$$

$$\widetilde{\psi}_{\mathrm{II}H} = \int dy\, g\, \rho_S \exp\bigl(\mathrm{i}\vec{k}_H\vec{r}_P + \mathrm{i}\tfrac{y\pi}{\Delta_0}(D_S+d_0)\bigr) \int d\widetilde{y}\, S\, \widetilde{\rho}_M\, \widetilde{\tau}_A \exp\bigl(\mathrm{i}\vec{\widetilde{k}}_H(\vec{r}-\vec{r}_P) + \mathrm{i}\tfrac{\widetilde{y}\pi}{\Delta_0}(D_M+D_A+2d_{\mathrm{II}b})\bigr) \tag{6.17}$$

• sample position $\vec{r}_P$ in region Ib:

$$\widetilde{\psi}_{\mathrm{Ib}} = \int dy\, g\, \tau_S\, \rho_M \exp\!\big(\mathrm{i}\vec{k}_H\vec{r}_P + \mathrm{i}\tfrac{y\pi}{\Delta_0}(D_S+D_M+2d_0+2d_{\mathrm{Ia}})\big) \int d\widetilde{y}\quad S\quad \exp\!\big(\mathrm{i}\vec{\tilde{k}}_H(\vec{r}-\vec{r}_P)\big) \tag{6.18}$$

$$\widetilde{\psi}_{\mathrm{I}O} = \int dy\, g\, \tau_S\, \rho_M \exp\!\big(\mathrm{i}\vec{k}_H\vec{r}_P + \mathrm{i}\tfrac{y\pi}{\Delta_0}(D_S+D_M+2d_0+2d_{\mathrm{Ia}})\big) \int d\widetilde{y}\, S\, \widetilde{\tilde{\rho}}_A \exp\!\big(\mathrm{i}\vec{\tilde{k}}_O(\vec{r}-\vec{r}_P) - \mathrm{i}\tfrac{\widetilde{y}\pi}{\Delta_0}(D_A+2\widetilde{d}_{\mathrm{Ib}})\big) \tag{6.19}$$

$$\widetilde{\psi}_{\mathrm{I}H} = \int dy\, g\, \tau_S\, \rho_M \exp\!\big(\mathrm{i}\vec{k}_H\vec{r}_P + \mathrm{i}\tfrac{y\pi}{\Delta_0}(D_S+D_M+2d_0+2d_{\mathrm{Ia}})\big) \int d\widetilde{y}\, S\, \widetilde{\tilde{\tau}}_A \exp\!\big(\mathrm{i}\vec{\tilde{k}}_H(\vec{r}-\vec{r}_P) + \mathrm{i}\tfrac{\widetilde{y}\pi}{\Delta_0}D_A\big) \tag{6.20}$$

• sample position $\vec{r}_P$ in region IIb:

$$\widetilde{\psi}_{\mathrm{II}b} = \int dy\, g\, \rho_S\, \bar{\rho}_M\ \exp\!\big(\mathrm{i}\vec{k}_O\vec{r}_P - \mathrm{i}\tfrac{y\pi}{\Delta_0}(D_S+D_M+2d_{\mathrm{II}a})\big) \int d\widetilde{y}\quad S\quad \exp\!\big(\mathrm{i}\vec{\tilde{k}}_O(\vec{r}-\vec{r}_P)\big) \tag{6.21}$$

$$\widetilde{\psi}_{\mathrm{II}O} = \int dy\, g\, \rho_S\, \bar{\rho}_M\ \exp\!\big(\mathrm{i}\vec{k}_O\vec{r}_P - \mathrm{i}\tfrac{y\pi}{\Delta_0}(D_S+D_M+2d_{\mathrm{II}a})\big) \int d\widetilde{y}\, S\, \widetilde{\tau}_A \exp\!\big(\mathrm{i}\vec{\tilde{k}}_O(\vec{r}-\vec{r}_P) - \mathrm{i}\tfrac{\widetilde{y}\pi}{\Delta_0}D_A\big) \tag{6.22}$$

$$\widetilde{\psi}_{\mathrm{II}H} = \int dy\, g\, \rho_S\, \bar{\rho}_M\ \exp\!\big(\mathrm{i}\vec{k}_O\vec{r}_P - \mathrm{i}\tfrac{y\pi}{\Delta_0}(D_S+D_M+2d_{\mathrm{II}a})\big) \int d\widetilde{y}\, S\, \widetilde{\rho}_A \exp\!\big(\mathrm{i}\vec{\tilde{k}}_H(\vec{r}-\vec{r}_P) + \mathrm{i}\tfrac{\widetilde{y}\pi}{\Delta_0}(D_A+2\widetilde{d}_{\mathrm{II}b})\big) \tag{6.23}$$

If the sample consists of many independent slits separated by opaque walls, then S can be calculated for a single channel and summed up afterwards for all channel positions p. S can depend on p if the channels are not exactly parallel aligned or have different width. Figure 6.6 shows the numerical calculation of the wave function directly behind the channels (6.13).

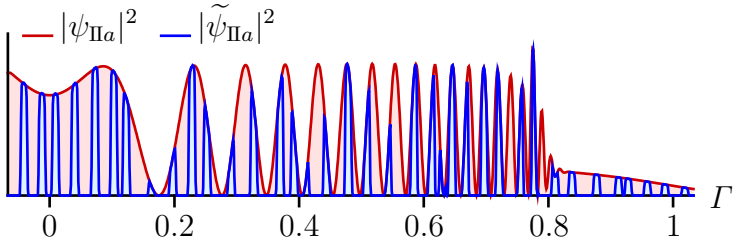

Figure 6.6: Red: The wave function in position IIa.
Blue: The wave function at the same position after inserting the channel stack. The wave function is calculated at the channel ends according to formula (6.13). The intensity seems to be zero at positions of the channel walls. This is a consequence of averaging over different channel lengths (2.32). (Justified?)

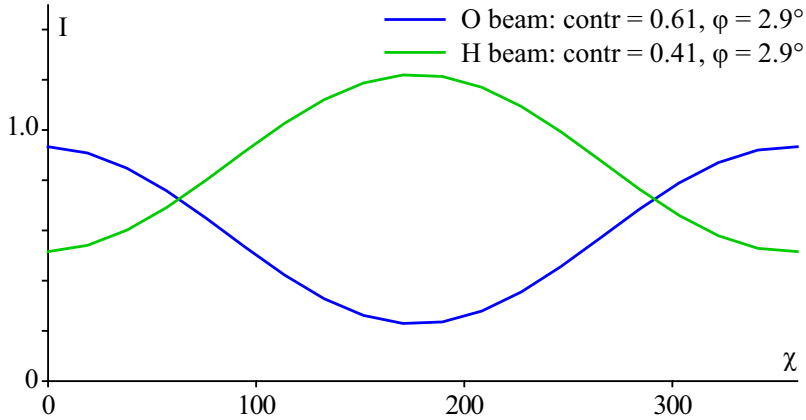

Figure 6.7: Interferogram with the channel stack inserted in position IIa.

The numerical calculation of the whole interferogram (figure 6.7) is very time consuming because of the two nested integrals with a few thousand integration steps each. Behind the third interferometer blade the beam is spread to a width of 7 mm which leads with (6.6) to $\Delta y < 0.01$. For an integration range of $-20 < y < 20$ we have 4000 steps.

Table 6.1 shows a few results of the phase shift for different parameters of sample position, blade thickness D and channel length L.

		$D = 3$mm	$D = 2.95$mm	$D = 2.9$mm	$D = 2.85$mm
$L = 2$cm	Pos. Ia	5.7°	8.5°	6.6°	2.8°
	Pos. IIa	-2.7°	2.9°	-3.2°	-2.3°
	Pos. Ib	2.8°	3.3°	3.1°	2.7°
	Pos. IIb	-2.8°	1.7°	-3.5°	-3.0°
$L = 0.01$cm	Pos. Ia		-5.6°	4.0°	-0.5°
	Pos. IIa		-0.1°	0.2°	-0.4°
	Pos. Ib		-0.2°	0.1°	-0.3°
	Pos. IIb		1.1°	0.5°	0.1°

Table 6.1: Numerical results of the phase shift by the channel stack, taking into account the diffraction by the channels.

The results are quite fluctuating, and a complete interpretation cannot be given until more sets of parameters are evaluated. (Which was not possible so far for lack of computer power. One set of parameters took 24 hours for 30 processors.) Nevertheless we can already recognize some interesting features, which we have also observed experimentally:

- The phase shift depends on the sample position.
- The phase shift in beam I and II is not symmetric in respect to zero.
- The phase shift depends on the blade thickness D in a non-linear maybe oscillating way. The same dependency can be expected on the wave length λ, as D and λ enter in a similar way, see (5.4). This could explain the sensitivity of the measurements regarding the beam angle, because the beam angle is correlated to the wave length.
- The phase shift does not vanish for $L \approx 0$, which means that we have to look for an additional effect besides the confinement induced phase shift.

What is the physics behind this? I would suppose an interaction between the diffraction by the sample and the dynamical diffraction in the crystal blades of the neutron interferometer. Let's recall what we have calculated here. The calculations take into account the components of a neutron beam which are coherent to each other but have different directions y. The distribution of directions is very narrow because it is restricted to the Laue reflection width (formula (5.3), figure 5.5), but within this distribution the components are coherent. This bunch of components is split up into two beam paths and interferes at the end of the interferometer.

If no diffraction occurs then each component of beam path I has a corresponding component in beam path II with the same y. These two components can interfere according to the plane wave formulas (5.26ff). Due to the focused condition of the interferometer, the resulting phase shift does not depend on y. All components contribute with the same phase shift which depends only on the phase shifter and the sample.

If we have a *diffracting* sample then the components of different directions are mixed up. A component y_0 for example of the reference beam interferes also with all y components which had initially another value but have been (partially) diffracted into the direction y_0. The interfering terms are no longer independent from y. We can hardly make any presumptions of the result of this complicated interference. We can just integrate over the diffraction angle $\widetilde{y}$ and the incident angle y and look what comes out, see table 6.1.

Further calculations and experiments would be necessary to investigate this effect.

Conclusion and Outlook

The phase shift caused by lateral confinement has been calculated in detail for neutrons in a narrow channel. The estimations by Lévy-Leblond and Greenberger have been extended to a realistic experimental situation, taking into account the excitation amplitudes of the transverse modes.

The phase shift has been measured in a series of neutron interferometry experiments. Surprisingly, the results show some interesting features which cannot be explained by the confinement effect. The phase shifts are larger than expected and they are different in the different branches of the interferometer. In addition the phase shifts depend on the beam angle (which is correlated with the wave length) in a way that cannot be explained by the channel calculations.

In order to explain these effects, the calculations have been extended from the channels to the whole interferometer system. There is some evidence, that the effects are caused by the combination of channel diffraction and the special properties of a neutron interferometer. In the case of neutrons, the beam splitters of the interferometer are not just half transparent mirrors like in optical interferometers. The beam splitters consist of perfect crystals which transmit and reflect the wave function in a very special way, described by the dynamical theory of diffraction. The reflection amplitude of a crystal shows oscillations with the beam angle on a sub-arcsecond scale. If the channel stack is put into the interferometer, then this fine structure is disturbed by the channel diffraction. One has to regard the channels and the interferometer as a combined system and cannot tell any more which one is the probe of the other.

For obtaining the neutron wave function in the combined system, the interferometer theory based on the dynamical theory of diffraction has been extended to diffracting samples. The analytical calculations end up in two nested integrals which have to be solved numerically. Due to lack of computer power these numerical calculations have been done only for a few sets of parameters. The qualitative results are promising, as they explain additional phase contributions as well as differences between the interferometer branches. However, to obtain reliable quantitative results, more calculations would be necessary. The influence of different sets of parameters should be systematically determined, including the Bragg angle, wave length, channel angle and geometrical parameters of the channel stack.

On the experimental side one could proceed with an interferometry measurement of a grating made of absorbing wires. This would be equivalent to a channel stack with zero length. There would be virtually no confinement phase because of $L \approx 0$ and no material phase because of the absorption in the wires.

Bibliography

[ACGK99] B. E. Allman, A. Cimmino, S. L. Griffin, and A. G. Klein, *Quantum Phase Shift Caused by Spatial Confinement*, Foundations of Physics **29-3** (1999), 325.

[ACK00] B. E. Allman, A. Cimmino, and A. G. Klein, *Reply to "Comment on Quantum Phase Shift Caused by Spatial Confinement" by M. Peshkin*, Foundations of Physics Letters **19** (2000), no. 1, 101.

[AEC84] R. F. Alvarez-Estrada and M. L. Calvos, *Neutron fibers: a possible application of neutron optics*, Journal of Physics D **17** (1984), 175.

[ALMW99] B. E. Allman, W.-T. Lee, O. I. Motrunich, and S. A. Werner, *Scalar Aharonov-Bohm effect with longitudinally polarized neutrons*, Physical Review A **60** (1999), no. 6, 4272.

[BBG76] W. Bauspiess, U. Bonse, and W. Graeff, *Spherical-Wave Theory of the Zero-Absorption LLL X-Ray or Neutron Interferometer*, Journal of Applied Crystallography **9** (1976), 68.

[BFG+02] R. Brühl, P. Fouquet, R. E. Grisenti, J. P. Toennies, G. C. Hegerfeldt, T. Köhler, M. Stroll, and C. Walter, *The van der Waals potential between metastable atoms and solid surfaces: Novel difraction experiments vs. theory*, Europhysics Letters **59** (2002), 357.

[BG77] U. Bonse and W. Graeff, *X-Ray and Neutron Interferometry*, ch. 4, Springer Verlag, 1977.

[BKM04] J. F. Babb, G. L. Klimchitskaya, and V. M. Mostepanenko, *Casimir-Polder interaction between an atom and a cavity wall under the influence of real conditions*, Physical Review A **70** (2004), 042901.

[BMS01] Michael Berry, Irene Marzoli, and Wolfgang Schleich, *Quantum Carpets, Carpets of Light*, Physics World (2001).

[Bra75] Siegmund Brandt, *Datenanalyse*, second ed., Bibliographisches Institut, 1975.

[BS99] Ludwig Bergmann and Clemens Schaefer, *Optics of Waves and Particles*, ch. 11, Walter de Gruyter, New York, 1999.

[BWG+93] G. Badurek, H. Weinfurter, R. Gähler, A. Kollmar, S. Wehinger, and A. Zeilinger, *Nondispersive Phase of the Aharonov-Bohm Effect*, Physical Review Letters **71** (1993), no. 3, 307.

[Dan02] R. Dandoloff, *Geometric Phase and Quantum Potential*, http://arxiv.org/ **quant-ph** (2002), 0212115.

[Gre88] Daniel M. Greenberger, *A New Non-Local Effect in Quantum Mechanics*, Physica B **151** (1988), 374.

[HJ01] Martin Hainbuchner and Erwin Jericha, *Neutron scattering lengths*, Tech. report, Atominstitut der Österreichischen Universitäten, http://www.ati.ac.at/ neutropt/scattering/table.html, 2001.

[HK00] Gerhard C. Hegerfeldt and Thorsten Köhler, *Deviations from classical optics in matter diffraction and determination of the size of weakly bound molecules*, Physical Review A **61** (2000), 023606.

[HR93] Serge Haroche and Jean-Michel Raimond, *Cavity Quantum Electrodynamics*, Scientific American **268** (1993), no. 4, 26.

[Jac] J. D. Jackson, *Classical Electrodynamics*, third ed., ch. 8: Waveguides, Resonant Cavities and Optical Fibers.

[Kas92] R. E. Kastner, *Geometrical quantum phase effect and Bohm's quantum potential*, American Journal of Physics **61** (1992), 852.

[KBB+00] G. Kroupa, G. Bruckner, O. Bolik, M. Zawisky, M. Hainbuchner, G. Badurek, R.J. Buchelt, A. Schricker, and H. Rauch, *Basic features of the upgraded S18 neutron interferometer set-up at ILL*, Nuclear Instruments & Methods in Physics Research A **440** (2000), 604.

[KHB+05] W. Ketter, W. Heil, G. Badurek, M. Baron, R. Loidl, and H. Rauch, *Measurement of the Coherent Neutron Scattering Length of ^{3}He*, Journal of Research of the National Institute of Standards and Technology **110** (2005), 241.

[LL87] Jean-Marc Lévy-Leblond, *A Geometrical Quantum Phase Effect*, Physics Letters A **125** (1987), 441.

[NAD+05] J. S. Nico, M. Arif, M. S. Dewey, T. R. Gentile, D. M. Gilliam, P. R. Huffman, D. L. Jacobson, and A. K. Thompson, *The Fundamental Neutron Physics Facilities at NIST*, Journal of Research of the National Institute of Standards and Technology **110** (2005), 137.

[NBG+03] V. V. Nesvizhevsky, H. G. Börner, A. M. Gagarski, A. K. Petoukhov, G. A. Petrov, H. Abele, S. Baeßler, G. Divkovic, F. J. Rueß, Th. Stöferle, A. Westphal, A. V. Strelkov, K. V. Protasov, and A. Yu. Voronin, *Measurement of quantum states of neutrons in the Earth's gravitational field*, Physical Review D **67** (2003), 102002.

[PC05] John D. Perreault and Alexander D. Cronin, *Observation of Atom Wave Phase Shifts induced by Van Der Waals Atom-Surface Interactions*, Physical Review Letters **95** (2005), 133201.

[Pér96] José-Philippe Pérez, *Optik*, Spektrum Akademischer Verlag, 1996.

[Pes00] Murray Peshkin, *Comment on "Quantum Phase Shift Caused by Spatial Confinement" by B. E. Allman et al.*, Foundations of Physics Letters **19** (2000), no. 1, 97.

[Pok97] Yu. N. Pokotilovski, *Quantum Phase Shift of Spatially Confined de Broglie Waves in Gravitational Field*, JINR Publications Dubna (1997).

[PVTF02] W. H. Press, W. T. Vetterling, S. A. Teukolsky, and B. P. Flannery, *Numerical Recipes in C++*, Cambridge University Press, 2002.

[RLBL02] Helmut Rauch, Hartmut Lemmel, Matthias Baron, and Rudolf Loidl, *Measurement of a Confinement Induced Neutron Phase*, nature **417** (2002), 630.

[Rob04] R. W. Robinett, *Quantum wave packet revivals*, http://arxiv.org/ **quant-ph** (2004), 0401031.

[Roh02] B. Rohwedder, *Interference effects in capillary neutron guides*, Physical Review A **65** (2002), 043619.

[RP74] Helmut Rauch and Dietmar Petrascheck, *Grundlagen für ein Laue-Neutroneninterferometer*, Atominstitut der Österreichischen Universitäten, 1974.

[RW00] Helmut Rauch and Samuel A. Werner, *Neutron Interferometry*, Clarendon Press, Oxford, 2000.

[VAB+06] Y. Yu. Voronin, H. Abele, S. Baeßler, V. V. Nesvizhevsky, A. K. Petukhov, K. V. Protasov, and A. Westphal, *Quantum motion of a neutron in a wave-guide in the gravitational field*, Physical Review D **73** (2006), 044029.

[Wer80] Samuel A. Werner, *Gravitational and magnetic field effects on the dynamical diffraction of neutrons*, Physical Review B **21** (1980), 1774.

Curriculum Vitae

Name	Hartmut Lemmel
geboren am	21.6.1973 in Wien
Staatsangehörigkeit	Deutschland

Schulausbildung

1984-1992	Allgemeinbildende Höhere Schule, neusprachlicher Zweig
1992	Matura mit Auszeichnung am Bundesgymnasium Wien XVI, Maroltingergasse

Hochschulausbildung

1992	Beginn des Studiums "Technische Physik" an der TU Wien
1998	Entwicklung einer PC-Steckkarte zur Erfassung von zeitaufgelösten Gamma-Spektren.
2000	Abschluss des Studiums mit der Diplomarbeit "Phasenschub von Neutronen in engen Kanälen"
2001-2006	Doktoratsstudium am Atominstitut der Österreichischen Universitäten, TU Wien, im Rahmen des SFB-Projekts 15 (1513) "Control and Measurement of Coherent Quantum Systems". Mehrere mehrwöchige Aufenthalte am Institute Laue Langevin (ILL) in Grenoble in Frankreich, und am National Institute of Standards and Technology (NIST) in Gaithersburg, Maryland, USA.

Berufslaufbahn im Bereich Softwareentwicklung

ab 1994	Planung und Programmierung der Software *capella-scan*, einer OCR-Software für Musiknoten, für die Firma capella-software GmbH, http://www.capella.de Fertigstellung der Versionen 1.0 bis 6.0 in den Jahren '96, '97, '00, '02, '03, '04.
1998	Gründung der Lemmel GmbH in Wien. Seitdem Eigentümer und Geschäftsführer.

Sonstiges

ab 1995	Hornist im Orchester der TU-Wien